Quantification and evaluation of uncertainty in active buckling control of a beam-column subject to dynamic axial loads

vom Fachbereich Maschinenbau
der Technischen Universität Darmstadt

zur Erlangung des Grades
Doktor-Ingenieur (Dr.-Ing.)

Dissertation
von Maximilian Frederic Schäffner

Erstgutachter:	Prof. Dr.-Ing. Tobias Melz
Zweitgutachter:	Prof. Dr.-Ing. Uwe Klingauf

Darmstadt 2018

Schäffner, Maximilian Frederic: Quantification and evaluation of uncertainty in active buckling control of a beam-column subject to dynamic axial loads

Darmstadt, Technische Universität Darmstadt,
Jahr der Veröffentlichung der Dissertation auf TUprints: 2019
Tag der mündlichen Prüfung: 11.12.2018

Vorwort

Die vorliegende Arbeit entstand während meiner Tätigkeit als wissenschaftlicher Mitarbeiter am Fachgebiet Systemzuverlässigkeit, Adaptronik und Maschinenakustik SAM an der Technischen Universität Darmstadt und am Fraunhofer-Institut für Betriebsfestigkeit und Systemzuverlässigkeit LBF. Der Deutschen Forschungsgemeinschaft (DFG) danke ich für die finanzielle Förderung meiner Arbeit im Rahmen des Sonderforschungsbereichs (SFB) 805 „Beherrschung von Unsicherheit in lasttragenden Systemen des Maschinenbaus“.

Mein herzlicher Dank gilt meinem Doktorvater, Herrn Prof. Tobias Melz, für die Betreuung meiner Promotion. Herrn Prof. Uwe Klingauf, Leiter des Instituts für Flugsysteme und Regelungstechnik FSR, danke ich für die freundliche Übernahme des Korreferats und das entgegengebrachte Interesse an meinen Forschungsergebnissen. Ein großer Dank gilt Herrn Dr.-Ing. Roland Platz für die intensiven fachlichen Gespräche und seine wertvollen fachlichen Anregungen zu meiner Arbeit.

Zudem danke ich meinen Kollegen im SFB 805 und am Fraunhofer LBF für die auf fachlicher und persönlicher Ebene ausgezeichnete Zusammenarbeit. Insbesondere gilt dieser Dank meinen Freunden und Kollegen Christopher Gehb und Benedict Götz für die unzähligen fachlichen Diskussionen und die vielen gemeinsamen Erlebnisse, die mir noch lange in Erinnerung bleiben werden. Herrn Dr.-Ing. Georg Enß danke ich für die Vorarbeit an diesem Forschungsthema und die gute Einarbeitung in mein Teilprojekt. Ebenso danke ich Herrn Fabian Becker und Herrn Martin Sehr für den Instituts- und Universitätsübergreifenden fachlichen Austausch und die wertvollen Hinweise zu meiner Arbeit. Auch bei meinen Studenten und Hilfswissenschaftlern, die meine Forschung mit großer Motivation und Tatkraft unterstützt haben, möchte ich mich bedanken.

Meiner Familie und meinen Freunden danke ich für ihre Ermutigungen. Mein ganz besonderer Dank gilt Astrid für ihre Geduld sowie die liebevolle und beständige Unterstützung in allen Lebenslagen, ohne die diese Dissertation sonst nicht möglich gewesen wäre. Schließlich danke ich meinen wunderbaren Söhnen Jacob und Philipp für die Ablenkung und Perspektivwechsel während meiner Promotion.

Darmstadt, im Mai 2019 Max Schäffner

Abstract

Slender beam-columns in lightweight mechanical load-bearing structures are sensitive to failure by buckling when loaded by compressive axial loads. The maximum bearable axial load of a beam-column is considerably reduced by uncertainty in the material, geometry, loading or support properties, but may be increased by active buckling control. So far, studies on active buckling control have investigated academic beam-column systems with rectangular cross-sections, relatively high slenderness ratios and relatively small critical buckling loads as well as (quasi-)static axial loads. In this thesis, active buckling control of a practical beam-column system with circular cross-section, relatively low slenderness ratio and relatively high critical buckling load as well as dynamic axial loads is investigated. The goal is to increase the maximum bearable axial load and reduce uncertainty in the buckling behavior. For the latter, probabilistic uncertainty in the maximum bearable axial loads and lateral deflections of the passive and active beam-column systems is quantified and evaluated experimentally.

This thesis opens with a review of the background in static and dynamic passive buckling and the previous research on active buckling control. The concept for active buckling control uses innovative piezo-elastic supports with integrated piezoelectric stack actuators. A mathematical linear parameter-varying (LPV) model of the axially loaded beam-column system with electrical components accounts for the axial load-dependency of the lateral dynamic behavior. The model is calibrated with experimental data and then used to design an LPV controller, in particular a gain-scheduled $\mathscr{H}_\infty$ controller, which guarantees stability and robust performance for the entire operation range of axial loads. Passive buckling and active buckling control are investigated in an experimental test setup with slowly increasing quasi-static and step-shaped dynamic axial loads. Probabilistic uncertainty in the maximum bearable quasi-static axial loads and the lateral deflections for dynamic axial loads due to component variations in a representative sample of beam-column systems is investigated experimentally. The experimental results are quantified and evaluated by three-parameter WEIBULL distributions and compared for the passive and active beam-column systems with respect to their most likely values and variability.

The proposed gain-scheduled $\mathscr{H}_\infty$ buckling control stabilizes the beam-column system in arbitrary lateral direction. For quasi-static axial loads, the most likely maximum bearable axial load increases by 29% and the variability reduces by 70% when comparing the passive beam-column system. For dynamic axial loads, the most likely lateral deflections reduce by up to 87% and the variability reduces by up to 90%. Overall, the results of this thesis contribute to the application of active buckling control in practical truss structures.

Contents

Acknowledgments I

Abstract III

Nomenclature IX

1 Introduction 1

1.1. Motivation 1
1.2. Research objective and contributions 4
1.3. Outline 5

2 Background and state of research 7

2.1. Passive buckling of slender beam-columns 7
2.1.1. Static passive buckling 8
2.1.2. Dynamic passive buckling 12
2.2. Active buckling control 15
2.3. Uncertainty 20
2.3.1. Classification of uncertainty 20
2.3.2. Quantification of uncertainty 21
2.3.3. Uncertainty in passive buckling and active buckling control . 24
2.4. Conclusion 25

3 Active buckling control of a beam-column system 27

3.1. Concept of the beam-column system 27
3.2. Mathematical model of the beam-column system 30
3.2.1. Finite Element beam-column model 31
3.2.2. Reduced modal beam-column model 44
3.2.3. Beam-column transfer function 47
3.2.4. Beam-column plant 48

3.3. Active buckling control 51
3.3.1. Selection of the control concept 51
3.3.2. Open-loop plant 55
3.3.3. Controller weights 57
3.3.4. Controller synthesis 60

4 Experimental test setup 63

4.1. Mechanical test setup components 63
4.1.1. Test setup and beam-column with piezo-elastic supports . . . 63
4.1.2. Piezo-elastic supports 67
4.1.3. Component variation for uncertainty quantification 68
4.2. Electrical test setup components 71

5 Beam-column dynamic behavior and controller tuning 73

5.1. Experimental lateral dynamic behavior of the beam-column system . 73
5.1.1. Deterministic lateral dynamic behavior 74
5.1.2. Uncertainty in the lateral dynamic behavior 77
5.2. Calibration of the beam-column plant 80
5.2.1. Model calibration procedure 80
5.2.2. Deterministic model calibration 82
5.2.3. Model calibration considering uncertainty 86
5.3. Controller tuning 90
5.3.1. Controller weight selection 90
5.3.2. Numerical verification of the controller performance 91

6 Experimental results of passive buckling and active buckling control 95

6.1. Experimental procedure 95
6.2. Experimental results for quasi-static axial loads 99
6.2.1. Deterministic passive buckling and active buckling control . . 100
6.2.2. Uncertainty in passive buckling and active buckling control . 102
6.3. Experimental results for dynamic axial loads 106
6.3.1. Deterministic passive and active step response 106
6.3.2. Uncertainty in passive and active step response 108
6.4. Discussion of results 112

7 Conclusions and outlook 115

A Appendix 119

A.1. Probability plots 119
A.2. Controller weights 123

References **125**

List of Figures **133**

List of Tables **137**

Nomenclature

Acronyms

ADC	analog-digital conversion
BRL	Bounded Real Lemma
cdf	cumulative distribution function
DAC	digital-analog conversion
EC	electrical components
FE	finite element
LFT	linear fractional transformation
LMI	linear matrix inequality
LPV	linear parameter-varying
LQR	linear quadratic regulator
LTI	linear time invariant
LTV	linear time variant
NRMSE	normalized root mean square error
P	proportional
pdf	probability density function
PID	proportional-integral-derivative
SFB	Collaborative Research Center – Sonderforschungsbereich
SMA	shape memory alloy
ZOH	zero order hold

Latin Letters

a	weight denominator coefficient
A	cross-section area in m^2
$\boldsymbol{A}$	state space system matrix
b	weight numerator coefficient
$\boldsymbol{B}$	state space input matrix
c	constant gain

$\boldsymbol{C}$	state space output matrix
d	edge length in m
d_{33}	piezoelectric constant in m/V
$\boldsymbol{d}$	vector of disturbance end moments
$\boldsymbol{D}$	state space feedthrough matrix
$\boldsymbol{D}_\zeta$	damping matrix
E	Young's modulus in $\mathrm{N/m^2}$
f	frequency in Hz
F	force in N
G	scalar transfer function
$\boldsymbol{G}$	matrix of transfer functions
h	membrane spring element thickness in m
H	shape function
$\boldsymbol{H}$	shape function matrix
i	index variable
I	second moment of area in $\mathrm{m^4}$
j	index variable
k	translational stiffness in N/m (geometrical stiffness k_g in 1/m)
k_φ	rotational stiffness in Nm/rad
$\boldsymbol{K}$	stiffness matrix
l	length in m
L	Lyapunov function
m	mass in kg
M	bending moment in N m
$\boldsymbol{M}$	mass matrix
n	index of FE node
N	number of FE nodes or number of piezoelectric layers
p	probability density function
P	cumulative distribution function
P	beam-column plant transfer function
$\boldsymbol{p}$	vector of calibrated parameters
$\boldsymbol{P}$	beam-column plant
q	modal displacement in m
Q	quantile in %
$\boldsymbol{q}$	modal displacement vector
r	radius in m
R	interpercentile range of WEIBULL distribution
$\boldsymbol{r}$	displacement vector
$\widehat{\boldsymbol{r}}$	eigenvector

$\boldsymbol{R}$	controller transfer function
s	LAPLACE variable
S_y	yield strength in $\mathrm{N/m^2}$
t	time in s
T	time delay in s
u	control input in V
$\boldsymbol{u}$	input vector
v	translational displacement in y-direction in m
V	voltage in V
w	translational displacement in z-direction in m
W	scalar weight transfer function
$\boldsymbol{w}$	exogenous input vector
$\boldsymbol{W}$	weight transfer function matrix
x	location in x-direction in m
X	random variable
X_0	location parameter of WEIBULL distribution
$\boldsymbol{x}$	state vector
$\boldsymbol{X}$	solution of Lyapunov equation
y	measurement output in V
$\boldsymbol{y}$	output vector
$\boldsymbol{z}$	performance output vector

Greek Letters

α	proportional damping coefficient
β	shape parameter of WEIBULL distribution
δ	membrane spring element cone angle in °
Δ	normalized root mean square error
ε	surface strain in m/m
η	scale parameter of WEIBULL distribution
γ	value of $\mathscr{L}_2$-norm
Γ	upper bounds of closed-loop plants
κ	effective length factor
λ	slenderness ratio
μ	mean of normal distribution
ω	angular frequency in rad/s
Ω	excitation angular frequency in rad/s
φ	rotational displacement in °

$\boldsymbol{\Phi}$	truncated modal matrtix
ϱ	density in kg/m^3
σ	standard deviation of normal distribution
Σ	most likely value (mode) of WEIBULL distribution
θ	piezoelectric force constant in m/V
ϑ	direction of buckling in °
ζ	modal damping ratio

Indices

0	initial
a	active
A	support A
b	beam-column
B	support B
c	controller
cl	closed-loop
cn	center
cr	critical
d	disturbance
e	elastic
el	finite element
exp	experimental
ext	axial extension
E	EULER
g	geometric
l	lower
m	modal
max	maximum
ms	membrane spring element
num	numerical
N	normal distribution
ol	open-loop
p	passive
pa	piezo amplifier
pz	piezoelectric
rf	reconstruction filter
rt	real-time platform

s	sensor
sg	strain gauge amplifier
t	performance output (target)
tr	transition
u	upper
w	weighted
W	WEIBULL distribution
x	x-direction
y	y-direction
z	z-direction

Other mathematical symbols

$\mathscr{B}$	Bounded Real Lemma
$\mathscr{F}_\mathrm{l}$	lower linear fractional transformation
$\overline{(\,)}$	(properties of) mean beam-column plant
$(\,)'$	space derivative ($= \mathrm{d}/\mathrm{d}x$)
$\dot{(\,)}$	time derivative ($= \mathrm{d}/\mathrm{d}t$)

1 Introduction

Buckling of slender beam-columns subject to compressive axial loads represents a critical design constraint for lightweight mechanical load-bearing structures, e.g. truss structures. Uncertainty in the assumptions and realization of the material, geometry, loading or support properties of a beam-column system considerably reduces the maximum bearable axial load. Active buckling control may increase the maximum bearable axial load. In this thesis, uncertainty in the active buckling control of a beam-column with circular cross-section subject to quasi-static and dynamic axial loads is quantified and evaluated. In particular, the beam-column's maximum bearable axial load is increased and the lateral deflections due to quasi-static and dynamic compressive axial loads are reduced by novel piezo-elastic supports and a gain-scheduled $\mathscr{H}_\infty$ controller. Probabilistic uncertainty in the maximum bearable axial load and the beam-column lateral deflections is quantified experimentally and evaluated to investigate the feasibility of the approach for practical beam-column systems.

1.1 Motivation

Lightweight truss structures that comprise of slender members and stiff nodes are commonly used in mechanical engineering applications to distribute both (quasi-)static and dynamic loads, e.g. in aircraft landing gears or vehicle suspension struts, [95]. Slender in this context means that the length is considerably larger than the cross-sectional width of a member, which is quantified by the slenderness ratio λ (2.3). The loads are static when they are time-invariant, quasi-static when they are only slowly changing with time or dynamic when they are time-varying with arbitrary fast changes.

Commonly in real applications, the members in a truss structure are loaded axially in tension and compression, which results in a good material utilization. In compression, however, the slender members are critical to failure by buckling before the material fails, e.g. by yielding, [89]. Buckling is a stability failure with sudden large lateral deflections for compressive axial loads F_x in longitudinal x-direction exceeding the critical buckling load (index cr) $F_{x,\mathrm{cr}}$, which occurs for ideal structures

with no imperfections. Real structures, however, always exhibit uncertainty due to imperfections in the material (e.g. voids), geometry (e.g. initial curvature), loading (e.g. eccentricity) or the support properties (e.g. end moments), which may lead to bending. Therefore, real structures do not fail suddenly, but show continuous deflection for increasing compressive axial loads and, thus, are characterized by a maximum bearable axial load (index max) $F_{x,\max} \leq F_{x,\mathrm{cr}}$, [53]. Purely axially loaded members are called columns, members with axial and bending loads are called beam-columns, [89], a term that is used throughout this work.

The conventional approach to increase the critical buckling load or maximum bearable axial load of axially loaded beam-columns is to change the material, the geometry, or the supports so that the beam-column withstands higher axial loads. In this thesis, this approach is called passive, as no additional external energy is put into the system and no sensors or actuators are needed, [90]. For example, a material with higher Young's modulus, shorter or thicker beam-columns or stiffer supports may be used. However, the modifications usually lead to oversizing and are sometimes not desirable because of given design constraints.

In these cases, active buckling control may be used to increase the maximum bearable axial load of a given beam-column. In this context, active means that additional energy is put into the system and sensors as well as actuators are present, [90]. Active buckling control of slender beam-columns by additional lateral forces or bending moments has been subject of research in various numerical and experimental investigations over the last three decades, [1, 10, 11, 17, 19, 26, 27, 40, 64, 67, 88, 92, 96]. The common characteristics of the investigated beam-column systems and the utilized active buckling control found in the referenced studies are

- rectangular cross-sections with mostly pinned-pinned supports,
- relatively high slenderness ratios $\lambda \geq 350$,
- relatively low critical buckling loads $F_{x,\mathrm{cr}} \leq 143\,\mathrm{N}$,
- (quasi-)static axial loads $F_x(t) \approx$ const.,
- mostly surface bonded piezoelectric patch actuators,
- either constant or manually switched feedback or optimal controllers and
- mostly no systematic investigation of data uncertainty.

In contrast to these rather academic beam-column systems, practical beam-columns in real lightweight mechanical load-bearing structures do not have rectangular cross-sections with one relatively weak and one relatively strong direction of buckling. Instead, they rather have symmetric cross-sections with high second moment of area, e.g. circular solid or thin-walled or quadratic thin-walled cross-sections, [95]. Unlike the pinned-pinned, fixed-pinned or fixed-free supports, the connections of practical beam-columns are usually realized as relatively stiff supports, [32]. Furthermore, practical beam-columns are mostly designed with lower slenderness ratios closer to the material-dependent transition slenderness ratio (index tr) λ_{tr} (2.4) to exhibit a better material utilization, [31]. Finally, the main function of beam-columns is the transmission of axial loads that, depending on the application, may be dynamic and exceed the axial loads observed in the previous studies on active buckling control for (quasi-)static axial loads. The practical beam-column used for active buckling control in this thesis is shown in figure 1.1a), section 4.1.

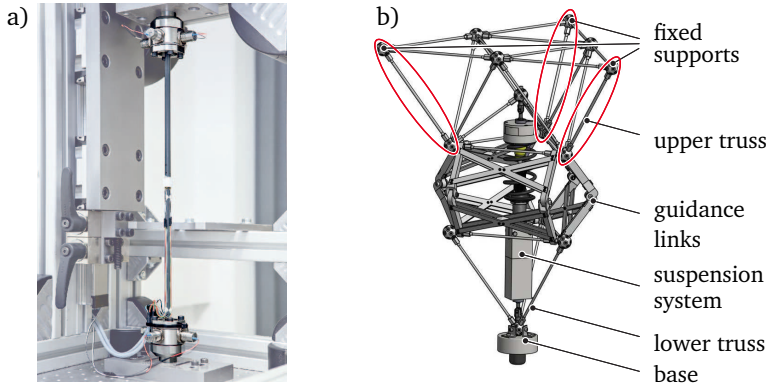

Figure 1.1.: a) Practical beam-column for active buckling control, b) modular active spring-damper system subject to dynamic loads introduced at the base, possible locations for the integration af active buckling control (——)

At the Technische Universität Darmstadt, the Collaborative Research Center (Sonderforschungsbereich SFB) 805 “Control of Uncertainty in Load-Carrying Structures in Mechanical Engineering” investigates uncertainty control solutions in the modular active spring-damper system shown in figure 1.1b) with possible locations for the integration of the practical beam-column for active buckling control. It mainly consists of an upper and lower truss structure connected by a suspension system and guidance links.

The upper truss is used to transfer and distribute quasi-static or time-varying loads introduced in the base and through the suspension system into the fixed supports. The tetrahedral truss structures consist of beam-columns with circular solid cross-section to distribute dynamic loads that exceed several kN, e.g. by impact due to drop tests, [60].

For this lightweight truss structure, the approaches for active buckling control of former studies found in literature are not applicable. For example, the use of piezoelectric patch actuators is not practical on the curved surface of beam-columns with circular cross-section, which makes a new actuator concept necessary, e.g. integrated into the supports. Also, the consideration of dynamic axial loads requires the application of more sophisticated controllers because of the significant axial load-dependency of the lateral beam-column dynamics. Finally, passive buckling and active buckling control of beam-columns are very sensitive to uncertainty. The former studies on active buckling control did not consider important sources of uncertainty, such as the assembly and mounting of the beam-column system as well as component variations by using different beam-columns and supports.

1.2 Research objective and contributions

Based on the analysis of the previous section, the following research question for this thesis is stated:

> *How much benefit is expected with a new active buckling control approach for a practical beam-column system subject to dynamic axial loads, and how much uncertainty is controlled or compensated by the active buckling control compared to the same beam-column system without active buckling control?*

In the context of this thesis, the term “practical beam-column system” refers to a beam-column with circular solid cross-section in nearly fixed-fixed supports with relatively low slenderness ratio $\lambda = 102$ and relatively high critical buckling load $F_{x,\mathrm{cr}} = 3381\,\mathrm{N}$ and dynamic axial loads $F_x(t) \neq \text{const.}$, which may be used as a member in the experimental lightweight truss structure from [60].

The investigated system is a beam-column with circular solid cross-section, supported by novel piezo-elastic supports with integrated piezoelectric stack actuators. A mathematical linear parameter-varying (LPV) model of the beam-column system is set up and calibrated with experimental data from a representative sample of nominally identical beam-column systems. The resulting mean LPV model obtained from normally distributed model parameters is used to design a gain-scheduled $\mathscr{H}_\infty$

buckling controller. The feasibility of the controller is verified numerically and in the experimental test setup with quasi-static and dynamic axial loads. Probabilistic data uncertainty in the maximum bearable axial load and in the beam-column lateral deflections are quantified and evaluated experimentally by three-parameter WEIBULL distributions for the passive beam-column system, without active buckling control, and the active beam-column system, with active buckling control.

Summarized, the objectives of this thesis are:

1. Active buckling control of a beam-column with circular solid cross-section subject to dynamic axial loads in arbitrary lateral direction using innovative piezo-elastic supports and LPV control.
2. Experimental quantification and evaluation of probabilistic uncertainty in the maximum bearable axial loads and lateral deflections of the passive and active beam-column systems and subsequent comparison of the passive and active results.

1.3 Outline

The outline of this thesis is as follows:

Chapter 2 provides the background and state of research for the passive buckling and active buckling control of slender beam-columns as well as for the quantification of uncertainty.

Chapter 3 presents the mathematical models of the beam-column system and the controller for active buckling control.

Chapter 4 presents the experimental realization of the beam-column system and test setup. Both, the mechanical and electrical components as well as the signal processing and measurement setup are discussed.

Chapter 5 shows the calibration of the model derived in chapter 3 for the uncertain experimental lateral dynamic beam-column dynamics. The resulting mean beam-column model is used for controller tuning.

Chapter 6 presents the experimental results of the passive buckling and active buckling control for quasi-static and dynamic axial loads. The probabilistic uncertainty in the experimental results is quantified, evaluated and compared for the passive and active beam-column system.

Chapter 7 finally summarizes the results of the thesis and provides an outlook on future research.

2 Background and state of research

This chapter presents the theoretical background and state of research of the relevant topics covered in this thesis. First, the theoretical background on static and dynamic buckling of passive slender beam-columns is presented. Second, the state of research on active buckling control is discussed. Third, the classification and quantification of uncertainty, as used throughout this thesis, as well as uncertainty in passive buckling and active buckling control are presented. Finally, conclusions are drawn from the state of research to motivate the investigations in this thesis.

2.1 Passive buckling of slender beam-columns

Figure 2.1 shows the elastically supported beam-column used to explain the theory of static and dynamic buckling of passive ideal and real, slender beam-columns.

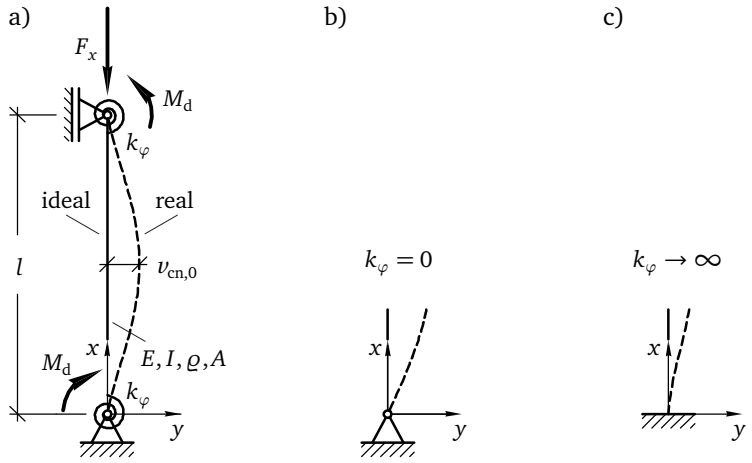

Figure 2.1.: Beam-column subject to axial load $F_x(t)$ with rotational support stiffness k_φ for buckling analysis, a) ideal, straight (——) with $\{M_\mathrm{d}, v_{\mathrm{cn},0}\} = 0$ and real, initially deflected (– –) with $\{M_\mathrm{d}, v_{\mathrm{cn},0}\} \neq 0$, b) pinned support with $k_\varphi = 0$, c) fixed support with $k_\varphi \to \infty$

Furthermore, it is used to investigate the influence of different boundary conditions and imperfections on passive buckling. Only beam-column deflections $v(x)$ in the lateral y-direction are considered and displayed at this point. In this thesis, the term passive buckling refers to the different types of failure associated with slender beam-columns subject to static $F_x(t) = \text{const.}$, section 2.1.1, or dynamic axial loads $F_x(t) \neq \text{const.}$, section 2.1.2, without input of external energy.

In figure 2.1, the beam-column with length l, Young's modulus E, second moment of area I, density ϱ and cross-section area A is pinned with additional rotational support stiffness k_φ around the z-axis, which is assumed to be equal at $x = 0$ and $x = l$. The rotational support stiffness k_φ in both supports can vary between 0 for an ideally pinned, figure 2.1b), and ∞ for an ideally fixed support, figure 2.1c). The beam-column is subject to the static or dynamic axial load $F_x(t)$, which acts on the upper support at $x = l$.

Equal and constant disturbance end moments M_d (index d) act in opposite directions at the lower and upper support to represent imperfections that lead to an intial lateral deflection of the unloaded beam-column, $F_x = 0$. The lateral deflection $v(x)$ depends on the longitudinal x-position along the beam-column and the magnitude of the disturbance end moments. As M_d and the boundary conditions are symmetric, the maximum initial (index 0) deflection is in the beam-column center (index cn) $v_{\mathrm{cn},0} = v\,(x{=}l/2, F_x{=}0, M_\mathrm{d})$. The ideal beam-column with $M_\mathrm{d} = 0$ initially is perfectly straight, $v_{\mathrm{cn},0} = 0$. In contrast, the real imperfect beam-column with $M_\mathrm{d} \neq 0$ is initially deformed, $v_{\mathrm{cn},0} \neq 0$. In the following, first, the theory of static buckling for passive, ideal and real slender beam-columns is presented. Second, the theory of dynamic buckling is presented.

2.1.1 Static passive buckling

The theory of static passive buckling has been thoroughly investigated for both ideal and real beam-columns and is presented in the following.

Ideal beam-column

First investigations on the theory of static buckling for an ideal slender beam-column were published by Euler [29] and since then many publications followed, [38, 48, 89]. Buckling of the ideal beam-column in figure 2.1 is a stability failure with large lateral deflections $v_\mathrm{cn}(F_x)$ for constant compressive axial loads $F_x = \text{const.}$ exactly at the critical buckling load $F_{x,\mathrm{cr}}$. For axial loads $F_x < F_{x,\mathrm{cr}}$, the ideal beam-column remains straight and does not deform, $v_\mathrm{cn}(F_x < F_{x,\mathrm{cr}}) = 0$.

To calculate the critical buckling load, the homogeneous differential equation

$$EI\, v^{IV}(x) + F_x\, v''(x) = 0, \tag{2.1}$$

[38], is solved for the elastic boundary conditions in figure 2.1, [74]. The smallest solution of the resulting eigenvalue problem is the critical buckling load

$$F_{x,\mathrm{cr}} = \frac{\pi^2 EI}{\left(\kappa(k_\varphi)\, l\right)^2}, \tag{2.2}$$

which corresponds to the first mode of buckling. The higher modes of buckling with their respective buckling loads are also obtained by solution of the eigenvalue problem. However, the critical buckling load is relevant for the beam-column failure by linear elastic buckling due to static axial loads F_x.

In (2.2), $\kappa(k_\varphi)$ is the effective length factor, representing the beam-column's type of boundary conditions, e.g. pinned-pinned, elastic-elastic or fixed-fixed, figure 2.1, [31, 89]. It determines the dimensionless slenderness ratio

$$\lambda = \kappa(k_\varphi)\, l \sqrt{\frac{A}{I}} = \pi \sqrt{\frac{EA}{F_{x,\mathrm{cr}}}}, \tag{2.3}$$

which includes both information on geometry and boundary conditions and, in general and in this thesis, is used to compare the buckling behavior of different beam-column systems, [89]. Failure by buckling according to (2.2) occurs for beam-columns with slenderness ratios exceeding the transition slenderness ratio

$$\lambda_{\mathrm{tr}} = \pi \sqrt{\frac{E}{S_{\mathrm{y}}}}, \tag{2.4}$$

with the Young's modulus E and the yield strength S_{y}. Thus, the transition slenderness ratio λ_{tr} characterizes the transition between linear elastic buckling of slender or long beam-columns for $\lambda > \lambda_{\mathrm{tr}}$ and material yielding of short beam-columns for $\lambda < \lambda_{\mathrm{tr}}$, [53]. Typical transition slenderness ratios for aluminum and steel are $\lambda_{\mathrm{tr,al}} \approx 60$ and $\lambda_{\mathrm{tr,st}} \approx 100$, [53, 95].

As can be seen from (2.2), the critical buckling load $F_{x,\mathrm{cr}}$ of the passive beam-column may be increased by either

- increasing the Young's modulus E,

- increasing the second moment of area I,
- reducing the beam-column length l or
- reducing the effective length factor $\kappa(k_\varphi)$.

In case the material and geometry, respectively E, I and l, are fixed, the boundary conditions determine the resulting critical buckling load $F_{x,\mathrm{cr}}$. For the pinned-pinned beam-column in figure 2.1b), the effective length factor is $\kappa(k_\varphi = 0) = 1$, representing the well-known EULER buckling case II, [38]. For the fixed-fixed beam-column in figure 2.1c), it is $\kappa(k_\varphi \to \infty) = 0.5$, representing EULER buckling case IV with a four times higher critical buckling load, [38]. In this thesis, the EULER buckling loads (index E)

$$F_{x,\text{E-II}} = \frac{\pi^2 EI}{(1\,l)^2} \qquad \text{and} \qquad F_{x,\text{E-IV}} = \frac{\pi^2 EI}{(0.5\,l)^2} = 4 \cdot F_{x,\text{E-II}} \tag{2.5}$$

for EULER buckling cases II and IV are used as references for the calculated critical buckling load depending on the rotational stiffness k_φ, as they are the minimum and maximum possible critical buckling loads for the elastically supported beam-column in figure 2.1. Figure 2.2 shows the critical buckling load $F_{x,\mathrm{cr}}(k_\varphi)$ normalized to $F_{x,\text{E-II}}$ and plotted versus the rotational support stiffness k_φ normalized to the beam-column's relative flexural stiffness EI/l, [5, 87].

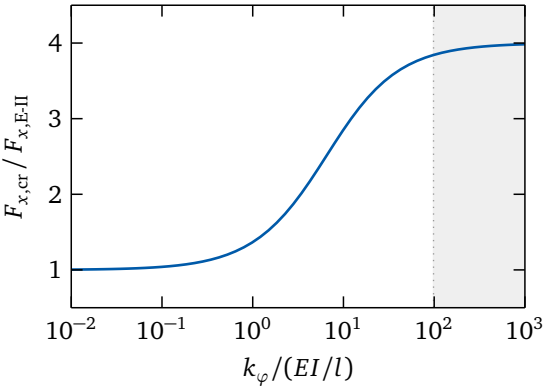

Figure 2.2.: Normalized critical buckling load $F_{x,\mathrm{cr}}/F_{x,\text{E-II}}$ versus normalized rotational support stiffness $k_\varphi/(EI/l)$ with range of normalized rotational support stiffness $k_\varphi/(EI/l)$ close to fixed-fixed boundary conditions ( )

As can be seen, the critical buckling load can be increased considerably by stiffening the supports. In order to achieve the maximum possible critical buckling load $F_{x,\mathrm{cr}}$ (2.2) of the passive beam-column, the boundary conditions for the active buckling control in this thesis are close to fixed-fixed supports, as indicated in the grey area in figure 2.2, section 5.2.

Real beam-columns

As presented in section 1.1, real beam-columns always show some form of imperfections that cause them to fail before the critical buckling load $F_{x,\mathrm{cr}}$ (2.2) is reached. Different imperfections in the material, e.g. voids, geometry, e.g. initial curvature, loading, e.g. eccentricity, or the supports, e.g. end moments, can occur separately or combined, [31, 89].

In the elastically supported beam-column from figure 2.1, the imperfections are represented by the disturbance end moments M_{d} that cause the beam-column to deflect laterally. The initial lateral center deflection of an unloaded, pinned-pinned beam-column, figure 2.1b), is given by

$$v_{\mathrm{cn},0}(M_{\mathrm{d}}) = v_{\mathrm{cn}}(F_x = 0, M_{\mathrm{d}}) = \frac{M_{\mathrm{d}}\, l^2}{8\, EI}, \tag{2.6}$$

[89]. The axial load on the beam-column amplifies the initial deflection due to the additional bending moment that is generated. The resulting axial load-dependent deflection of the beam-column center is approximated by

$$v_{\mathrm{cn}}(F_x, M_{\mathrm{d}}) \approx \frac{v_{\mathrm{cn},0}}{1 - F_x/F_{x,\mathrm{cr}}}, \tag{2.7}$$

where the term $(1 - F_x/F_{x,\mathrm{cr}})^{-1}$ is the amplification factor, [31, 89]. Figure 2.3 shows the load-deflection curves for the ideal and real beam-column from figure 2.1 for different degrees of imperfection, represented by M_{d}. The ideal beam-column has no initial lateral center deflection and remains straight for axial loads $F_x < F_{x,\mathrm{cr}}$. At the critical buckling load $F_{x,\mathrm{cr}}$, the lateral center deflection grows infinitely and the beam-column buckles.

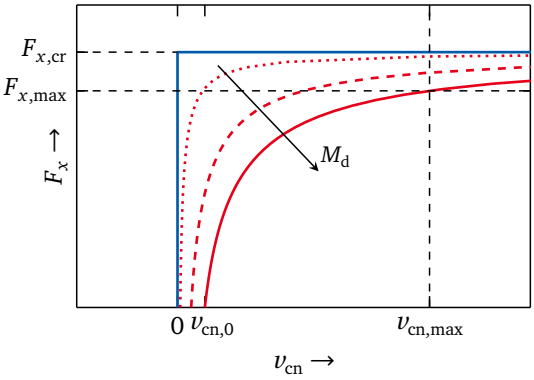

Figure 2.3.: Beam-column center deflection $v_\mathrm{cn}(F_x, M_\mathrm{d})$ versus axial load F_x for ideal (——) and real beam-columns with increasing disturbance M_d (——) > (– –) > (·····)

The real beam-column does not fail suddenly, it shows non-linearly increasing lateral center deflection for increasing axial loads according to (2.7). When F_x approaches the critical buckling load $F_{x,\mathrm{cr}}$, the amplification factor goes to infinity, so that $F_{x,\mathrm{cr}}$ is never reached. Therefore, a maximum bearable axial load $F_{x,\mathrm{max}} \leq F_{x,\mathrm{cr}}$ is defined instead of a critical buckling load $F_{x,\mathrm{cr}}$. It is defined as the axial load, where the beam-column center has reached the maximum admissible lateral center deflection $v_{\mathrm{c,max}}$. For increasing disturbance bending moments M_d, the initial lateral center deflection $v_{\mathrm{cn},0}$ increases and, thus, the maximum bearable axial load $F_{x,\mathrm{max}}$ is reduced. To achieve high values for $F_{x,\mathrm{max}}$, the initial lateral center deflections have to be small, which, therefore, is defined as the goal of active buckling control.

2.1.2 Dynamic passive buckling

The buckling behavior of axially loaded beam-columns is closely related to their lateral dynamic vibration behavior. The homogeneous differential equation of lateral beam-column vibrations in y-direction according to figure 2.1 is

$$\varrho A\, \ddot{v}(x,t) + EI\, v^{IV}(x,t) + F_x(t)\, v''(x,t) = 0, \tag{2.8}$$

[91]. In comparison to the static differential equation (2.1), the beam-column inertia and the dependency of time t are added. Equation (2.8) is the basis for the axial load-dependent beam-column model for model-based controller synthesis in the studies on active buckling control, section 2.2, and in this thesis, section 3.2.

An important property of the axially loaded beam-column in figure 2.1 are the resonance frequencies with the n-th resonance frequency of the continuous beam-column $f_n(F_x, k_\varphi)$ for $n = 1 \rightarrow \infty$, which are dependent on the axial load F_x and on the support stiffness k_φ. They are obtained by solving the characteristic equation of lateral beam-column vibrations derived from (2.8), [61, 75]. The first resonance frequencies of the unloaded beam-column with pinned-pinned, EULER buckling case II, and fixed-fixed boundary conditions, EULER buckling case IV, are

$$f_{1,\text{E-II}} = \frac{\pi}{2}\sqrt{\frac{EI}{\varrho A l^4}} \qquad \text{and} \qquad f_{1,\text{E-IV}} = 2.27 \cdot f_{1,\text{E-II}}, \tag{2.9}$$

[91]. Figure 2.4a) shows the normalized first resonance frequency of the unloaded beam-column $f_1(F_x = 0)/f_{1,\text{E-II}}$ plotted versus the normalized rotational support stiffness $k_\varphi/(EI/l)$. The EULER buckling cases II and IV represent the minimum and maximum resonance frequencies of the unloaded beam-column.

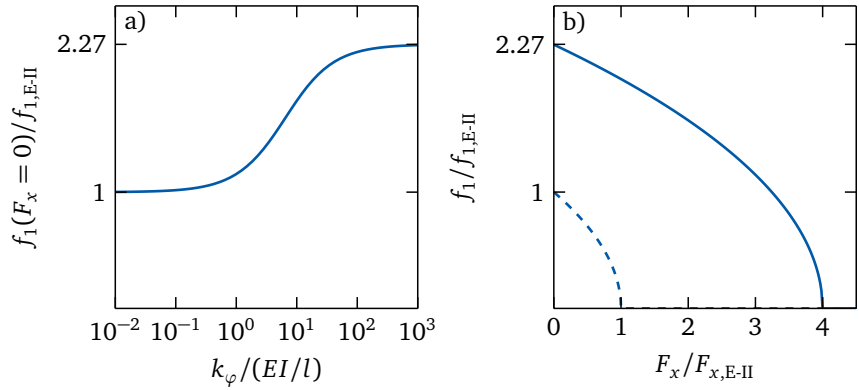

Figure 2.4.: Normalized first resonance frequency $f_1/f_{1,\text{E-II}}$ versus a) normalized rotational support stiffness $k_\varphi/(EI/l)$ for $F_x = 0$, b) normalized axial load $F_x/F_{x,\text{E-II}}$ for pinned-pinned (——) and fixed-fixed (– –) boundary conditions

The axial compressive load reduces the lateral structural stiffness and, thus, also the resonance frequencies $f_n(F_x, k_\varphi)$, [13]. Figure 2.4b) shows the normalized first resonance frequency $f_1(F_x)/f_{1,\text{E-II}}$ plotted versus the normalized axial load $F_x/F_{x,\text{E-II}}$ for pinned-pinned and fixed-fixed boundary conditions. The first resonance frequency $f_1(F_x, k_\varphi)$ reduces to zero for the critical buckling load $F_{x,\text{cr}}$. This can be observed in the dynamic beam-column behavior for different static axial loads $F_x = \text{const.}$, section 5.1, and for quasi-statically increasing axial load $F_x \approx \text{const.}$, section 6.2.

For other forms of dynamic axial loads, the buckling behavior is fundamentally different from static EULER buckling. In the following, three types of dynamic buckling that have commonly been covered in literature are discussed:

- vibration buckling,
- impulse buckling and
- buckling of suddenly loaded beam-columns.

Vibration buckling, also known as parametric resonance, occurs for a harmonic axial load of the form $F_x(t) = F_{x,0} + F_{x,1} \cos(\Omega t)$ with excitation frequency Ω, amplitude $F_{x,1}$ and offset $F_{x,0}$, as first presented in [86]. Depending on the combination of $F_{x,0}$, $F_{x,1}$ and Ω, the system can be stable for axial loads exceeding the critical buckling load $F_{x,0} > F_{x,\mathrm{cr}}$ or also instable for axial loads below the critical buckling load $F_{x,0} < F_{x,\mathrm{cr}}$, [14]. Regions of stability or instability are illustrated in stability maps, [57, 89].

Impulse buckling describes the buckling of beam-columns due to impulse loads that are characterized by an impulse magnitude and duration, as first presented in [49]. Due to the delayed effect of the beam-column inertia, the maximum impulse load may significantly exceed the static critical buckling load $F_{x,\mathrm{cr}}$. For a long impulse duration, buckling occurs in form of the fundamental first mode of buckling at $F_{x,\mathrm{cr}}$ (2.2). For a short impulse duration, higher modes of buckling are excited and higher axial loads are sustained, especially for beam-columns with high slenderness ratios λ and small imperfections, [31, 55]. In impulse buckling, the axial load disappears after the impulse duration, followed by free lateral vibrations of the beam-column.

Buckling of suddenly loaded beam-columns may occur for axial step loads with constant magnitude $F_{x,\mathrm{step}}$ and infinite duration, [84]. It is not a stability failure as it assumes the beam-column to have some initial imperfections that are amplified by the axial load. For small axial step loads $F_{x,\mathrm{step}} \ll F_{x,\mathrm{cr}}$, the beam-column vibrates about the new equilibrium position. For axial step loads approaching the critical buckling load $F_{x,\mathrm{cr}}$ (2.2), the vibrations grow, as in the static case according to (2.7), so that a maximum allowable deflection $v_{\max}$ for the vibration amplitudes may be defined. The static critical buckling load $F_{x,\mathrm{cr}}$ (2.2) is always the upper limit for step-shaped axial loads, [50].

In this thesis, step-shaped dynamic axial loads are considered to occur as load scenarios in practical beam-columns as e.g. in drop tests of the modular active spring-damper system shown in figure 1.1b), [60]. Harmonic and impulse axial loads are not further investigated as load scenarios for the beam-column system. Thus, the term dynamic axial load refers to axial step loads in the following.

2.2 Active buckling control

In the previous section, passive buckling and passive approaches to increase the critical buckling load $F_{x,\mathrm{cr}}$ (2.2) of an ideal beam-column or the maximum bearable axial load $F_{x,\max}$, figure 2.3, of a real beam-column were presented. Active buckling control is a different approach to increase the maximum bearable axial load of a given beam-column.

The goal of active buckling control is to increase the active maximum bearable axial load $F_{x,\max,\mathrm{a}}$ above the critical buckling load $F_{x,\mathrm{cr}}$ (2.2) of an ideal beam-column system or above the passive maximum bearable axial load $F_{x,\max,\mathrm{p}}$ of a real beam-column system, as shown in figure 2.3. Generally, a beam-column system for active buckling control consists of the supported beam-column with sensors to measure the lateral deflection and actuators to introduce forces or bending moments as well as the electrical components for signal processing. By adding a controller to connect the beam-column system's measurement outputs with the control inputs, active buckling control is achieved.

In literature, shape memory alloys (SMA) and piezoelectric materials have so far been used as actuators for active buckling control of slender beam-columns. A number of experimental studies investigated active buckling control of beam-columns with external or embedded SMA wires or springs against quasi-static axial loads, [1, 19, 40]. A drawback of SMA actuators, however, are the slow response times that make the use only suitable for quasi-static axial loads, [46, 52].

Most studies used piezoelectric patch or stack actuators for active buckling control of beam-columns with rectangular cross-sections, [10, 11, 17, 26, 27, 64, 67, 88, 92, 96]. They make use of the inverse piezoelectric effect, where electrical voltages applied to the electrodes of a piezoelectric actuator result in a deformation, [66, 72]. In the following, first, numerical and, second, experimental studies on the active buckling control of beam-columns with rectangular cross-sections by piezoelectric actuators are reviewed.

Numerical studies

The beam-column systems in the numerical studies considered ideal beam-columns loaded by static axial loads $F_x(t) = \text{const.}$, which are characterized by the slenderness ratio λ (2.3) calculated for the beam-column without actuators and the critical buckling load $F_{x,\mathrm{cr}}$ (2.2).

MERESSI AND PADEN [64] numerically simulated the active buckling control of a pinned-pinned beam-column with slenderness ratio $\lambda = 530$, critical buckling load $F_{x,\mathrm{cr}} = 5\,\mathrm{N}$ and piezoelectric patch actuators along the entire length. A linear quadratic regulator (LQR) stabilized the beam-column for non-zero initial deflection and increased the maximum bearable axial load by 280%.

WANG [92] numerically simulated the active buckling control of a beam-column with the same slenderness ratio and critical buckling load as in [64], but with discrete piezo patches at two beam-column positions. An LQR controller designed for two separate axial loads stabilized the beam-column for non-zero initial deflection and increased the maximum bearable axial load by 780%.

MUKHERJEE AND CHAUDHURI [68] numerically simulated the active buckling control of a pinned-pinned beam-column with slenderness ratio $\lambda = 346$, critical buckling load $F_{x,\mathrm{cr}} = 143\,\mathrm{N}$ and piezoelectric patch actuators along the entire length. A proportional (P) controller stabilized the beam-column with initial deflection and increased the maximum bearable axial load by 90%.

Table 2.1 summarizes the presented numerical investigations by their supports, the used controller, slenderness ratio λ, critical buckling load $F_{x,\mathrm{cr}}$ and active (index a) maximum bearable axial load $F_{x,\mathrm{max,a}}$.

Table 2.1.: Numerical studies on active buckling control

source	supports	controller	λ	$F_{x,\mathrm{cr}}/\mathrm{N}$	$F_{x,\mathrm{max,a}}/\mathrm{N}$
[64]	pinned-pinned	LQR	530	5	19
[92]	pinned-pinned	LQR	530	5	44
[67]	pinned-pinned	P	350	143	272

Especially the studies [64, 92] show a significant relative increase in the active maximum bearable axial loads $F_{x,\mathrm{max,a}}$. The approaches, however, only simulated active buckling control of non-zero initial lateral beam-column deflections that are compensated by the controller after a short period of time with no further necessary control. The active buckling control for constant disturbance end moments to represent imperfections, as shown in figure 2.1 and investigated in this thesis, has not been demonstrated and is expected to yield worse results.

Experimental studies

The beam-column systems investigated in the experimental studies are real beam-columns loaded by quasi-static axial loads $F_x(t) \approx \text{const.}$, which are again characterized by the slenderness ratio λ (2.3) calculated for the beam-column without actuators. Instead of the critical buckling load $F_{x,\text{cr}}$ for ideal beam-columns, the passive (index p) maximum bearable axial load $F_{x,\text{max,p}}$ according to figure 2.3 is used to characterize the passive beam-column systems.

Berlin [10] experimentally investigated the active buckling control of a pinned-pinned steel beam-column with slenderness ratio $\lambda = 4420$, passive maximum bearable axial load $F_{x,\text{max,p}} = 5\,\text{N}$ and five pairs of piezoelectric patch actuators attached along the beam-column. A proportional-integral-derivative (PID) controller increased the maximum bearable axial load by up to 460%.

Thompson and Loughlan [88] experimentally investigated the active buckling control of pinned-pinned carbon-epoxy composite beam-columns with slenderness ratio $\lambda = 970$, passive maximum bearable axial load $F_{x,\text{max,p}} = 10\,\text{N}$ and piezoelectric patch actuators in the beam-column center. A P controller increased the maximum bearable axial load by up to 37%.

Berlin [11] and Chase [17] experimentally investigated the active buckling control of a pinned-pinned fiberglass beam-column with slenderness ratio $\lambda = 670$, passive maximum bearable axial load $F_{x,\text{max,p}} = 45\,\text{N}$ and piezoelectric patch actuators attached along the entire surface. An LQR controller increased the maximum bearable axial load by up to 190%.

Zenz and Humer [96] experimentally investigated the active buckling control of a fixed-free steel beam-column subject to a follower axial load with slenderness ratio $\lambda = 1770$, passive maximum bearable axial load $F_{x,\text{max,p}} = 74\,\text{N}$ and twelve pairs of piezoelectric patch actuators attached along the beam-column. A P controller increased the maximum bearable axial load by up to 105%.

In all these studies, the piezoelectric patch actuators for active buckling control significantly influence the beam-column's slenderness ratio and lateral dynamic behavior. Another approach, therefore, uses piezoelectric stack actuators, which apply active lateral forces to the beam-column.

Enss [26, 27] experimentally investigated the active buckling control of a fixed-pinned steel beam-column with slenderness ratio $\lambda = 725$, passive maximum bearable axial load $F_{x,\text{max,p}} = 30\,\text{N}$ and piezoelectric stack actuators near the fixed beam-column base. This way, the surface was kept free of piezoelectric patch actuators. LQR controllers that were designed for three different constant axial loads $F_{x,1/2/3}$ increased the maximum bearable axial load by up to 40%.

Table 2.2 summarizes the presented experimental investigations by their supports, the used controller, slenderness ratio λ, passive maximum bearable axial load $F_{x,\mathrm{max,p}}$ and active maximum bearable axial load $F_{x,\mathrm{max,a}}$.

Table 2.2.: Experimental studies on active buckling control

source	supports	controller	λ	$F_{x,\mathrm{max,p}}$/N	$F_{x,\mathrm{max,a}}$/N
[10]	pinned-pinned	PID	4420	5	28
[88]	pinned-pinned	P	970	10	14
[11, 17]	pinned-pinned	LQR	670	45	130
[96]	fixed-free	P	1770	74	151
[26]	fixed-pinned	LQR	725	30	42

In contrast to the investigated and presented beam-column systems, most practical beam-columns for the use in mechanical lightweight structures do not have rectangular cross-sections with one relatively weak and one relatively strong direction of buckling. Instead, they rather have symmetric cross-sections with high second moment of area, e.g. circular solid or thin-walled or quadratic thin-walled cross-sections, [95]. To the authors' knowledge, active buckling control of beam-columns with circular cross-section, as used in this thesis, has not yet been investigated except in own works, [76–78].

Unlike the pinned-pinned, fixed-pinned or fixed-free supports, the connections of practical beam-columns are usually realized as stiff supports, [32]. Furthermore, practical beam-columns are mostly designed to have slenderness ratios closer to the transition slenderness ratio λ_{tr} (2.4) so that they exhibit a better material utilization, [31]. The beam-column systems of the studies referenced in tables 2.1 and 2.2 have slenderness ratios $\lambda \geq 350$ according to (2.3), which significantly exceeds these typical values, in contrast to the beam-column system used in this thesis with $\lambda = 102$, section 5.2.3.

Finally, the main function of beam-columns is the transmission of axial loads, that, depending on the application, may be dynamic and considerably exceed the critical buckling and maximum bearable axial loads $F_{x,\mathrm{cr}} \,|\, F_{x,\mathrm{max,p}} \leq 143\,\mathrm{N}$ observed in the reviewed studies on active buckling control, tables 2.1 and 2.2. The beam-column system used in this thesis has a critical buckling load of $F_{x,\mathrm{cr}} = 3381\,\mathrm{N}$, section 5.2.3 and a passive maximum bearable axial load of $F_{x,\mathrm{max,p}} = 2644\,\mathrm{N}$, which is significantly higher.

For the obvious differences of the investigated beam-column systems to practical beam-columns regarding the cross-section, supports, slenderness ratios, critical buckling loads and applied axial loads, the investigated beam-column systems are considered to be academic, whereas the beam-column system used in this thesis is considered to be practical.

Except for [26, 27], single or multiple piezoelectric patch actuators were applied to the beam-column surface to introduce distributed bending moments for active buckling control. This, however, results in a significant modification of the original beam-column. Furthermore, the application of piezoelectric patch actuators is not possible on the curved surface of a beam-column with circular cross-section, as investigated in this thesis. Therefore, a new concept for beam-column supports with integrated piezoelectric stack actuators is used in this work, section 4.1.2.

Finally, all discussed studies used either classic feedback controllers (P, PID), which do not require a beam-column model for controller synthesis, or optimal controllers (LQR), which use a beam-column model for controller synthesis. These linear time invariant (LTI) controllers, which were designed for a given axial load F_x or design point, respectively, were either used for a large operation range of axial loads or were discretely switched for quasi-statically increasing axial load $F_x(t) \approx \text{const}$. These control concepts, however, are not feasible for dynamic axial loads $F_x(t) \neq \text{const.}$, as investigated in this thesis. Instead, an LPV controller is proposed for active bucking control in section 3.3.1.

The highest relative experimental increase in the active maximum bearable axial load $F_{x,\max,a}$ of 460% was observed in [10] for a PID controller with integral action, table 2.2. By inclusion of the integral action, the controller is able to compensate static disturbances, which occur in the form of imperfections in the beam-column system, figure 2.1. Thus, the lateral deflection of the beam-column is reduced and higher maximum bearable axial loads are achieved. Despite the mentioned advantages, the other studies on active buckling control referenced in tables 2.1 and 2.2 do not include integral action. In this thesis and in earlier own works, [76], integral action is included in the controller design, in order to compensate the static lateral deflections, sections 3.3.1 and 5.3.1.

2.3 Uncertainty

In order to compare the passive buckling with the active buckling control within this work, uncertainty in the lateral deflections and the maximum bearable axial loads is quantified and evaluated for the passive and active case. The basis for the experimental uncertainty quantification in this thesis are the classification of uncertainty used in the SFB 805, section 2.3.1, and the probability distributions and probabilistic measures to quantify and evaluate uncertainty, section 2.3.2. Based on that, the state of research on uncertainty in the passive buckling and active buckling control of beam-column systems is presented, section 2.3.3.

2.3.1 Classification of uncertainty

Within the SFB 805, a holistic approach to describe, evaluate and control uncertainty in load-carrying systems in mechanical engineering along the entire product life, i.e. design, production and usage, has been developed, [23, 41, 42]. According to the SFB's working hypothesis, "uncertainty occurs when process properties of a system can not, or only partially be determined", [23]. As part of the ongoing work, a classification of uncertainty has been established that distinguishes between

- data uncertainty and
- model uncertainty.

Data uncertainty is the variation of model parameters and states, e.g. geometric and stiffness properties, displacements, loads, etc., but also of characteristic (empirical) system values, e.g. eigenfrequencies, critical buckling loads, etc. Data uncertainty may originate from various sources, such as manufacturing inaccuracies, assembly, measurement noise, etc. It is divided into three separate categories with increasing knowledge about the respective data, [25, 69]:

- **Disregarded uncertainty** refers to deterministic data that has no associated information on its variation.
- **Non-probabilistic uncertainty** refers to non-deterministic data with known or assumed intervals or membership functions with lower and upper limits.
- **Probabilistic uncertainty** refers to non-deterministic data with known or assumed continuous probability distributions that can be described by probabilistic measures.

Model uncertainty is the discrepancy of a model from the relevant reality and may originate from any assumptions, abstractions or simplifications during modeling, e.g. by unmodelled non-linearities, time variance, higher dynamics, spillover, etc., [60].

In this thesis, probabilistic uncertainty in the model parameters for model calibration, section 5.2, and the maximum bearable axial loads and lateral beam-column deflections observed in experimental passive buckling and active buckling control, sections 6.2.2 and 6.3.2, is quantified and evaluated. Model uncertainty is not considered. The following section presents the mathematical measures to quantify probabilistic uncertainty.

2.3.2 Quantification of uncertainty

Probabilistic data uncertainty is used to describe the variation of a random variable X that is given by an empirical sample. The variation can be illustrated either by histograms, which show the frequency of observations in a given range of values (bin), or empirical cumulative distribution functions (cdf), which shows each single observation as a step function, figure 2.5, [18].

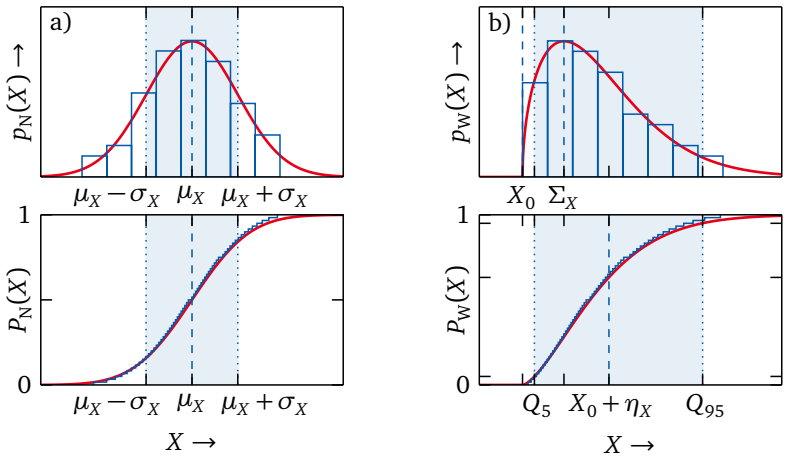

Figure 2.5.: Probability distributions of random variable X a) normal distribution, b) WEIBULL distribution with $\beta_X = 1.5$: Normalized histograms (——) and fitted pdf $p(X)$ (——) (top) and empirical (——) and fitted cdf $P(X)$ (——) (bottom) with indicated variability ( )

The empirical sample may be approximated by a continuous probability distribution. However, the suitability of a specific probability distribution has to be substantiated by statistical tests, e.g. graphically by probability plots, [18]. The histogram is approximated by the continuous probability density function (pdf) $p(X)$ and the empirical cdf is approximated by the continuous cdf, figure 2.5, given by

$$P(X) = \int_{-\infty}^{X} p(s)\,\mathrm{d}s. \tag{2.10}$$

In this thesis, two different types of probability distributions are used, the normal distribution (index N) and the WEIBULL distribution (index W), which are presented in the following. Probabilistic measures are used to describe the location (central tendency) and variability (dispersion) of the probability distributions to quantify and evaluate the probabilistic uncertainty of the random variable X.

Normal distribution

In this thesis, the model parameters that are used for the model calibration of 30 nominally identical beam-column systems, section 5.2, are approximated by normal distributions, as shown in figure 2.5a). The pdf of the normally distributed random variable X is given by

$$p_{\mathrm{N}}(X) = \frac{1}{\sqrt{2\pi\,\sigma_X^2}}\,\exp\left(-\frac{(X-\mu_X)^2}{2\sigma_X^2}\right), \tag{2.11}$$

[18]. For an empirical sample of size N, the mean μ_X and the standard deviation σ_X are

$$\mu_X = \frac{1}{N}\sum_{n=1}^{N} X_N \qquad \text{and} \qquad \sigma_X^2 = \frac{1}{N-1}\sum_{n=1}^{N}(X_N-\mu_X)^2. \tag{2.12}$$

The probabilistic measure for the location of the normal distribution is the mean. The variability is measured by the standard deviation, e.g. by the $2\,\sigma$ interval around the mean, which contains 68.2% of all observations as shown in figure 2.5a).

WEIBULL distribution

In this thesis, the maximum bearable axial loads and lateral deflections of the passive and active beam-column systems are approximated by three-parameter WEIBULL distributions, as shown in figure 2.5b), sections 6.2.2 and 6.3.2, [94]. The WEIBULL distribution is a common probability distribution in reliability analysis to describe component failures since different types of failure can be represented, [12]. However, the WEIBULL distribution can also be used to describe other observations. The pdf of the WEIBULL distributed random variable X is given by

$$p_{\mathrm{W}}(X) = \frac{\beta_X}{\eta_X}\left(\frac{X - X_0}{\eta_X}\right)^{\beta_X - 1} \exp\left(-\left(\frac{X - X_0}{\eta_X}\right)^{\beta_X}\right), \tag{2.13}$$

[12, 51]. The three-parameter WEIBULL distribution is characterized by

- shape parameter β_X,
- scale parameter η_X and
- location parameter X_0.

The shape parameter β_X defines the skewness and, thus, the asymmetry of the WEIBULL distribution. Typical values of the shape parameter β_X in reliability analysis lie in the range of $0 \leq \beta_X \leq 5$, [12]. The WEIBULL pdf is positively skewed, i.e. asymmetric with most observations on the left part of the curve, for a shape parameter $\beta_X < 3.5$, symmetric resembling the normal distribution for $\beta_X \approx 3.5$ and negatively skewed, i.e. asymmetric with most observations on the right part of the curve, for a shape parameter $\beta_X > 3.5$.

Figure 2.5b) shows the WEIBULL pdf and cdf for $\beta_X = 1.5$ with positive skewness. The scale parameter η_X is the value of X where 63.2% of all observations have occurred, independent from the shape parameter β_X. This value is shifted by the location parameter X_0, up to which the probability of an observation is zero, figure 2.5b). In the case $X_0 = 0$, (2.13) simplifies to the two-parameter WEIBULL distribution.

A probabilistic measure for the location of the WEIBULL distribution is chosen as the most likely value (mode)

$$\Sigma_X = X_0 + \eta_X \left(1 - \frac{1}{\beta_X}\right)^{1/\beta_X}, \tag{2.14}$$

[12, 18]. The variability of random variable X, e.g. the maximum bearable axial load or lateral deflection, is measured by the interpercentile range

$$R_X = Q_{95} - Q_5, \tag{2.15}$$

which is the difference of the 95th and 5th percentiles Q_{95} and Q_5. It, thus, is a measure for the parameter space which contains 90% of all observations, figure 2.5b).

2.3.3 Uncertainty in passive buckling and active buckling control

Uncertainty in the passive buckling of slender beam-columns subject to (quasi-)static axial loads, as discussed in section 2.1.1, has been investigated numerically and experimentally, e.g. in [31, 48]. A review on the history of uncertainty in numerical simulation of buckling until the year 2000 is presented in [24]. As was shown in figure 2.3, uncertainty in the form of imperfections increases the lateral deflections due to a compressive axial load and reduces the maximum bearable axial load $F_{x,\max,\mathrm{p}}$ of a passive beam-column. Uncertainty in the material, geometry, loading or the support properties is seen as a variability in the maximum bearable axial load.

The goal of the active buckling control is to compensate the uncertainty and, thus, increase the maximum bearable axial loads. However, the influence of uncertainty on the active buckling control as compared to the passive buckling has not been addressed and quantified in literature, except in [26, 27].

ENSS performed an experimental quantification of probabilistic uncertainty in the passive and active maximum bearable axial loads due to repeated buckling experiments by the two-parameter WEIBULL distribution according to (2.13) and showed a reduction in the variability in the maximum bearable axial loads for the active case $F_{x,\max,\mathrm{a}}$ compared to the passive case $F_{x,\max,\mathrm{p}}$. However, highly skewed WEIBULL pdf curves with large shape parameters of $\beta_X > 300$ were obtained for the actively controlled beam-column due to the late onset of buckling. Therefore and in this thesis, the three-parameter WEIBULL distribution is used to quantify probabilistic uncertainty in the beam-column deflections and maximum bearable

axial loads. Furthermore, assembly and mounting of the beam-column system as well as component variations by using different beam-columns and supports are expected to have significant contributions to the uncertainty in the beam-column deflections and maximum bearable axial loads. However, these influences have not been investigated so far, but are included in this work.

2.4 Conclusion

Static buckling is a stability failure with large lateral deflections of ideal, compressively loaded beam-columns at the critical buckling load $F_{x,\mathrm{cr}}$. The critical buckling load depends on the beam-column's support stiffness and is maximum for fixed-fixed supports. However, real beam-columns have imperfections that lead to an initial lateral deflection, which is amplified by axial loads approaching the critical buckling load. Therefore, real beam-columns already fail at a passive maximum bearable axial load $F_{x,\mathrm{max,p}} < F_{x,\mathrm{cr}}$.

The lateral beam-column dynamic behavior significantly depends on the axial load. Different types of dynamic buckling may occur depending on the dynamic axial load $F_x(t)$, e.g. harmonic, impulse or step excitation. In this thesis, axial step loads $F_x(t) \neq \text{const.}$ are considered for the investigation of passive buckling and active buckling control.

Besides passive approaches to increase the passive maximum bearable axial load $F_{x,\mathrm{max,p}}$ of a beam-column by changing the material, geometry or supports, active buckling control may reduce the lateral beam-column deflections and, thus, increase the active maximum bearable axial load $F_{x,\mathrm{max,a}} > F_{x,\mathrm{max,p}}$. Previous studies have investigated active buckling control for academic beam-column systems with

- rectangular cross-sections and mostly pinned-pinned supports,
- relatively high slenderness ratios $350 \leq \lambda \leq 4420$,
- relatively low critical buckling loads $5\,\mathrm{N} \leq F_{x,\mathrm{cr}} \leq 143\,\mathrm{N}$ and
- (quasi-)static axial loads $F_x(t) \approx \text{const.}$

Active buckling control was most often implemented by

- piezoelectric patch actuators applied to the beam-column surface,
- either constant or manually switched feedback or optimal controllers and
- most often without systematic investigation of data uncertainty.

As motivated in section 1.2, the novel contributions of this thesis are the investigation of a practical beam-column with

- circular cross-section with nearly fixed-fixed supports to optimally utilize the passive beam-column,
- relatively low slenderness ratios $\lambda = 102$ closer to the transition slenderness ratio, as in practical beam-columns,
- relatively high critical buckling load $F_{x,\mathrm{cr}} = 3381\,\mathrm{N}$ and
- dynamic axial loads $F_x(t) \neq \text{const.}$

as well as the active buckling control by

- piezoelectric stack actuators integrated in piezo-elastic supports to stabilize the beam-column in arbitrary lateral directions,
- an LPV controller to account for the beam-column's highly axial load-dependent lateral dynamic behavior and
- the experimental quantification of probabilistic uncertainty in the maximum bearable axial loads and lateral deflections due to system assembly, mounting and variation of components by three-parameter WEIBULL distributions.

3 Active buckling control of a beam-column system

This chapter introduces the beam-column system used for the investigations of active buckling control in this thesis. First, the general concept for active buckling control of a beam-column with circular cross-section by piezo-elastic supports is presented in section 3.1. Then, the mathematical model of the beam-column system including the mechanical and electrical components is derived in section 3.2. Finally, the controller used for active buckling control is presented in section 3.3.

3.1 Concept of the beam-column system

This section presents the concept of the beam-column system for active buckling control investigated in this thesis. The term beam-column system refers to the physical system consisting of

- the axially loaded beam-column with its supports, actuators and sensors and
- the electrical components for signal processing.

The beam-column (index b) used for active buckling control is a slender beam-column with length l_b and circular solid cross-section with constant radius r_b, as shown in figure 3.1. The Young's modulus E_b and density ϱ_b are assumed to be constant across the entire beam-column length. The lower beam-column end is fixed at support A (index A). The upper beam-column end at support B (index B), where the time-varying axial load $F_x(t)$ is applied, is free to move in longitudinal x-direction. The beam-column may buckle in any plane lateral to the x-axis by flexural buckling without preferred lateral direction. Due to the circular solid cross-section, lateral torsional buckling does not occur, [95].

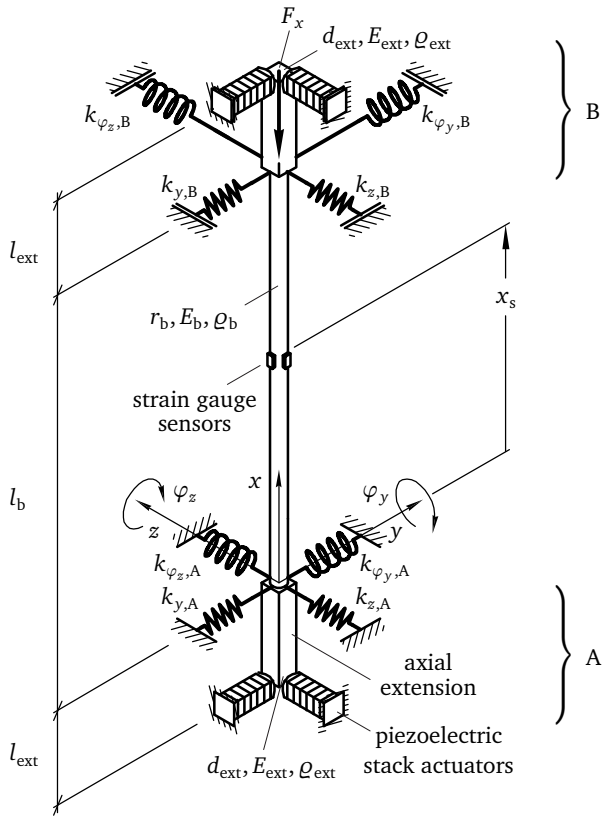

Figure 3.1.: Schematic sketch of the axially loaded beam-column with elastic supports, piezoelectric stack actuators and strain gauge sensors

A passive beam-column with given material and geometry has the maximum possible critical buckling load $F_{x,cr}$ for EULER buckling case IV (fixed-fixed) in (2.5), figure 2.2. To optimally use the passive load capacity of the beam-column for active buckling control, the beam-column ends at $x = 0$ and $x = l_b$ are supported by lateral and rotational stiffness in and around the y- and z-direction that create close to fixed-fixed boundary conditions, as shown in section 5.1. In the schematic sketch in figure 3.1, the elastic boundary conditions are represented by lateral stiffness $k_{y/z,A/B}$ and rotational stiffness $k_{\varphi_{y/z},A/B}$.

Furthermore, piezoelectric stack actuators are integrated in the lateral load path via axial extensions (index ext) with length l_{ext}, which are connected to the beam-column ends and are mechanically prestressed (not shown in figure 3.1), section 4.1.2. By that, the mechanical stiffness of the piezoelectric stack actuators further increases the overall stiffness of the supports. The axial extensions have quadratic cross-sections with edge length d_{ext} and relatively high bending stiffness with Young's modulus E_{ext} and density ϱ_{ext}.

The inverse piezoelectric effect is used to deform the piezoelectric stack actuators by electrical voltages applied to the electrodes, [66, 72]. Thus, the electrically prestressed piezoelectric stack actuators exert active lateral forces in positive and negative y- and z-direction to the beam-column's axial extensions. They result in active bending moments, which act in arbitrary directions at the lower and upper beam-column ends. Because of the elastically supported beam-column and the integrated piezoelectric stack actuators, the supports are called piezo-elastic supports A at location $x = 0$ and B at $x = l_{\mathrm{b}}$. The novel concept of the piezo-elastic support was patented in [28] and, other than for active buckling control, is also used for vibration attenuation with shunted piezoelectric transducers, [35, 36].

Strain gauge sensors (index s) at the sensor position $x_{\mathrm{s}} = l_{\mathrm{b}}/2$ are used to measure the surface strains due to bending to calculate the deflection of the beam-column in y- and z-direction. In contrast to the piezoelectric patch actuators, which are used in most studies on active buckling control, section 2.2, the strain gauges can be applied to the curved surface of the beam-column with circular cross-section and the modification of the beam-column's flexural stiffness is relatively small.

The axially loaded beam-column with elastic supports, piezoelectric stack actuators and strain gauge sensors is represented by the beam-column model, which is presented in sections 3.2.1 and 3.2.2. For the active buckling control, electrical components for signal processing are added to the in- and outputs of the beam-column model, as shown in figure 3.2, section 3.2.4. The controller output $\boldsymbol{u}(t)$ is amplified to generate the piezoelectric stack actuator voltages (index pz) $V_{\mathrm{pz},y/z}(t)$ and the strain gauge sensor signals $\varepsilon_{\mathrm{s},y/z}(t)$ are low-pass filtered to generate controller input $\boldsymbol{y}(t)$ representing the beam-column plant. The axial load-dependent LPV controller $\boldsymbol{R}(F_x)$ (3.57) connects the controller in- and output for active buckling control, section 3.3.

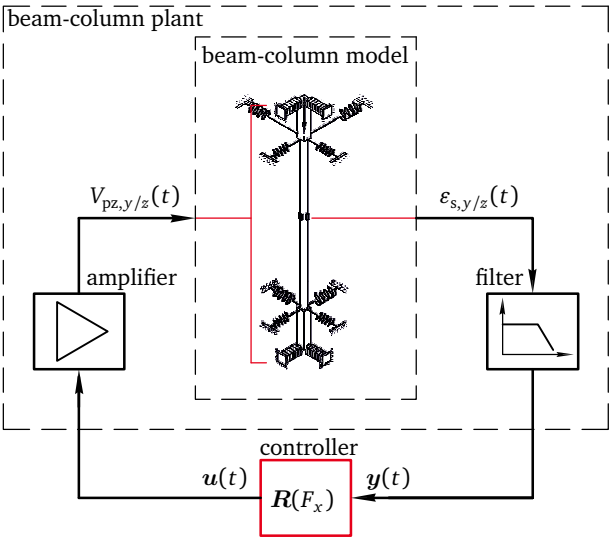

Figure 3.2.: Concept of the beam-column system for active buckling control

The experimental realizations of the beam-column system and the piezo-elastic supports are presented in sections 4.1.1 and 4.1.2, respectively. The electrical components for signal processing in the experiment are presented in section 4.2.

3.2 Mathematical model of the beam-column system

This section presents the mathematical model of the beam-column system without controller, referred to as beam-column plant, figure 3.2. The model is derived analytically and is later used to design a controller, section 3.3. The performance of the controller is primarily determined by the quality of the underlying mathematical model used for controller synthesis. In particular, the model is required to

1. properly describe the elastic boundary conditions created by the piezo-elastic supports and include the actuator inputs and sensor outputs,
2. capture the axial load-dependency of the lateral beam-column dynamic behavior, which is critical for buckling,
3. allow the model-based controller synthesis with minimal model order and

4. include the signal processing dynamics to account for phase delay introduced by the electrical components.

The requirements 1–4 are mirrored by the outline of the section. First, section 3.2.1 introduces the finite element (FE) model of the beam-column with piezo-elastic supports, actuators and sensors, in the following called FE beam-column model (requirement 1). The FE beam-column model is an LPV model, where the axial load F_x is included as varying parameter, to describe the lateral dynamic behavior (requirement 2). Second, sections 3.2.2 and 3.2.3 present the modal reduction of the FE beam-column model to reduce the order and complexity for controller synthesis and the beam-column transfer function (requirement 3). Finally, section 3.2.4 derives the beam-column plant by adding the dynamics of the electrical components for signal conditioning, such as analog filters and amplifiers, to the lateral dynamics of the mechanical beam-column model (requirement 4).

3.2.1 Finite Element beam-column model

For the FE model, the beam-column and the stiff axial extensions are discretized by $N-1$ one-dimensional EULER-BERNOULLI beam-column elements with N nodes, figure 3.3. The beam-column is discretized with $N-3$ equidistant finite elements and the axial extensions are discretized by one single finite element. Consequently, the axial load $F_x(t)$ acts at the second to last node $N-1$.

The piezoelectric stack actuators in the piezo-elastic supports A and B are represented by piezoelectric stack actuator forces $F_{\mathrm{pz},y/z,\mathrm{A/B}}(t)$ with active and elastic components in y- and z-direction of node 1 and node N of the FE model. The strain gauge sensors at node n_s are represented by discrete sensor mass m_s and stiffness k_s, which are relatively small, compared to the beam-column's mass and flexural stiffness, but necessary to properly describe the lateral dynamic behavior of the beam-column system, section 5.2.

For the controller synthesis in section 3.3, disturbance end moments $M_{\mathrm{d},y/z}(t)$ acting in opposite directions at supports A and B, as in figure 2.1, are included in the FE beam-column model. They represent imperfections, such as initial curvature, eccentric loading or end moments of a real beam-column system, section 2.1.1.

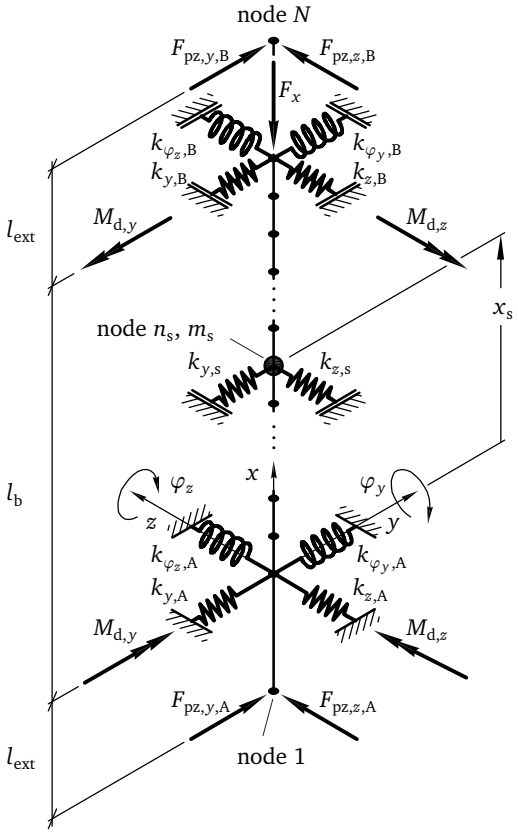

Figure 3.3.: Sketch of the FE beam-column

The following assumptions are made for the FE modeling:

- EULER-BERNOULLI beam theory is valid for the beam-column with axial extensions, i.e. small deflections, no shear and cross-sections remain perpendicular to the bending axis,
- the lateral dynamic behavior of the beam-column is independent in y- and z-direction,
- translational and rotational displacements in and around the beam-column's x-axis are neglegted,

- the rotational inertia of the finite beam-column elements is neglected,
- the axial load F_x acts along the x-axis of the beam-column, does not change direction and is constant across the entire beam-column and
- the inertia of the beam-column support stiffness and the piezoelectric transducers is neglected.

To derive the mathematical model of the beam-column system, the rest of this section is divided into two parts. First, the FE model of the undamped elastically supported beam-column including the elastic components of the piezoelectric stack actuator forces, but without external loads is presented. External loads refer to the active components of the piezoelectric stack actuator forces $F_{\mathrm{pz},y/z,\mathrm{A/B}}(t)$, derived in (3.16), and the disturbance end moments $M_{\mathrm{d},y/z}(t)$. Then, damping and external loads are added to the FE model and the FE output equation is derived.

Undamped beam-column without external loads

Starting point for the mathematical modeling of the beam-column with elastic supports, piezoelectric stack actuators and strain gauge sensors subject to axial load $F_x(t)$, as shown in figure 3.3, is the linear, homogeneous EULER-BERNOULLI differential equation of motion for lateral beam-column deflections $v(x,t)$ in y-direction, as introduced in (2.8), and $w(x,t)$ in z-direction

$$\begin{aligned} \varrho A\,\ddot{v}(x,t) + EI\,v^{IV}(x,t) + F_x(t)\,v''(x,t) &= 0 \\ \varrho A\,\ddot{w}(x,t) + EI\,w^{IV}(x,t) + F_x(t)\,w''(x,t) &= 0 \end{aligned} \tag{3.1}$$

[13, 91]. To describe the lateral dynamic behavior, the inertia and stiffness properties of the beam-column system are derived by the FE method. First, the beam-column with axial extensions is divided into finite elements, as shown in figure 3.3, to derive mass and stiffness element matrices that describe the distributed mass and stiffness properties of the individual finite elements. Second, the boundary conditions of the elastic beam-column supports, piezoelectric stack actuators and strain gauge sensors are presented. Finally, the FE mass and stiffness matrices are assembled and important properties of the beam-column model, such as the critical buckling load, eigenfrequencies and eigenvectors are presented.

Finite elements and element matrices

Figure 3.4a) shows the n-th finite beam-column element (index el) between nodes n and $n+1$ ($1 \leq n \leq N-1$) with length l_{el}, Youngs modulus E_{el}, second moment of area I_{el}, density ϱ_{el} and cross-section area A_{el}. The finite elements for the beam-column and the axial extensions are characterized by their Youngs moduli E_{b} and E_{ext}, second moments of area $I_{\mathrm{b}} = \pi/4\, r_{\mathrm{b}}^4$ and $I_{\mathrm{ext}} = d_{\mathrm{ext}}^4/12$, densities ϱ_{b} and ϱ_{ext} as well as cross-section areas $A_{\mathrm{b}} = \pi\, r_{\mathrm{b}}^2$ and $A_{\mathrm{ext}} = d_{\mathrm{ext}}^2$.

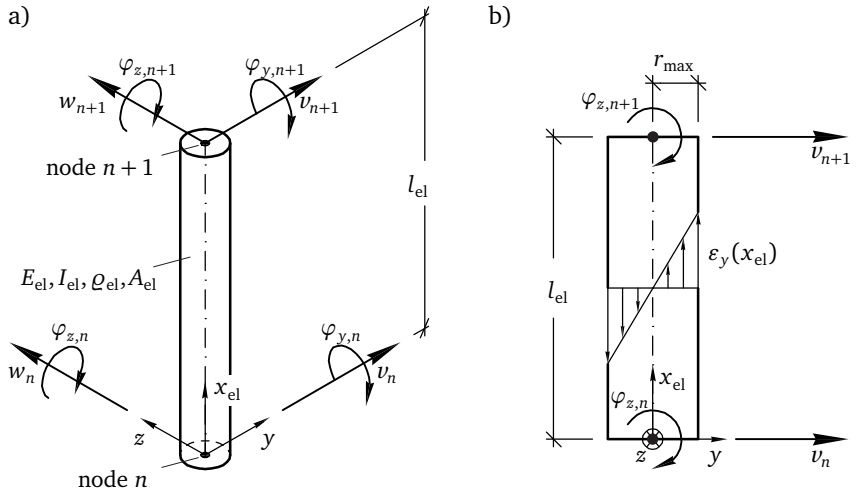

Figure 3.4.: n-th finite beam-column element of length l_{el} with a) element coordinates in positive directions, b) bending strains in the x-y-plane with maximum surface strain $\varepsilon_y(x_{\mathrm{el}})$

Each node n is described by the lateral displacements v_n and w_n in y- and z-direction and the rotational displacements $\varphi_{y,n}$ and $\varphi_{z,n}$ around the y- and z-axis. The nodal displacements and rotations of the n-th finite element are summarized in the $[8 \times 1]$ element displacement vector

$$\boldsymbol{r}_{\mathrm{el}}(t) = \left[v_n(t),\, w_n(t),\, \varphi_{y,n}(t),\, \varphi_{z,n}(t),\, v_{n+1}(t),\, w_{n+1}(t),\, \varphi_{y,n+1}(t),\, \varphi_{z,n+1}(t) \right]^T . \quad (3.2)$$

The lateral displacements within the n-th finite element are calculated by

$$\begin{bmatrix} v_{\mathrm{el}}(x_{\mathrm{el}}, t) \\ w_{\mathrm{el}}(x_{\mathrm{el}}, t) \end{bmatrix} = \boldsymbol{H}(x_{\mathrm{el}})\, \boldsymbol{r}_{\mathrm{el}}(t) \quad (3.3)$$

as functions of the local coordinate x_{el} and time t. They depend on the eight HERMITIAN cubic shape functions given by

$$\begin{aligned} H_1(x) = \;\; H_2(x) &= 1-3\left(\frac{x}{l}\right)^2+2\left(\frac{x}{l}\right)^3, \\ H_3(x) = -H_4(x) &= \left[-\frac{x}{l}+2\left(\frac{x}{l}\right)^2-\left(\frac{x}{l}\right)^3\right] l, \\ H_5(x) = \;\; H_6(x) &= 3\left(\frac{x}{l}\right)^2-2\left(\frac{x}{l}\right)^3 \text{ and} \\ H_7(x) = -H_8(x) &= \left[\left(\frac{x}{l}\right)^2-\left(\frac{x}{l}\right)^3\right] l, \end{aligned} \tag{3.4}$$

[47, 99], where the index el in the element length l_{el} and element x-coordinate x_{el} is omitted here and in the following for the purpose of clarity ($l = l_{\mathrm{el}}$, $x = x_{\mathrm{el}}$). The shape functions are summarized in the shape function matrix

$$\boldsymbol{H}(x) = \begin{bmatrix} H_1(x) & 0 & 0 & H_4(x) & H_5(x) & 0 & 0 & H_8(x) \\ 0 & H_2(x) & H_3(x) & 0 & 0 & H_6(x) & H_7(x) & 0 \end{bmatrix}. \tag{3.5}$$

Similarly to (3.3), the time and space derivatives of the lateral displacement are

$$\begin{aligned} \begin{bmatrix} \dot{v}_{\mathrm{el}}(x,t) \\ \dot{w}_{\mathrm{el}}(x,t) \end{bmatrix} &= \boldsymbol{H}(x)\;\dot{\boldsymbol{r}}_{\mathrm{el}}(t) \qquad & \begin{bmatrix} \ddot{v}_{\mathrm{el}}(x,t) \\ \ddot{w}_{\mathrm{el}}(x,t) \end{bmatrix} &= \boldsymbol{H}(x)\;\ddot{\boldsymbol{r}}_{\mathrm{el}}(t) \\ \begin{bmatrix} v'_{\mathrm{el}}(x,t) \\ w'_{\mathrm{el}}(x,t) \end{bmatrix} &= \boldsymbol{H}'(x)\,\boldsymbol{r}_{\mathrm{el}}(t) \qquad & \begin{bmatrix} v''_{\mathrm{el}}(x,t) \\ w''_{\mathrm{el}}(x,t) \end{bmatrix} &= \boldsymbol{H}''(x)\,\boldsymbol{r}_{\mathrm{el}}(t). \end{aligned} \tag{3.6}$$

Figure 3.4b) shows the beam-column strains within the n-th finite element in the x-y-plane. The bending strains are highest at the beam-column surface with maximum distance from the element x_{el}-axis $r_{\max}$. The surface strains in y- and z-direction at the strain gauge position, which are needed for the active buckling control, are calculated from the element displacement vector (3.2) by

$$\begin{bmatrix} \varepsilon_{y,\mathrm{el}}(x,t) \\ \varepsilon_{z,\mathrm{el}}(x,t) \end{bmatrix} = -r_{\max}\,\boldsymbol{H}''(x)\,\boldsymbol{r}_{\mathrm{el}}(t) \tag{3.7}$$

using the second derivative of the shape function matrix in (3.5) at the strain gauge positions, [47]. For the beam-column between nodes 2 and $N-1$, the maximum distance is the beam-column radius $r_{\max} = r_{\mathrm{b}}$.

The discretized linear, homogeneous EULER-BERNOULLI differential equation of motion (3.1) describes the lateral dynamics of a single finite element without any boundary conditions via the element mass and stiffness matrices, which are derived in the following. For that, the method of weighted residuals, also known as GALERKIN method is used, [47, 73, 99].

Equation (3.1) is written in the weak formulation, multiplied by the shape functions (3.4) and integrated along a finite element. After partial integration and use of the approximated displacements (3.3), the components of the mass and stiffness matrices are calculated in dependence of the shape functions (3.4) and their first and second spacial derivatives, [47, 99]. Consequently, the components of the element mass matrix $\boldsymbol{M}_{\mathrm{el}}$ are given by

$$m_{\mathrm{el},ij} = \int_0^l \varrho A\, H_i(x) H_j(x)\, \mathrm{d}x \qquad i,j = 1,\cdots,8, \tag{3.8}$$

resulting in the $[8 \times 8]$ element mass matrix

$$\boldsymbol{M}_{\mathrm{el}} = \frac{\varrho A l}{420} \begin{bmatrix} 156 & 0 & 0 & 22l & 54 & 0 & 0 & -13l \\ & 156 & -22l & 0 & 0 & 54 & 13l & 0 \\ & & 4l^2 & 0 & 0 & -13l & -3l^2 & 0 \\ & & & 4l^2 & 13l & 0 & 0 & -3l^2 \\ & & & & 156 & 0 & 0 & -22l \\ & & & & & 156 & 22l & 0 \\ & & \text{symmetric} & & & & 4l^2 & 0 \\ & & & & & & & 4l^2 \end{bmatrix}. \tag{3.9}$$

Analog, the components of the elastic (index e) element stiffness matrix $\boldsymbol{K}_{\mathrm{e,el}}$ are given by

$$k_{\mathrm{e,el},ij} = \int_0^l EI\, H_i''(x) H_j''(x)\, \mathrm{d}x \qquad i,j = 1,\cdots,8, \tag{3.10}$$

resulting in the $[8 \times 8]$ elastic element stiffness matrix

$$\boldsymbol{K}_{\mathrm{e,el}} = \frac{E\,I}{l^3} \begin{bmatrix} 12 & 0 & 0 & 6l & -12 & 0 & 0 & 6l \\ & 12 & -6l & 0 & 0 & -12 & -6l & 0 \\ & & 4l^2 & 0 & 0 & 6l & 2l^2 & 0 \\ & & & 4l^2 & -6l & 0 & 0 & 2l^2 \\ & & & & 12 & 0 & 0 & -6l \\ & & & & & 12 & 6l & 0 \\ & & \text{symmetric} & & & & 4l^2 & 0 \\ & & & & & & & 4l^2 \end{bmatrix}. \tag{3.11}$$

The components of the geometric (index g) element stiffness matrix $\boldsymbol{K}_{\mathrm{g,el}}$, which describes the linear influence of the axial load F_x on the beam-column's lateral stiffness, are

$$k_{\mathrm{g,el},ji} = \int_0^l H_i'(x) H_j'(x)\,\mathrm{d}x \qquad i,j = 1,\cdots,8, \tag{3.12}$$

resulting in the $[8 \times 8]$ geometric element stiffness matrix

$$\boldsymbol{K}_{\mathrm{g,el}} = \frac{1}{10l} \begin{bmatrix} 12 & 0 & 0 & l & -12 & 0 & 0 & l \\ & 12 & -l & 0 & 0 & -12 & -l & 0 \\ & & 4/3\,l^2 & 0 & 0 & l & -l^2/3 & 0 \\ & & & 4/3\,l^2 & -l & 0 & 0 & -l^2/3 \\ & & & & 12 & 0 & 0 & -l \\ & & & & & 12 & l & 0 \\ & & \text{symmetric} & & & & 4/3\,l^2 & 0 \\ & & & & & & & 4/3\,l^2 \end{bmatrix}. \tag{3.13}$$

Boundary conditions

The boundary conditions of the beam-column with axial extensions are given by

- the elastic beam-column supports,
- the piezoelectric stack actuators and
- the strain gauge sensors.

The **elastic beam-column supports** define the boundary conditions at the beam-column ends at $x = 0$ and $x = l_\mathrm{b}$ in y- and z-direction, as shown in figure 3.3. The lateral and rotational stiffness are modeled to be linearly dependent from axial load F_x as

$$\begin{aligned} k_{y,\mathrm{A/B}}(F_x) &= k_{y,\mathrm{A/B,e}} + F_x\, k_{y,\mathrm{A/B,g}}, \\ k_{z,\mathrm{A/B}}(F_x) &= k_{z,\mathrm{A/B,e}} + F_x\, k_{z,\mathrm{A/B,g}}, \\ k_{\varphi_y,\mathrm{A/B}}(F_x) &= k_{\varphi_y,\mathrm{A/B,e}} + F_x\, k_{\varphi_y,\mathrm{A/B,g}}, \\ k_{\varphi_z,\mathrm{A/B}}(F_x) &= k_{\varphi_z,\mathrm{A/B,e}} + F_x\, k_{\varphi_z,\mathrm{A/B,g}}, \end{aligned} \tag{3.14}$$

taking into account the experimentally observed axial load-dependency, section 5.2. The stiffness terms in (3.14) are included in the $[4\times4]$ elastic and geometric support stiffness matrices

$$\boldsymbol{K}_{\mathrm{A/B,e/g}} = \begin{bmatrix} k_{y,\mathrm{A/B,e/g}} & 0 & 0 & 0 \\ 0 & k_{z,\mathrm{A/B,e/g}} & 0 & 0 \\ 0 & 0 & k_{\varphi_y,\mathrm{A/B,e/g}} & 0 \\ 0 & 0 & 0 & k_{\varphi_z,\mathrm{A/B},e/g} \end{bmatrix} \tag{3.15}$$

for the supports A and B.

In general, **piezoelectric stack actuators** that use the inverse piezoelectric effect can be modeled as linear-elastic actuators with elastic and active components, [66, 72]. Thus, the piezoelectric stack actuators contribute to the overall stiffness of the piezo-elastic supports by their inherent mechanical stiffness that is included in the elastic FE stiffness matrix. Consequently, the piezoelectric stack actuators in piezo-elastic supports A and B in y- and z-direction are modeled by discrete forces

$$\begin{aligned} F_{\mathrm{pz},y,\mathrm{A}} &= \theta_{y,\mathrm{A}}\, k_{\mathrm{pz},y,\mathrm{A}}\, V_{\mathrm{pz},y} - k_{\mathrm{pz},y,\mathrm{A}}\, v_1, \\ F_{\mathrm{pz},z,\mathrm{A}} &= \theta_{z,\mathrm{A}}\, k_{\mathrm{pz},z,\mathrm{A}}\, V_{\mathrm{pz},z} - k_{\mathrm{pz},z,\mathrm{A}}\, w_1, \\ F_{\mathrm{pz},y,\mathrm{B}} &= \theta_{y,\mathrm{B}}\, k_{\mathrm{pz},y,\mathrm{B}}\, V_{\mathrm{pz},y} - k_{\mathrm{pz},y,\mathrm{B}}\, v_N, \\ F_{\mathrm{pz},z,\mathrm{B}} &= \theta_{z,\mathrm{B}}\, k_{\mathrm{pz},z,\mathrm{B}}\, V_{\mathrm{pz},z} - k_{\mathrm{pz},z,\mathrm{B}}\, w_N, \end{aligned} \tag{3.16}$$

acting at node 1 at $x = -l_\mathrm{ext}$ and the last node N at $x = l_\mathrm{b} + l_\mathrm{ext}$ of the FE model, figure 3.3. In (3.16), $\theta = N_\mathrm{pz}\, d_{33}$ is the piezoelectric force constant for a piezoelectric stack actuator with N_pz layers and the piezoelectric constant d_{33}, and k_pz is the mechanical stiffness of the short-circuited piezoelectric stack actuators, [72].

The actuator voltages $V_{\mathrm{pz},y}(t)$ and $V_{\mathrm{pz},z}(t)$ are simultaneously applied to both piezoelectric stack actuators in supports A and B in y- and z-direction. The mechanical stiffness of the piezoelectric stack actuators is included in the $[4 \times 4]$ piezo stiffness matrix

$$\boldsymbol{K}_{\mathrm{pz,A/B}} = \begin{bmatrix} k_{\mathrm{pz},y,\mathrm{A/B}} & 0 & 0 & 0 \\ 0 & k_{\mathrm{pz},z,\mathrm{A/B}} & 0 & 0 \\ 0 & 0 & 0 & 0 \\ 0 & 0 & 0 & 0 \end{bmatrix}. \tag{3.17}$$

to account for the elastic components of (3.16). The active components of (3.16) are included in the beam-column model as external forces acting on the axial extensions according to (3.25) and (3.26).

The **strain gauge sensors** in the beam-column center, figure 3.3, are represented by the discrete sensor stiffness k_{s} and the sensor mass m_{s}, that are mainly attributed to the sensor cables, section 4.1.1, and are needed to calibrate the mathematical model of the beam-column system, section 5.2. They are included in the $[4 \times 4]$ sensor stiffness and mass matrices

$$\boldsymbol{K}_{\mathrm{s}} = \begin{bmatrix} k_{\mathrm{s},y} & 0 & 0 & 0 \\ 0 & k_{\mathrm{s},z} & 0 & 0 \\ 0 & 0 & 0 & 0 \\ 0 & 0 & 0 & 0 \end{bmatrix} \quad \text{and} \quad \boldsymbol{M}_{\mathrm{s}} = \begin{bmatrix} m_{\mathrm{s}} & 0 & 0 & 0 \\ 0 & m_{\mathrm{s}} & 0 & 0 \\ 0 & 0 & 0 & 0 \\ 0 & 0 & 0 & 0 \end{bmatrix}. \tag{3.18}$$

Assembly of FE mass and stiffness matrices

The $[8 \times 8]$ element mass and stiffness matrices $\boldsymbol{M}_{\mathrm{el}}$ (3.9), $\boldsymbol{K}_{\mathrm{e,el}}$ (3.11) and $\boldsymbol{K}_{\mathrm{g,el}}$ (3.13) are assembled to $[4N \times 4N]$ matrices according to the assembly scheme in figure 3.5. The $[4 \times 4]$ mass and stiffness matrices for the boundary conditions are added to the assembled matrices at the respective lateral and rotational degrees of freedom according to figure 3.3 to obtain the FE mass matrix $\boldsymbol{M}$, elastic stiffness matrix $\boldsymbol{K}_{\mathrm{e}}$ and geometric stiffness matrix $\boldsymbol{K}_{\mathrm{g}}$.

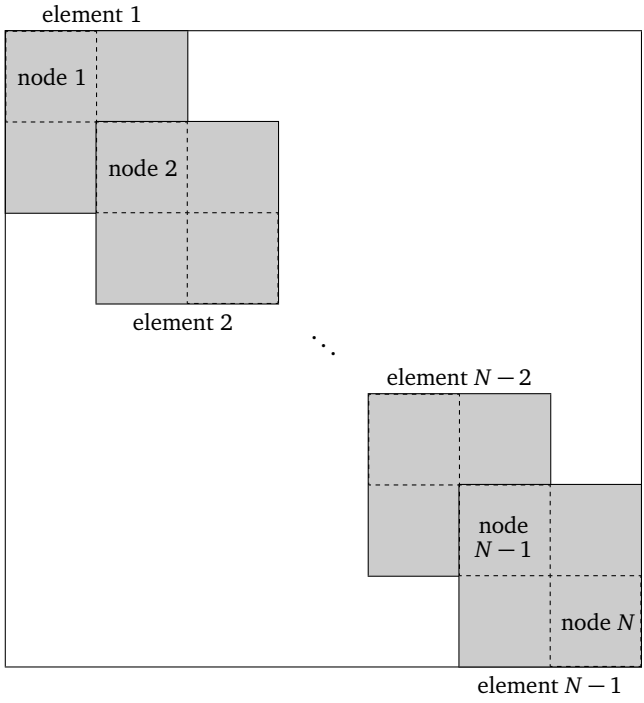

Figure 3.5.: Assembly scheme for the $[4N \times 4N]$ FE mass and stiffness matrices

- The sensor mass matrix $\boldsymbol{M}_{\mathrm{s}}$ (3.18) is part of the entries of the central node n_{s} of the FE mass matrix $\boldsymbol{M}$.

- The elastic and geometric support stiffness matrices $\boldsymbol{K}_{\mathrm{A/B,e/g}}$ in (3.15) for supports A and B are part of the entries of node 2 at $x = 0$ and node $N-1$ at $x = l_{\mathrm{b}}$ of the elastic and geometric stiffness matrices $\boldsymbol{K}_{\mathrm{e}}$ and $\boldsymbol{K}_{\mathrm{g}}$.

- The piezo stiffness matrices $\boldsymbol{K}_{\mathrm{pz,A/B}}$ (3.17) for supports A and B are part of the entries of node 1 at $x = -l_{\mathrm{ext}}$ and the last node N at $x = l_{\mathrm{b}} + l_{\mathrm{ext}}$ of the elastic system stiffness matrix $\boldsymbol{K}_{\mathrm{e}}$.

- Finally, the sensor stiffness matrix $\boldsymbol{K}_{\mathrm{s}}$ in (3.18) is part of the entries of the central FE node n_{s} at $x = x_{\mathrm{s}}$ of the elastic system stiffness matrix $\boldsymbol{K}_{\mathrm{e}}$.

After assembly of the FE mass and stiffness matrices from the element matrices, the undamped homogeneous FE equation of motion is

$$\boldsymbol{M}\ddot{\boldsymbol{r}}(t) + \left(\boldsymbol{K}_{\mathrm{e}} - F_x(t)\,\boldsymbol{K}_{\mathrm{g}}\right)\boldsymbol{r}(t) = \boldsymbol{0} \tag{3.19}$$

with the $[4N \times 1]$ FE displacement vector

$$\boldsymbol{r}(t) = \left[\, v_1(t),\ w_1(t),\ \varphi_{y,1}(t),\ \varphi_{z,1}(t), \ldots, v_N(t),\ w_N(t),\ \varphi_{y,N}(t),\ \varphi_{z,N}(t) \right]^T. \tag{3.20}$$

The overall stiffness has two components, the elastic stiffness matrix $\boldsymbol{K}_{\mathrm{e}}$ and the geometric stiffness matrix $\boldsymbol{K}_{\mathrm{g}}$, which describes the linear influence of the axial load F_x on the beam-column's lateral stiffness. The undamped, homogeneous FE equation of motion (3.19) represents the free lateral beam-column dynamics. It is used to calculate the critical buckling load, eigenfrequencies and eigenvectors of the beam-column with piezo-elastic supports, which are essential properties to describe the static and dynamic buckling behavior, as introduced in section 2.1.

For simple boundary conditions, the critical buckling load $F_{x,\mathrm{cr}}$ is given by (2.2). For the boundary conditions created by the elastic beam-column supports, the piezoelectric stack actuators and the strain gauge sensors, $F_{x,\mathrm{cr}}$ is calculated from the FE elastic and geometric stiffness matrices $\boldsymbol{K}_{\mathrm{e}}$ and $\boldsymbol{K}_{\mathrm{g}}$ by solving for the smallest solution of the eigenvalue problem

$$\det\left[\boldsymbol{K}_{\mathrm{e}} - F_x\,\boldsymbol{K}_{\mathrm{g}}\right] = 0, \tag{3.21}$$

[73]. By that, the critical buckling load can be determined for the boundary conditions of the beam-column with elastic supports, piezoelectric stack actuators and strain gauge sensors in figure 3.3, section 5.2.3.

The axial load-dependent angular eigenfrequencies $\omega(F_x) = 2\pi \cdot f(F_x)$, section 2.1.2, and eigenvectors $\widehat{\boldsymbol{r}}(F_x)$ are obtained by the solution of the modal eigenvalue problem

$$\left[\left(\boldsymbol{K}_{\mathrm{e}} - F_x\,\boldsymbol{K}_{\mathrm{g}}\right) - \omega^2 \boldsymbol{M}\right]\widehat{\boldsymbol{r}} = 0, \tag{3.22}$$

[72]. The angular eigenfrequencies are used to characterize the axial load-dependent lateral dynamic behavior and the stability of the beam-column system. The eigenvectors are used for modal decoupling of the FE beam-column model, section 3.2.2. Equation (3.22) has $4N$ solutions for the angular eigenfrequencies and eigenvectors.

Figure 3.6 shows the first three normalized eigenvectors $\widehat{r}_{1/2/3}(F_x)$ for the unloaded, $F_x = 0$, and critically loaded, $F_x = F_{x,\mathrm{cr}}$, beam-column with piezo-elastic supports.

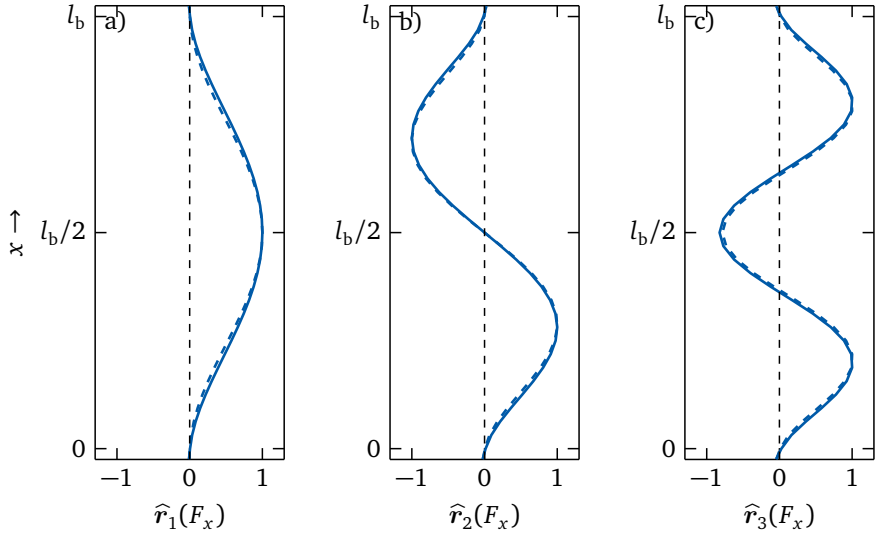

Figure 3.6.: First three normalized eigenvectors $\widehat{r}_{1/2/3}(F_x)$ for zero axial loads $F_x = 0$ (——) and theoretical critical buckling load $F_x = F_{x,\mathrm{cr}}$ (– –)

Due to the symmetric boundary conditions, the eigenvectors are symmetric and are similar for both depicted axial loads. All even modes exhibit a node at the beam-column center at $x = l_b/2$, figure 3.6b). Consequently, they are unobservable with the chosen sensor position $x_s = l_b/2$, which is used in the modal decoupling of the FE beam-column model, section 3.2.2.

Damped beam-column with external loads and output equation

In the second part of section 3.2.1, damping and external loads are added to the undamped, homogeneous FE equation of motion (3.19) to correctly represent the beam-column with piezo-elastic supports.

The extended FE equation of motion is given by

$$\boldsymbol{M}\ddot{\boldsymbol{r}}(t) + \boldsymbol{D}_\zeta\,\dot{\boldsymbol{r}}(t) + \big(\boldsymbol{K}_\mathrm{e} - F_x(t)\,\boldsymbol{K}_\mathrm{g}\big)\boldsymbol{r}(t) = \boldsymbol{B}_{\boldsymbol{u},0}\,\boldsymbol{u}_\mathrm{b}(t) + \boldsymbol{B}_{\boldsymbol{d},0}\,\boldsymbol{d}(t), \tag{3.23}$$

where $\boldsymbol{D}_\zeta$ is the FE damping matrix, $\boldsymbol{B}_{\boldsymbol{u},0}$ is the voltage input matrix and $\boldsymbol{B}_{\boldsymbol{d},0}$ is the disturbance input matrix.

Damping is assumed by RAYLEIGH proportional damping with the $[4N \times 4N]$ FE damping matrix $\boldsymbol{D}_\zeta = \alpha_0\,\boldsymbol{M} + \alpha_1\,\boldsymbol{K}_\mathrm{e}$. The mass and stiffness proportional damping coefficients α_0 and α_1 are obtained by the experimentally identified modal damping ratios ζ_1 and ζ_3, section 5.2, together with the undamped angular eigenfrequencies ω_1 and ω_3 for the unloaded beam-column from (3.22) for the first and third bending modes via

$$\begin{bmatrix}\alpha_0\\ \alpha_1\end{bmatrix} = 2\,\frac{\omega_1\omega_3}{\omega_3^2-\omega_1^2}\begin{bmatrix}\omega_3 & -\omega_1\\ -1/\omega_3 & 1/\omega_1\end{bmatrix}\begin{bmatrix}\zeta_1\\ \zeta_3\end{bmatrix}, \tag{3.24}$$

[20, 72]. The first and third mode are chosen, since only the odd modes are observable with the chosen sensor position $x_\mathrm{s} = l_\mathrm{b}/2$ in the beam-column center, figures 3.1 and 3.6.

The active components of the piezoelectric stack actuator forces in (3.16) and disturbance end moments acting on the beam-column with piezo-elastic supports, as shown in figure 3.3, are given on the right side of (3.23). The actuator voltages $V_{\mathrm{pz},y}(t)$ and $V_{\mathrm{pz},z}(t)$ are combined in the beam-column input vector

$$\boldsymbol{u}_\mathrm{b}(t) = \begin{bmatrix}V_{\mathrm{pz},y}(t)\\ V_{\mathrm{pz},z}(t)\end{bmatrix}. \tag{3.25}$$

The $[4N \times 2]$ voltage input matrix

$$\boldsymbol{B}_{\boldsymbol{u},0} = \begin{bmatrix}\theta_{y,\mathrm{A}}\,k_{\mathrm{pz},y,\mathrm{A}} & 0 & \boldsymbol{0}_{1\times 4N-6} & \theta_{y,\mathrm{B}}\,k_{\mathrm{pz},y,\mathrm{B}} & 0 & \boldsymbol{0}_{2\times 2}\\ 0 & \theta_{z,\mathrm{A}}\,k_{\mathrm{pz},z,\mathrm{A}} & \boldsymbol{0}_{1\times 4N-6} & 0 & \theta_{z,\mathrm{B}}\,k_{\mathrm{pz},z,\mathrm{B}} & \boldsymbol{0}_{2\times 2}\end{bmatrix}^T \tag{3.26}$$

allocates the active components of the piezoelectric stack actuator forces to the lateral degrees of freedom of the first node 1 at $x = -l_\mathrm{ext}$ and the last node N at $x = l_\mathrm{b} + l_\mathrm{ext}$ of the FE model. The term $\theta\,k_\mathrm{pz}$ describes the active forces generated by the piezoelectric stack actuators for an applied voltage $V_{\mathrm{pz},y/z}(t)$.

To account for imperfections, such as initial curvature, eccentric loading or end moments, [89] and section 2.1.1, disturbance end moments

$$\boldsymbol{d}(t) = \begin{bmatrix} M_{\mathrm{d},y}(t) \\ M_{\mathrm{d},z}(t) \end{bmatrix} \tag{3.27}$$

are applied at the beam-column ends at $x = 0$ and $x = l_\mathrm{b}$, figure 3.3.

The $[4N \times 2]$ disturbance input matrix

$$\boldsymbol{B}_{\boldsymbol{d},0} = \begin{bmatrix} \mathbf{0}_{1\times 6} & 0 & 1 & \mathbf{0}_{1\times 4N-14} & 0 & -1 & \mathbf{0}_{1\times 4} \\ \mathbf{0}_{1\times 6} & -1 & 0 & \mathbf{0}_{1\times 4N-14} & 1 & 0 & \mathbf{0}_{1\times 4} \end{bmatrix}^T \tag{3.28}$$

allocates the disturbance end moments to the rotational degrees of freedom of node 2 at $x = 0$ and node $N-1$ at $x = l_\mathrm{b}$ in y- and z-direction.

FE output equation

Finally, the FE output equation for the strain gauge sensors is derived. The sensors measure the surface strains in the beam-column center due to bending in y- and z-direction, figure 3.1. Consequently, the beam-column bending strains at sensor position $x_\mathrm{s} = l_\mathrm{b}/2$ in y- and z-direction are used as the beam-column output

$$\boldsymbol{y}_\mathrm{b}(t) = \begin{bmatrix} \varepsilon_{\mathrm{s},y}(t) \\ \varepsilon_{\mathrm{s},z}(t) \end{bmatrix} = \begin{bmatrix} \varepsilon_y(x_\mathrm{s}, t) \\ \varepsilon_z(x_\mathrm{s}, t) \end{bmatrix}. \tag{3.29}$$

It is calculated from the FE displacement vector $\boldsymbol{r}(t)$ (3.20) by the output equation

$$\boldsymbol{y}_\mathrm{b}(t) = \boldsymbol{C}_{\boldsymbol{y},0}\, \boldsymbol{r}(t), \tag{3.30}$$

with the $[2 \times 4N]$ output matrix $\boldsymbol{C}_{\boldsymbol{y},0}$, which, in accordance with (3.7), is given by

$$\boldsymbol{C}_{\boldsymbol{y},0} = \begin{bmatrix} \mathbf{0}_{2\times 2N-6} & -r_\mathrm{b}\, \boldsymbol{H}''(x_\mathrm{s}) & \mathbf{0}_{2\times 2N-2} \end{bmatrix}. \tag{3.31}$$

3.2.2 Reduced modal beam-column model

The FE equation of motion (3.23) and the FE output equation (3.30) represent the full FE model of the beam-column in figure 3.3. To properly capture the lateral dynamic behavior, the beam-column with axial extensions is discretized by $N-1 = 34$ finite elements with $N = 35$ nodes. Therefore, (3.23) describes the

axial load-dependent lateral beam-column dynamics with $4N = 140$ degrees of freedom. This relatively high order of the FE beam-column model is unsuitable for efficient computational processing, in particular for model-based controller synthesis, [7, 85]. In order to reduce computational effort, a modal model order reduction is performed, [34, 72].

The first lateral beam-column mode of vibration becomes instable for axial loads greater than the first critical buckling load from (3.21) and, thus, is essential for active buckling control. The sensor position $x_s = l_b/2$ and the symmetric actuator voltages $V_{pz,y/z}(t)$, which are the same in piezo-elastic supports A and B, in figure 3.3 are chosen so that the second and all higher even modes are unobservable and uncontrollable in order to separate the critical first mode of vibration. Therefore, the even modes of vibration, which are not observable by the given sensor position, are excluded from the reduced modal model.

To properly describe the lateral dynamic behavior of the beam-column system that was observed experimentally in section 5.2, the third mode of vibration is included in the reduced modal model, but all higher odd modes are neglected. Thus, the FE model is modally decoupled and reduced by truncation to only include the first and third lateral modes of vibration for both y- and z-direction. This reduces the modal beam-column model to four degrees of freedom. By that, the complexity of controller design is reduced and the resulting modal beam-column model is observable and controllable with the given sensor and actuator locations, [33].

The FE model is decoupled with the $[140 \times 4]$ truncated modal matrix $\boldsymbol{\Phi}$, which includes the four $[140 \times 1]$ eigenvectors $\widehat{\boldsymbol{r}}_{1/3,y/z}(F_{x,\mathrm{cr}})$ of the first and third lateral modes of vibration in y- and z- direction from (3.22), [72]. The linear approximation of the FE displacement vector (3.20) by the reduced $[4 \times 1]$ modal displacement vector $\boldsymbol{q}(\mathrm{t})$ is given by

$$\boldsymbol{r}(t) \approx \boldsymbol{\Phi}\,\boldsymbol{q}(t) = \begin{bmatrix} \widehat{\boldsymbol{r}}_{1,y}(F_{x,\mathrm{cr}}) \\ \widehat{\boldsymbol{r}}_{1,z}(F_{x,\mathrm{cr}}) \\ \widehat{\boldsymbol{r}}_{3,y}(F_{x,\mathrm{cr}}) \\ \widehat{\boldsymbol{r}}_{3,z}(F_{x,\mathrm{cr}}) \end{bmatrix}^T \begin{bmatrix} q_{1,y}(t) \\ q_{1,z}(t) \\ q_{3,y}(t) \\ q_{3,z}(t) \end{bmatrix}. \tag{3.32}$$

The eigenvectors to decouple the FE matrices are obtained for the critical buckling load $F_{x,\mathrm{cr}}$ from (3.21) shown in figure 3.6 to provide good decoupling for the critical axial load range around the critical buckling load.

In the following, first, the modal equation of motion and modal output equation are presented. Second, the state space representation and the transfer function of the modal beam-column model in the frequency domain are derived.

Modal equation of motion and output equation

Inserting (3.32) in the FE equation of motion (3.23) and left-multiplying by $\boldsymbol{\Phi}^T$ results in the modal equation of motion (index m)

$$\boldsymbol{M}_{\mathrm{m}}\,\ddot{\boldsymbol{q}}(t)+\boldsymbol{D}_{\zeta,\mathrm{m}}\,\dot{\boldsymbol{q}}(t)+\left(\boldsymbol{K}_{\mathrm{e,m}}-F_x(t)\,\boldsymbol{K}_{\mathrm{g,m}}\right)\boldsymbol{q}(t)=\boldsymbol{B}_{\boldsymbol{u},\mathrm{m}}\,\boldsymbol{u}_{\mathrm{b}}(t)+\boldsymbol{B}_{\boldsymbol{d},\mathrm{m}}\,\boldsymbol{d}(t), \quad (3.33)$$

with decoupled $[4\times4]$ modal mass matrix $\boldsymbol{M}_{\mathrm{m}}$, modal damping matrix $\boldsymbol{D}_{\zeta,\mathrm{m}}$, modal elastic stiffness matrix $\boldsymbol{K}_{\mathrm{e,m}}$ and modal geometric stiffness matrix $\boldsymbol{K}_{\mathrm{g,m}}$ given by

$$\begin{aligned}\boldsymbol{M}_{\mathrm{m}}&=\boldsymbol{\Phi}^T\,\boldsymbol{M}\,\boldsymbol{\Phi}, & \boldsymbol{D}_{\zeta,\mathrm{m}}&=\boldsymbol{\Phi}^T\,\boldsymbol{D}_{\zeta}\boldsymbol{\Phi},\\ \boldsymbol{K}_{\mathrm{e,m}}&=\boldsymbol{\Phi}^T\,\boldsymbol{K}_{\mathrm{e}}\boldsymbol{\Phi} \quad \text{and} & \boldsymbol{K}_{\mathrm{g,m}}&=\boldsymbol{\Phi}^T\,\boldsymbol{K}_{\mathrm{g}}\boldsymbol{\Phi}\end{aligned} \quad (3.34)$$

as well as the decoupled $[4\times2]$ modal input matrices for the active piezoelectric forces $\boldsymbol{B}_{\boldsymbol{u},\mathrm{m}}$ and disturbance end moments $\boldsymbol{B}_{\boldsymbol{d},\mathrm{m}}$ given by

$$\boldsymbol{B}_{\boldsymbol{u},\mathrm{m}}=\boldsymbol{\Phi}^T\,\boldsymbol{B}_{\boldsymbol{u},0} \quad \text{and} \quad \boldsymbol{B}_{\boldsymbol{d},\mathrm{m}}=\boldsymbol{\Phi}^T\,\boldsymbol{B}_{\boldsymbol{d},0}. \quad (3.35)$$

The FE output equation $\boldsymbol{C}_{\boldsymbol{y},0}$ in (3.30) is decoupled and truncated by inserting (3.32). However, the truncation results in an underestimation of the static system response since the static contributions of the higher modes are neglected, [72]. To compensate this effect, the static contributions of the higher modes are included in the output equation according to [72] via the $[2\times2]$ modal feedthrough matrices for the actuator voltages

$$\boldsymbol{D}_{\boldsymbol{u},\mathrm{b}}=\boldsymbol{C}_{\boldsymbol{y},0}\left[\boldsymbol{K}_{\mathrm{e}}^{-1}-\boldsymbol{\Phi}\,\boldsymbol{K}_{\mathrm{e,m}}\,\boldsymbol{\Phi}^T\right]\boldsymbol{B}_{\boldsymbol{u},0} \quad (3.36)$$

and the disturbance end moments

$$\boldsymbol{D}_{\boldsymbol{d},\mathrm{b}}=\boldsymbol{C}_{\boldsymbol{y},0}\left[\boldsymbol{K}_{\mathrm{e}}^{-1}-\boldsymbol{\Phi}\,\boldsymbol{K}_{\mathrm{e,m}}\,\boldsymbol{\Phi}^T\right]\boldsymbol{B}_{\boldsymbol{d},0}. \quad (3.37)$$

The resulting output equation of the reduced modal model is

$$\boldsymbol{y}_{\mathrm{b}}(t)=\boldsymbol{C}_{\boldsymbol{y},\mathrm{m}}\,\boldsymbol{q}(t)+\boldsymbol{D}_{\boldsymbol{u},\mathrm{b}}\,\boldsymbol{u}_{\mathrm{b}}(t)+\boldsymbol{D}_{\boldsymbol{d},\mathrm{b}}\,\boldsymbol{d}(t), \quad (3.38)$$

with the decoupled $[2\times4]$ modal output matrix

$$\boldsymbol{C}_{\boldsymbol{y},\mathrm{m}}=\boldsymbol{C}_{\boldsymbol{y},0}\,\boldsymbol{\Phi}. \quad (3.39)$$

3.2.3 Beam-column transfer function

Equations (3.33) and (3.38) represent the four degrees of freedom reduced modal model of the beam-column with piezo-elastic supports. In the following, they are written in state space representation to derive the beam-column transfer function, which is needed to include the influence of the electrical components in the beam-column plant in section 3.2.4. The $[8 \times 1]$ modal state vector of the modal beam-column model (index b) with modal displacements and velocities

$$\boldsymbol{x}_{\mathrm{b}}(t) = \begin{bmatrix} \boldsymbol{q}(t) \\ \dot{\boldsymbol{q}}(t) \end{bmatrix} \tag{3.40}$$

is used to set up the modal state space equations of first order and the output equation with eight degrees of freedom

$$\begin{aligned} \dot{\boldsymbol{x}}_{\mathrm{b}}(t) &= \underbrace{\begin{bmatrix} \mathbf{0} & \mathbf{I} \\ -\boldsymbol{M}_{\mathrm{m}}^{-1}\left(\boldsymbol{K}_{\mathrm{e,m}} - F_x(t)\,\boldsymbol{K}_{\mathrm{g,m}}\right) & -\boldsymbol{M}_{\mathrm{m}}^{-1}\,\boldsymbol{D}_{\zeta,\mathrm{m}} \end{bmatrix}}_{\boldsymbol{A}_{\mathrm{b}}\left(F_x(t)\right),\ [8\times 8]} \boldsymbol{x}_{\mathrm{b}}(t) \\ &\quad + \underbrace{\begin{bmatrix} \mathbf{0} \\ \boldsymbol{M}_{\mathrm{m}}^{-1}\,\boldsymbol{B}_{\boldsymbol{u},\mathrm{m}} \end{bmatrix}}_{\boldsymbol{B}_{\boldsymbol{u},\mathrm{b}},\ [8\times 2]} \boldsymbol{u}_{\mathrm{b}}(t) + \underbrace{\begin{bmatrix} \mathbf{0} \\ \boldsymbol{M}_{\mathrm{m}}^{-1}\,\boldsymbol{B}_{\boldsymbol{d},\mathrm{m}} \end{bmatrix}}_{\boldsymbol{B}_{\boldsymbol{d},\mathrm{b}},\ [8\times 2]} \boldsymbol{d}(t) \\ \boldsymbol{y}_{\mathrm{b}}(t) &= \underbrace{\begin{bmatrix} \boldsymbol{C}_{\boldsymbol{y},\mathrm{m}} & \mathbf{0} \end{bmatrix}}_{\boldsymbol{C}_{\boldsymbol{y},\mathrm{b}},\ [2\times 8]} \boldsymbol{x}_{\mathrm{b}}(t) + \underbrace{\boldsymbol{D}_{\boldsymbol{u},\mathrm{b}}}_{[2\times 2]}\,\boldsymbol{u}_{\mathrm{b}}(t) + \underbrace{\boldsymbol{D}_{\boldsymbol{d},\mathrm{b}}}_{[2\times 2]}\,\boldsymbol{d}(t) \end{aligned} \tag{3.41}$$

with zero and identity matrices $\mathbf{0}$ and $\mathbf{I}$ of appropriate dimensions, [33]. The linear influence of axial load $F_x(t)$ on the beam-column is included in the LPV system matrix

$$\boldsymbol{A}_{\mathrm{b}}\left(F_x(t)\right) = \boldsymbol{A}_{\mathrm{b,e}} + F_x(t)\,\boldsymbol{A}_{\mathrm{b,g}} \tag{3.42}$$

with an elastic and a geometric component. The beam-column model, thus, is an LPV system with the axial load as varying parameter, [4, 39]. According to [3], the LPV system can be interpreted as a linear time variant (LTV) system, where the state-space matrices are fixed functions of the time-dependent, dynamic axial load $F_x(t)$. For static axial loads $F_x(t) = \text{const.}$, the beam-column model reduces to an LTI system. For simplicity, the time-dependent axial force will be written as $F_x = F_x(t)$ in the following.

To derive the beam-column transfer function, the modal beam-column model (3.41) given in the time domain is transformed into the frequency domain, which is used throughout the thesis, by the LAPLACE transformation, [30]. The state space realization of the modal beam-column model (3.41) with LAPLACE variable s is

$$\begin{aligned} s\,\boldsymbol{x}_{\mathrm{b}}(s) &= \boldsymbol{A}_{\mathrm{b}}(F_x)\,\boldsymbol{x}_{\mathrm{b}}(s) + \boldsymbol{B}_{\boldsymbol{u},\mathrm{b}}\,\boldsymbol{u}_{\mathrm{b}}(s) + \boldsymbol{B}_{\boldsymbol{d},\mathrm{b}}\,\boldsymbol{d}(s) \\ \boldsymbol{y}_{\mathrm{b}}(s) &= \quad \boldsymbol{C}_{\boldsymbol{y},\mathrm{b}}\;\boldsymbol{x}_{\mathrm{b}}(s) + \boldsymbol{D}_{\boldsymbol{u},\mathrm{b}}\,\boldsymbol{u}_{\mathrm{b}}(s) + \boldsymbol{D}_{\boldsymbol{d},\mathrm{b}}\,\boldsymbol{d}(s). \end{aligned} \tag{3.43}$$

The disturbance end moments $\boldsymbol{d}(s)$ (3.27) are used for the controller synthesis in section 3.3. In order to add the influence of the electrical components in section 3.2.4, they are neglected and only the transfer behavior from the actuator voltages $\boldsymbol{u}_{\mathrm{b}}(s)$ (3.25) to the beam-column strains (3.29) $\boldsymbol{y}_{\mathrm{b}}(s)$, as shown in figure 3.2, is considered. The $[2 \times 2]$ matrix of transfer functions is obtained from (3.43) according to

$$\begin{aligned} \boldsymbol{G}_{\mathrm{b}}(F_x, s) = \frac{\boldsymbol{y}_{\mathrm{b}}(s)}{\boldsymbol{u}_{\mathrm{b}}(s)} &= \boldsymbol{C}_{\boldsymbol{y},\mathrm{b}} \left(\mathbf{I}s - \boldsymbol{A}_{\mathrm{b}}(F_x)\right)^{-1} \boldsymbol{B}_{\boldsymbol{u},\mathrm{b}} + \boldsymbol{D}_{\boldsymbol{u},\mathrm{b}} \\ &\overset{s}{=} \left[\begin{array}{c|c} \boldsymbol{A}_{\mathrm{b}}(F_x) & \boldsymbol{B}_{\boldsymbol{u},\mathrm{b}} \\ \hline \boldsymbol{C}_{\boldsymbol{y},\mathrm{b}} & \boldsymbol{D}_{\boldsymbol{u},\mathrm{b}} \end{array}\right] \end{aligned} \tag{3.44}$$

where the last part of (3.44) is a short notation for the transfer function of the four state space matrices $\boldsymbol{A}_{\mathrm{b}}(F_x)$, $\boldsymbol{B}_{\boldsymbol{u},\mathrm{b}}$, $\boldsymbol{C}_{\boldsymbol{y},\mathrm{b}}$ and $\boldsymbol{D}_{\boldsymbol{u},\mathrm{b}}$, [85].

3.2.4 Beam-column plant

In section 3.2.3, the axial load-dependent beam-column transfer function $\boldsymbol{G}_{\mathrm{b}}(F_x, s)$ (3.44) was derived, which represents the beam-column model without disturbance end moments $\boldsymbol{d}(s)$ (3.27), as shown in figure 3.2. For the practical implementation of the active buckling control, section 4.2, the electrical components for signal conditioning are included in the beam-column plant. It is important to model the electrical components to properly capture the lateral dynamic behavior of the beam-column system seen by the controller. Otherwise, disregarded phase shifts introduced by the electrical components could lead to controller instability in the experiments. The goal of this section is to model the beam-column plant that includes the beam-column transfer function (3.44) extended by the transfer functions of the electrical components.

The beam-column plant is given by the $[2 \times 2]$ transfer function matrix

$$\boldsymbol{P}(F_x, s) = \frac{\boldsymbol{y}(s)}{\boldsymbol{u}(s)} = \boldsymbol{G}_{\mathrm{rt}}(s)\, \boldsymbol{G}_{\mathrm{sg}}(s)\, \boldsymbol{G}_{\mathrm{b}}(F_x, s)\, \boldsymbol{G}_{\mathrm{pa}}(s)\, \boldsymbol{G}_{\mathrm{rf}}(s) \tag{3.45}$$

as a series connection of the individual transfer functions, as shown in figure 3.7.

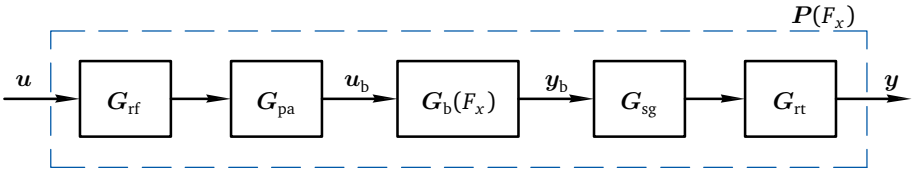

Figure 3.7.: Block diagram of the beam-column plant $\boldsymbol{P}(F_x)$

The input of the beam-column plant (3.45) is the control input generated by the controller

$$\boldsymbol{u}(s) = \begin{bmatrix} u_y(s) \\ u_z(s) \end{bmatrix}, \tag{3.46}$$

with components in y- and z-direction. To generate the actuator voltages $\boldsymbol{u}_{\mathrm{b}}(s)$ (3.25), the control input (3.46) is smoothed by analog low-pass reconstruction filters (index rf) and amplified by piezo amplifiers (index pa)

$$\boldsymbol{u}_{\mathrm{b}}(s) = \boldsymbol{G}_{\mathrm{pa}}(s)\, \boldsymbol{G}_{\mathrm{rf}}(s)\, \boldsymbol{u}(s). \tag{3.47}$$

The output of the beam-column plant (3.45) is the measurement output seen by the controller

$$\boldsymbol{y}(s) = \begin{bmatrix} y_y(s) \\ y_z(s) \end{bmatrix}, \tag{3.48}$$

with components in y- and z-direction. The measurement outputs (3.48) are the beam-column surface strains $\boldsymbol{y}_{\mathrm{b}}(s)$ (3.29), which are amplified and filtered by strain gauge amplifiers (index sg) and converted into a digital signal in the real-time platform (index rt)

$$\boldsymbol{y}(s) = \boldsymbol{G}_{\mathrm{rt}}(s)\, \boldsymbol{G}_{\mathrm{sg}}(s)\, \boldsymbol{y}_{\mathrm{b}}(s). \tag{3.49}$$

The $[2 \times 2]$ transfer function matrices for the electrical components in (3.45) are diagonal matrices with scalar transfer functions, which are introduced in the following.

The **reconstruction filters** are 8th order BESSEL low-pass filters with cutoff frequency f_{rf}. BESSEL filters are chosen because no steep cutoff of the amplitude is needed to smooth the control input. Furthermore, they offer a linear phase shift and constant group delay within the passband. The order results from the available amplifier hardware, section 4.2. The transfer function $G_{\mathrm{BESSEL}}(f_{\mathrm{rf}})$ is synthesized by the MATLAB® *besself* command, [2, 65].

$$G_{\mathrm{rf}}(s) = G_{\mathrm{BESSEL}}(f_{\mathrm{rf}}) \tag{3.50}$$

The **piezo amplifiers** are modeled with constant gain, which is admissible in the considered frequency range.

$$G_{\mathrm{pa}}(s) = c_{\mathrm{pa}} \tag{3.51}$$

The **strain gauge amplifiers** amplify the strain signals with amplification c_{sg} and apply 6th order BUTTERWORTH low-pass filters with cutoff frequency f_{sg}. BUTTERWORTH filters are chosen because they provide a relatively steep cutoff of the amplitude, which is needed to avoid anti-aliasing. The order results from the available hardware settings, section 4.2. The transfer function $G_{\mathrm{BUTTER}}(f_{\mathrm{sg}})$ is synthesized by the MATLAB® *butter* command, [2, 65].

$$G_{\mathrm{sg}}(s) = c_{\mathrm{sg}}\, G_{\mathrm{BUTTER}}(f_{\mathrm{sg}}) \tag{3.52}$$

The **real-time platform** is represented by 2nd order Padé zero order hold (ZOH) approximations with time delay T_{rt} according to [59, 85] to account for the phase delay introduced by the analog-digital conversion (ADC), computing time and digital-analog conversion (DAC).

$$G_{\mathrm{rt}}(s) = \frac{s^2 - 6/T_{\mathrm{rt}} + 12/T_{\mathrm{rt}}^2}{s^2 + 6/T_{\mathrm{rt}} + 12/T_{\mathrm{rt}}^2} \tag{3.53}$$

The resulting beam-column plant is written in form of the state space matrices analog to (3.44) as

$$\boldsymbol{P}(F_x, s) \overset{s}{=} \left[\begin{array}{c|c} \boldsymbol{A}(F_x) & \boldsymbol{B_u} \\ \hline \boldsymbol{C_y} & \boldsymbol{0} \end{array}\right]. \tag{3.54}$$

As in (3.42), the LPV system matrix

$$\boldsymbol{A}(F_x) = \boldsymbol{A}_{\mathrm{e}} + F_x\, \boldsymbol{A}_{\mathrm{g}} \tag{3.55}$$

linearly depends on the axial load F_x and has an elastic and a geometric component, but now includes the states of the electrical components.

In contrast to the beam-column model (3.42), the beam-column plant does not have direct feedthrough, i.e. $\boldsymbol{D} = \mathbf{0}$, which results from the missing feedthrough components in the transfer functions of the electrical components (3.50) to (3.53).

For the controller synthesis in section 3.3, the disturbance end moments (3.27) are again added to the beam-column plant

$$\boldsymbol{P}_{\mathrm{d}}(F_x, s) \stackrel{s}{=} \left[\begin{array}{c|cc} \boldsymbol{A}(F_x) & \boldsymbol{B_u} & \boldsymbol{B_d} \\ \hline \boldsymbol{C_y} & \mathbf{0} & \mathbf{0} \end{array}\right]. \tag{3.56}$$

The disturbance end moments still affect the beam-column directly. However, the disturbance input matrix from (3.43) is filled up with zero entries to fit the increased number of system states as $\boldsymbol{B_d} = [\boldsymbol{B}_{\boldsymbol{d},\mathrm{b}}, \mathbf{0}]^T$ and the disturbance feedthrough matrix becomes zero.

3.3 Active buckling control

In this section, the active buckling control of the beam-column system from section 3.1 is presented. First, the selection of a control concept based on the controller requirements is shown. Second, the disturbed beam-column plant from the previous section is augmented to the open-loop plant, which is used for the model-based controller synthesis. Third, frequency-dependent controller weights are added to the open-loop plant to properly adjust the controller performance. Finally, the controller synthesis for the selected control concept is presented.

3.3.1 Selection of the control concept

In this thesis, the active buckling control is intended for an experimental beam-column system, section 4.1.1, that shows real buckling behavior with increasing lateral deflections for increasing axial loads due to inherent uncertainty in the material, geometry, loading or the support properties, figure 2.3. The goal of the active buckling control, therefore, is to minimize the lateral beam-column deflections and increase the maximum bearable axial load $F_{x,\max}$ for quasi-static and dynamic axial loads F_x.

As shown in section 3.2.4, the disturbed beam-column plant $\boldsymbol{P}_{\mathrm{d}}(F_x)$ (3.56) for model-based controller synthesis is an LPV system, in which the system matrix $\boldsymbol{A}(F_x)$ linearly depends on the axial load F_x and becomes instable for the critical buckling load $F_{x,\mathrm{cr}}$ from (3.21). Since the axial load dominates the lateral dynamic beam-column behavior, other sources of uncertainty, such as data and model uncertainty presented in section 2.3, are not considered for the controller synthesis. The experimental beam-column system is subject to dynamic axial loads $F_x(t)$ that are

- bounded by a lower and upper (indices l and u) axial load $F_{x,\mathrm{l}} \leq F_x(t) \leq F_{x,\mathrm{u}}$,
- may exceed the critical buckling load $F_{x,\mathrm{u}} > F_{x,\mathrm{cr}}$ and
- may change arbitrarily fast over time t.

So far, studies on active buckling control used LTI controllers for (quasi-)static axial loads $F_x(t) \approx$ const., which were either used for a large operation range of axial loads or were manually switched, section 2.2. These control concepts are not applicable for dynamic axial loads within a large operation range of axial loads $F_{x,\mathrm{l}} \leq F_x(t) \leq F_{x,\mathrm{u}}$. To deal with the parameter-dependency of LPV systems, APKARIAN ET AL. [4] mention three possible control concepts:

- robust control,
- gain-scheduled LTI control and
- LPV control.

The applicability of the mentioned control concepts for the presented beam-column plant is discussed in the following.

Robust control considers parameter uncertainty in the axial load F_x during the controller synthesis in form of structured or unstructured uncertainty, [85, 97, 98]. For models with unstructured uncertainty, powerful synthesis methods, in particular $\mathscr{H}_\infty$ controller synthesis, are available. However, the unstructured modeling of uncertainty is physically less meaningful and often leads to highly conservative controllers, [81, 97]. On the other hand, structured uncertainty allows a non-conservative system description with physically motivated parameter uncertainty, as e.g. would be effective for the large operation range of axial loads F_x. However,

the controller synthesis like the μ synthesis is mathematically much more complex, [22, 81, 97]. Due to the high mathematical complexity and the large operation range of axial loads $F_{x,\mathrm{l}} \leq F_x(t) \leq F_{x,\mathrm{u}}$, as experimentally investigated in this thesis, section 6.2, the robust control approach is dismissed.

Gain-scheduled LTI control calculates classic feedback controllers, e.g. proportional (P) and proportional-integral-derivative (PID), or optimal controllers, e.g. linear quadratic regulator (LQR), for discrete design points of the axial load F_x, which are tuned independently, and interpolates between them. This approach has been investigated in own studies [76, 77] and proved to be successful in active buckling control in case of quasi-static axial loads. However, changes in the axial load $F_x(t)$ can only allowed to be slow and stability of the closed-loop plant is only guaranteed at the design points and for static loads, [4, 83]. Since the beam-column in this thesis is loaded by arbitrarily changing dynamic axial loads $F_x(t)$, the gain-scheduled LTI control approach is dismissed as well.

LPV control considers the axial load-dependency of the open-loop plant in the controller synthesis. It is suitable, if the axial load $F_x(t)$ can be measured accurately and reliably in real-time, as is the case in this thesis, section 4.1. In particular, LPV controllers based on the $\mathscr{H}_\infty$ performance are found in literature, [4, 9, 44, 70, 82]. The gain-scheduled $\mathscr{H}_\infty$ control results in a dynamic and axial load-dependent LPV controller $\boldsymbol{R}(F_x, s)$, which guarantees stability and robust performance for the entire range of operation and arbitrary fast changes of the axial load F_x. Therefore, the LPV control approach, in particular gain-scheduled $\mathscr{H}_\infty$ control as presented in [79], is selected for active buckling control in this thesis.

The gain-scheduled $\mathscr{H}_\infty$ control is an output feedback control method in the frequency domain resulting from a model-based controller synthesis. The output feedback controller directly determines the control input $\boldsymbol{u}(s)$ (3.46) from the measurement output $\boldsymbol{y}(s)$ (3.48) via the LPV controller $\boldsymbol{R}(F_x, s)$

$$\boldsymbol{u}(s) = \boldsymbol{R}(F_x, s)\, \boldsymbol{y}(s), \tag{3.57}$$

as shown in figure 3.2. In contrast to state feedback control, not all system states have to be measured or estimated, [97], as was done in previous own studies, [76, 78, 80]. Figure 3.8 shows the block diagram for the controller synthesis of the gain-scheduled $\mathscr{H}_\infty$ control. For simplicity, the dependency of the LAPLACE variable s is omitted in the following block diagrams.

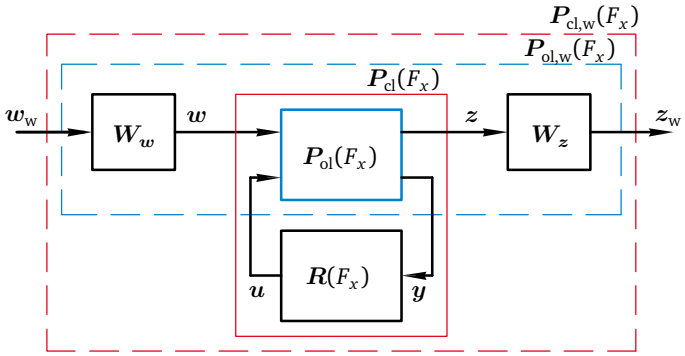

Figure 3.8.: Block diagram for controller synthesis: open-loop plant $\boldsymbol{P}_{\mathrm{ol}}(F_x,s)$ (——), closed-loop plant $\boldsymbol{P}_{\mathrm{cl}}(F_x,s)$ (——), weighted open-loop plant $\boldsymbol{P}_{\mathrm{ol,w}}(F_x,s)$ (– –) and weighted closed-loop plant $\boldsymbol{P}_{\mathrm{cl,w}}(F_x,s)$ (– –)

The still unknown dynamic LPV controller $\boldsymbol{R}(F_x,s)$ from (3.57) connects the measurement output $\boldsymbol{y}(s)$ (3.48) to the control input $\boldsymbol{u}(s)$ (3.46) of the open-loop plant (index ol) $\boldsymbol{P}_{\mathrm{ol}}(F_x,s)$, which is the augmented disturbed beam-column plant $\boldsymbol{P}_{\mathrm{d}}(F_x)$ (3.56) with additional exogenous input $\boldsymbol{w}(s)$ (3.60) and performance output $\boldsymbol{z}(s)$ (3.64). The open-loop plant and the additional exogenous input and performance output are derived in section 3.3.2. The resulting closed-loop plant (index cl)

$$\boldsymbol{P}_{\mathrm{cl}}(F_x,s)=\frac{\boldsymbol{z}(s)}{\boldsymbol{w}(s)}=\mathscr{F}_{\mathrm{l}}\big(\boldsymbol{P}_{\mathrm{ol}}(F_x,s),\boldsymbol{R}(F_x,s)\big) \tag{3.58}$$

is obtained by the lower linear fractional transformation (LFT) $\mathscr{F}_{\mathrm{l}}$ of the open-loop plant and the dynamic LPV controller, [85, 97]. It describes the relation of the exogenous input $\boldsymbol{w}(s)$ to the performance output $\boldsymbol{z}(s)$.

In order to tune the transfer behavior of the closed-loop plant $\boldsymbol{P}_{\mathrm{cl}}(F_x,s)$, it is augmented by frequency-dependent weights for the exogenous input, $\boldsymbol{W}_{\boldsymbol{w}}(s)$ and the performance output, $\boldsymbol{W}_{\boldsymbol{z}}(s)$, which are presented in section 3.3.3. The open- and closed-loop plants with additional input and output weights represent the weighted open- and closed-loop plant (index w) $\boldsymbol{P}_{\mathrm{ol,w}}(F_x,s)$ and $\boldsymbol{P}_{\mathrm{cl,w}}(F_x,s)$, figure 3.8. The weighted closed-loop plant is used for the synthesis of the gain-scheduled $\mathscr{H}_\infty$ controller, which is presented in section 3.3.4.

3.3.2 Open-loop plant

In this section, the open-loop plant, which is needed for the synthesis of the gain-scheduled $\mathscr{H}_\infty$ buckling control, is derived. In order to determine the dynamic LPV controller in (3.57), the disturbed beam-column plant $\boldsymbol{P}_\mathrm{d}(F_x, s)$ (3.56) is augmented to comply with the general control configuration shown in figure 3.8, [85, 97].

The open-loop plant $\boldsymbol{P}_\mathrm{ol}(F_x, s)$ describes the relation of the exogenous input $\boldsymbol{w}(s)$ (3.60) and the control input $\boldsymbol{u}(s)$ (3.46) to the performance output $\boldsymbol{z}(s)$ (3.64) and the measurement output $\boldsymbol{y}(s)$ (3.48) via

$$\begin{bmatrix} \boldsymbol{z}(s) \\ \boldsymbol{y}(s) \end{bmatrix} = \boldsymbol{P}_\mathrm{ol}(F_x, s) \begin{bmatrix} \boldsymbol{w}(s) \\ \boldsymbol{u}(s) \end{bmatrix}, \tag{3.59}$$

[85, 97]. In (3.59), the exogenous input vector

$$\boldsymbol{w}(s) = \begin{bmatrix} \boldsymbol{d}(s) \\ \boldsymbol{n}(s) \end{bmatrix} \tag{3.60}$$

contains the disturbance end moments $\boldsymbol{d}(s)$ (3.27) and additional measurement noise with components in y- and z-direction

$$\boldsymbol{n}(s) = \begin{bmatrix} n_y(s) \\ n_z(s) \end{bmatrix}, \tag{3.61}$$

which is added to the measurement output (3.48)

$$\boldsymbol{y}(s) = \boldsymbol{C}_{\boldsymbol{y}}\, \boldsymbol{x}(s) + \boldsymbol{n}(s). \tag{3.62}$$

By that, measurement noise that is present in the experiments, chapter 6, is represented in the controller synthesis to prevent high control amplification at high frequencies, section 3.3.3.

To reduce the lateral deflection of the beam-column by active buckling control with the available control inputs, the performance outputs (target – index t) are chosen as the measurement output without measurement noise and the control input (3.46) itself as

$$\boldsymbol{y}_\mathrm{t}(s) = \boldsymbol{C}_{\boldsymbol{y}}\, \boldsymbol{x}(s) \qquad \text{and} \qquad \boldsymbol{u}_\mathrm{t}(s) = \mathbf{I}\, \boldsymbol{u}(s). \tag{3.63}$$

They are combined in the performance output vector

$$\boldsymbol{z}(s) = \begin{bmatrix} \boldsymbol{y}_{\mathrm{t}}(s) \\ \boldsymbol{u}_{\mathrm{t}}(s) \end{bmatrix} = \boldsymbol{C}_{\boldsymbol{z}}\, \boldsymbol{x}(s) + \boldsymbol{D}_{\boldsymbol{z}}\, \boldsymbol{u}(s), \tag{3.64}$$

as in (3.59), with performance output and feedthrough matrices

$$\boldsymbol{C}_{\boldsymbol{z}} = \begin{bmatrix} \boldsymbol{C}_{\boldsymbol{y}} \\ \boldsymbol{0} \end{bmatrix} \qquad \text{and} \qquad \boldsymbol{D}_{\boldsymbol{z}} = \begin{bmatrix} \boldsymbol{0} \\ \mathbf{I} \end{bmatrix}. \tag{3.65}$$

Figure 3.9 shows the block diagram of the open-loop plant according to the system equation in (3.56), the modified measurement output equation (3.62) and the performance output equation (3.64).

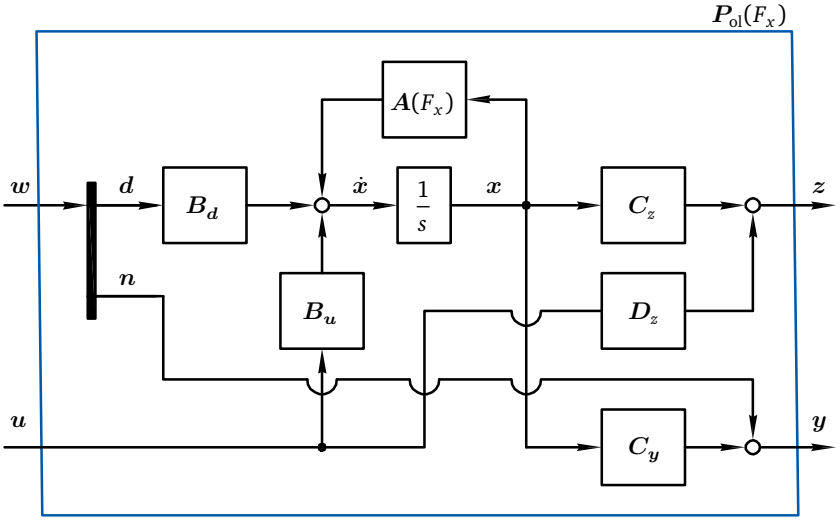

Figure 3.9.: Block diagram of the open-loop plant $\boldsymbol{P}_{\mathrm{ol}}(F_x, s)$ (——)

The resulting open-loop plant in state space representation is given by

$$\boldsymbol{P}_{\mathrm{ol}}(F_x, s) \overset{s}{=} \left[\begin{array}{c|cc} \boldsymbol{A}(F_x) & \boldsymbol{B}_{\boldsymbol{w}} & \boldsymbol{B}_{\boldsymbol{u}} \\ \hline \boldsymbol{C}_{\boldsymbol{z}} & \boldsymbol{0} & \boldsymbol{D}_{\boldsymbol{z}} \\ \boldsymbol{C}_{\boldsymbol{y}} & \boldsymbol{D}_{\boldsymbol{y}} & \boldsymbol{0} \end{array}\right], \tag{3.66}$$

where the input matrix

$$\boldsymbol{B}_w = \begin{bmatrix} \boldsymbol{B}_d & \mathbf{0} \end{bmatrix} \tag{3.67}$$

contains the disturbance input matrix $\boldsymbol{B}_d$ from (3.56) and the measurement feedthrough matrix is

$$\boldsymbol{D}_y = \begin{bmatrix} \mathbf{0} & \mathbf{I} \end{bmatrix}. \tag{3.68}$$

3.3.3 Controller weights

In order to tune the system dynamics of the closed-loop plant $\boldsymbol{P}_{\mathrm{cl}}(F_x)$ (3.58) and to achieve the desired controller performance in the frequency range of interest, the frequency-dependent input and output weights $\boldsymbol{W}_{\boldsymbol{w}}(s)$ and $\boldsymbol{W}_{\boldsymbol{z}}(s)$ in figure 3.8 are used. Figure 3.10 shows the same block diagram of the augmented open- and closed-loop plants as in figure 3.8 with separate frequency-dependent input and output weights for the exogenous input, $\boldsymbol{W}_{\boldsymbol{d}}(s)$ and $\boldsymbol{W}_{\boldsymbol{n}}(s)$, as well as the performance output, $\boldsymbol{W}_{\boldsymbol{y}}(s)$ and $\boldsymbol{W}_{\boldsymbol{u}}(s)$.

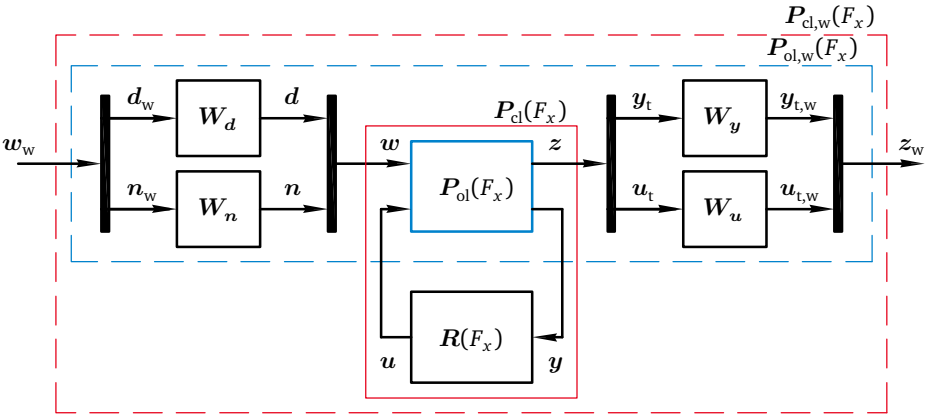

Figure 3.10.: Block diagram of augmented plants: open-loop plant $\boldsymbol{P}_{\mathrm{ol}}(F_x, s)$ (——), closed-loop plant $\boldsymbol{P}_{\mathrm{cl}}(F_x, s)$ (——), weighted open-loop plant $\boldsymbol{P}_{\mathrm{ol,w}}(F_x, s)$ (– –) and weighted closed-loop plant $\boldsymbol{P}_{\mathrm{cl,w}}(F_x, s)$ (– –)

The open-loop plant $\boldsymbol{P}_{\mathrm{ol}}(F_x, s)$ (3.66) with additional input and output weights results in the weighted open-loop plant $\boldsymbol{P}_{\mathrm{ol,w}}(F_x, s)$ with

$$\begin{bmatrix} \boldsymbol{z}_{\mathrm{w}}(s) \\ \boldsymbol{y}(s) \end{bmatrix} = \boldsymbol{P}_{\mathrm{ol,w}}(F_x, s) \begin{bmatrix} \boldsymbol{w}_{\mathrm{w}}(s) \\ \boldsymbol{u}(s) \end{bmatrix}. \tag{3.69}$$

The lower LFT $\mathscr{F}_l$ of the weighted open-loop plant (3.69) with control feedback (3.57) leads to the weighted closed-loop plant

$$\begin{aligned}\boldsymbol{P}_{\mathrm{cl,w}}(F_x,s) &= \frac{\boldsymbol{z}_{\mathrm{w}}(s)}{\boldsymbol{w}_{\mathrm{w}}(s)} = \mathscr{F}_l\big(\boldsymbol{P}_{\mathrm{ol,w}}(F_x,s),\boldsymbol{R}(F_x,s)\big) \\ &\stackrel{s}{=} \left[\begin{array}{c|c} \boldsymbol{A}_{\mathrm{cl}}(F_x) & \boldsymbol{B}_{\mathrm{cl}}(F_x) \\ \hline \boldsymbol{C}_{\mathrm{cl}}(F_x) & \boldsymbol{D}_{\mathrm{cl}}(F_x) \end{array}\right],\end{aligned} \tag{3.70}$$

which describes the relation of the weighted exogenous input $\boldsymbol{w}_{\mathrm{w}}(s)$ to the weighted performance output $\boldsymbol{z}_{\mathrm{w}}(s)$. The weighted exogenous input and weighted performance output are given by

$$\boldsymbol{w}_{\mathrm{w}}(s) = \begin{bmatrix} \boldsymbol{W}_{\boldsymbol{d}}^{-1}(s) & \boldsymbol{0} \\ \boldsymbol{0} & \boldsymbol{W}_{\boldsymbol{n}}^{-1}(s) \end{bmatrix} \boldsymbol{w}(s) \quad \text{and} \quad \boldsymbol{z}_{\mathrm{w}}(s) = \begin{bmatrix} \boldsymbol{W}_{\boldsymbol{y}}(s) & \boldsymbol{0} \\ \boldsymbol{0} & \boldsymbol{W}_{\boldsymbol{u}}(s) \end{bmatrix} \boldsymbol{z}(s). \tag{3.71}$$

The $[2\times 2]$ input weight matrices for the disturbance end moments $\boldsymbol{W}_{\boldsymbol{d}}(s) = \mathrm{diag}\,(W_{\boldsymbol{d}}(s), W_{\boldsymbol{d}}(s))$ and the measurement noise $\boldsymbol{W}_{\boldsymbol{n}}(s) = \mathrm{diag}\,(W_{\boldsymbol{n}}(s), W_{\boldsymbol{n}}(s))$ are chosen as diagonal matrices with scalar transfer functions $W(s)$. In the same way, the $[2\times 2]$ output weight matrices $\boldsymbol{W}_{\boldsymbol{y}}(s) = \mathrm{diag}\big(W_{\boldsymbol{y}}(s), W_{\boldsymbol{y}}(s)\big)$ and $\boldsymbol{W}_{\boldsymbol{u}}(s) = \mathrm{diag}\,(W_{\boldsymbol{u}}(s), W_{\boldsymbol{u}}(s))$ are obtained for the performance output.

The frequency-dependent input and output weights influence the transfer functions of the weighted closed-loop plant $\boldsymbol{P}_{\mathrm{cl,w}}(F_x,s)$ (3.70), which is used for controller synthesis according to (3.79). In general, a stronger weight increases the influence of an input or output in the controller synthesis for the specified frequency range. By that, the significance of individual transfer paths that are important for the active buckling control can be tuned. The weights are selected as simple as possible in order to keep the controller order low, [58, 97]. In the following, the scalar input and output weights are introduced.

The **weights on the disturbance end moments** $\boldsymbol{d}(s)$ (3.27) are used to increase the influence of static disturbance end moments in the weighted closed-loop plant. They are chosen as approximate integrators

$$W_{\boldsymbol{d}}(s) = \frac{b_{\boldsymbol{d}}}{s + a_{\boldsymbol{d}}} \tag{3.72}$$

with a small value of $a_{\boldsymbol{d}}$ to introduce integral action in the gain-scheduled $\mathscr{H}_\infty$ controller, which is necessary to achieve stationary accuracy in spite of static disturbance

end moments $\boldsymbol{d}(s)$ that counteract the active stabilization, [85, 97]. The amplitude and phase response of the input weight transfer function for the disturbance end moments $W_{\boldsymbol{d}}(s)$ is shown in figure 3.11a).

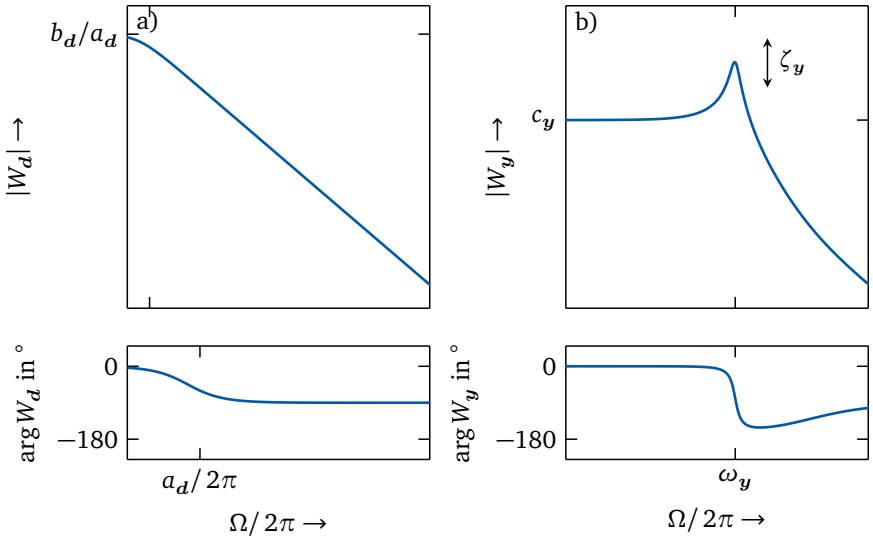

Figure 3.11.: Amplitude and phase responses of the input and output weight transfer functions plotted versus excitation frequency $\Omega/2\pi$, a) disturbance end moments $W_{\boldsymbol{d}}(\Omega)$, b) measurement output without measurement noise $W_{\boldsymbol{y}}(\Omega)$

The **weights on the measurement noise** $\boldsymbol{n}(s)$ (3.61) are chosen constant in order to be as simple as possible,

$$W_{\boldsymbol{n}}(s) = c_{\boldsymbol{n}}. \tag{3.73}$$

The **weights on the performance measurement output** $\boldsymbol{y}_t(s)$ (3.63) are used to increase the influence of the performance measurement output around the beam-column's second mode of vibration in the weighted closed-loop plant. They are chosen as second order dynamic filters

$$W_{\boldsymbol{y}}(s) = c_{\boldsymbol{y}} \frac{2\zeta_{\boldsymbol{y}}\omega_{\boldsymbol{y}} s + \omega_{\boldsymbol{y}}^2}{s^2 + 2\zeta_{\boldsymbol{y}}\omega_{\boldsymbol{y}} s + \omega_{\boldsymbol{y}}^2}. \tag{3.74}$$

with resonance frequency $\omega_{\boldsymbol{y}}/2\pi$, damping ratio $\zeta_{\boldsymbol{y}}$ and constant gain $c_{\boldsymbol{y}}$.

By that, the controller can be forced to not operate in the frequency range of the beam-column's second mode of vibration. This is necessary, as the second mode of vibration is observed in some experiments, figure 5.3, despite of in theory being not controllable and observable due to the chosen actuator and sensor arrangement, section 3.1. The amplitude and phase response of the output weight transfer function for the performance measurement output $W_{\boldsymbol{y}}(s)$ is shown in figure 3.11b).

The **weights on the performance control output** $u_{\mathrm{t}}(s)$ (3.63) are chosen as fourth order high-pass filters with cutoff frequency $\omega_{\boldsymbol{u}}/2\pi$ that ensure low noise amplification at high frequencies outside the frequency range of interest,

$$W_{\boldsymbol{u}}(s) = c_{\boldsymbol{u}} \left(\frac{b_{\boldsymbol{u}}^{-1/4} s + \omega_{\boldsymbol{u}}}{s + \omega_{\boldsymbol{u}} a_{\boldsymbol{u}}^{1/4}} \right)^4 . \tag{3.75}$$

The parameters of the frequency-dependent input and output weights (3.72) to (3.75) are presented later in table 5.6. They are the result of the controller tuning, section 5.3, which is performed with the calibrated weighted closed-loop plant $\boldsymbol{P}_{\mathrm{cl,w}}(F_x, s)$ (3.70).

3.3.4 Controller synthesis

In the following, the synthesis of the dynamic LPV controller $\boldsymbol{R}(F_x, s)$ in (3.57) based on the weighted closed-loop plant (3.70) is presented. The controller (index c) is given by the transfer function

$$\boldsymbol{R}(F_x, s) \overset{s}{=} \left[\begin{array}{c|c} \boldsymbol{A}_{\mathrm{c}}(F_x) & \boldsymbol{B}_{\mathrm{c}}(F_x) \\ \hline \boldsymbol{C}_{\mathrm{c}}(F_x) & \boldsymbol{D}_{\mathrm{c}}(F_x) \end{array}\right]. \tag{3.76}$$

The dynamic LPV controller is equally dependent on axial load F_x as the underlying open-loop plant (3.66) with elastic and geometric part and is determined via the axial load-dependent state space matrices

$$\begin{aligned} \boldsymbol{A}_{\mathrm{c}}(F_x) &= \boldsymbol{A}_{\mathrm{c,e}} + F_x \boldsymbol{A}_{\mathrm{c,g}}, & \boldsymbol{B}_{\mathrm{c}}(F_x) &= \boldsymbol{B}_{\mathrm{c,e}} + F_x \boldsymbol{B}_{\mathrm{c,g}}, \\ \boldsymbol{C}_{\mathrm{c}}(F_x) &= \boldsymbol{C}_{\mathrm{c,e}} + F_x \boldsymbol{C}_{\mathrm{c,g}} \quad \text{and} & \boldsymbol{D}_{\mathrm{c}}(F_x) &= \boldsymbol{D}_{\mathrm{c,e}} + F_x \boldsymbol{D}_{\mathrm{c,g}}. \end{aligned} \tag{3.77}$$

A sufficient criterion for the asymptotic stability of the closed-loop system matrix $\boldsymbol{A}_{\mathrm{cl}}(F_x)$ in (3.70) is the existence of a positive definite, parameter-independent,

quadratic LYAPUNOV function $L(\boldsymbol{x}_{\mathrm{cl}}) = \boldsymbol{x}_{\mathrm{cl}}^T \boldsymbol{X}\, \boldsymbol{x}_{\mathrm{cl}}$, where $\boldsymbol{x}_{\mathrm{cl}}$ is the state vector of the closed-loop plant and $\boldsymbol{X} \succ 0$ is an arbitrary positive definite matrix, for which the condition

$$\boldsymbol{A}_{\mathrm{cl}}^T(F_x)\, \boldsymbol{X} + \boldsymbol{X}\, \boldsymbol{A}_{\mathrm{cl}}(F_x) \prec 0 \tag{3.78}$$

is satisfied for any $F_x(t)$, [9, 15]. For asymptotically stable LPV systems, the performance of the closed-loop plant is characterized by the induced $\mathscr{L}_2$-norm of the weighted closed-loop plant (3.70), [4]. The goal of the gain-scheduled $\mathscr{H}_\infty$ control is to minimize

$$\left|\left| \boldsymbol{P}_{\mathrm{cl,w}}(F_x, s) \right|\right|_{\mathscr{L}_2} = \sup_{\boldsymbol{w}_{\mathrm{w}} \neq 0} \frac{\left|\left| \boldsymbol{z}_{\mathrm{w}}(s) \right|\right|_2}{\left|\left| \boldsymbol{w}_{\mathrm{w}}(s) \right|\right|_2} \leq \gamma, \tag{3.79}$$

to lie below γ for arbitrary trajectories of the variable axial load $F_x(t)$ by optimizing the dynamic LPV controller $\boldsymbol{R}(F_x, s)$ (3.77).

The weighted closed-loop plant (3.70) is stable and has quadratic $\mathscr{H}_\infty$ performance γ if there exists a positive definite matrix $\boldsymbol{X} \succ 0$ that satisfies the condition known as Bounded Real Lemma (BRL)

$$\mathscr{B}_{\boldsymbol{P}_{\mathrm{cl,w}}(F_x)}(\boldsymbol{X}, \gamma) = \begin{bmatrix} \boldsymbol{A}_{\mathrm{cl}}^T(F_x)\, \boldsymbol{X} + \boldsymbol{X}\, \boldsymbol{A}_{\mathrm{cl}}(F_x) & \boldsymbol{X}\, \boldsymbol{B}_{\mathrm{cl}}(F_x) & \boldsymbol{C}_{\mathrm{cl}}^T(F_x) \\ \boldsymbol{B}_{\mathrm{cl}}^T(F_x)\, \boldsymbol{X} & -\gamma\, \boldsymbol{I} & \boldsymbol{D}_{\mathrm{cl}}^T(F_x) \\ \boldsymbol{C}_{\mathrm{cl}}(F_x) & \boldsymbol{D}_{\mathrm{cl}}(F_x) & -\gamma\, \boldsymbol{I} \end{bmatrix} \prec 0, \tag{3.80}$$

[4]. The BRL has to be satisfied for arbitrary axial loads $F_x(t)$ which results in an infinite number of constraints. However, in the special case of polytopic LPV systems, it is sufficient to solve the BRL for the vertices of the polytopic LPV system, [4].

For the weighted closed-loop plant (3.70) with only one linear-dependent parameter, the axial load $F_x(t)$, the operation range of the gain-scheduled $\mathscr{H}_\infty$ controller is defined by $F_{x,\mathrm{l}} \leq F_x \leq F_{x,\mathrm{u}}$. Thus, the weighted closed-loop plant is a polytopic LPV system with the vertices $\boldsymbol{P}_{\mathrm{cl,w}}(F_{x,\mathrm{l}})$ and $\boldsymbol{P}_{\mathrm{cl,w}}(F_{x,\mathrm{u}})$, [39]. The BRL (3.80) is, thus, solved simultaneously for the two weighted closed-loop plants. This problem can be reformulated as a set of linear matrix inequalities (LMI) as is well documented in [4, 8, 82]. In this thesis, the controller synthesis is performed with the MATLAB® *Robust Control Toolbox*, [6, 39]. The numerical verification of the gain-scheduled $\mathscr{H}_\infty$ buckling controller performance is presented in, section 5.3.2.

4 Experimental test setup

This chapter introduces the experimental realization of the beam-column system from section 3.1 and the test setup used for the experimental investigation of passive buckling and active buckling control in sections 6.2 and 6.3. Section 4.1 presents the test setup and the mechanical components of the beam-column system. Section 4.2 presents the electrical components for signal processing and the measurement setup.

4.1 Mechanical test setup components

In this section, first, the experimental test setup and the mechanical components of the beam-column system from section 3.1 are introduced. Second, the components of the piezo-elastic support are explained in detail. Finally, the variation of mechanical components from the beam-column system used for the experimental quantification and evaluation of probabilistic uncertainty in the lateral dynamic behavior in chapter 5 and passive buckling and active buckling control in chapter 6 is presented.

4.1.1 Test setup and beam-column with piezo-elastic supports

For the experimental investigation of passive buckling and active buckling control of a beam-column with circular cross-section and piezo-elastic supports subject to quasi-static and dynamic axial loads $F_x(t)$, as motivated in section 2.4, the experimental test setup shown in figure 4.1 was designed and realized in the scope of this thesis. The main functions of the test setup are to provide the mounts of the beam-column's piezo-elastic supports, which are fixed at the bottom and free to move in axial direction at the top, and to generate the quasi-static and dynamic axial loads $F_x(t)$, as shown in figure 3.1.

The central component of the experimental test setup is the beam-column with circular cross-section and piezo-elastic supports (no. 1) from figure 4.1. A close-up photo of the beam-column is provided in figure 4.2. The beam-column's lower

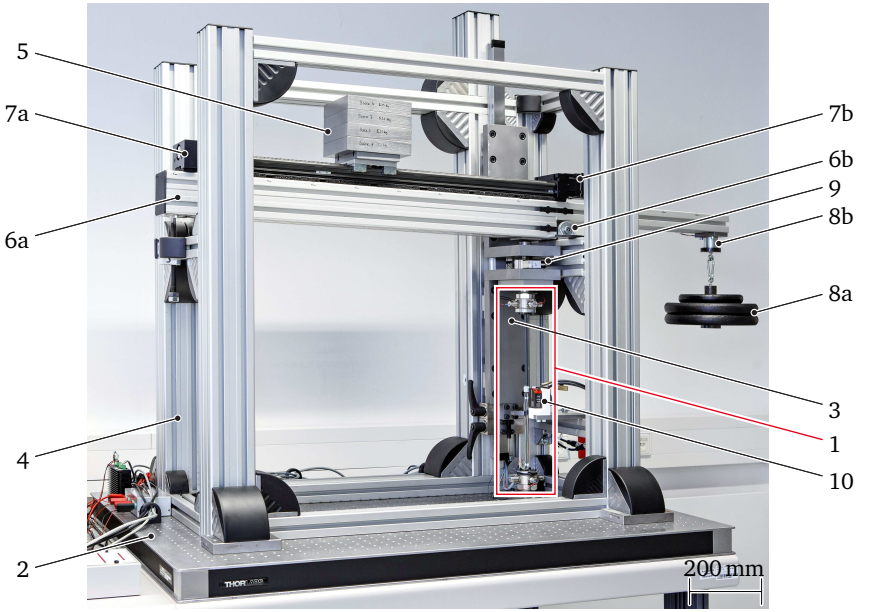

Figure 4.1.: Experimental test setup and beam-column with piezo-elastic supports (——) for active buckling control (close-up photo in figure 4.2)

piezo-elastic support is fixed to a baseplate (no. 2) and the upper piezo-elastic support is fixed to a parallel guidance (no. 3), which is connected to a stiff frame structure (no. 4). Thus, the upper piezo-elastic support is free to move in axial beam-column direction. The beam-column is loaded via a high lever ratio by a shiftable mass (no. 5) placed on a stiff beam (no. 6a), which is supported by a hinge (no. 6b). The lever ratio and, therefore, the axial load are increased by shifting the mass in nearly horizontal plane via a linear axle (no. 7a), which is operated by a stepper motor (no. 7b). With this test setup design, slowly increasing quasi-static axial loads $F_x(t) \approx$ const. can be introduced at the upper piezo-elastic support, section 6.2. An additional (optional) releasable mass (no. 8a) reduces the axial load on the beam-column. It can be released by an electromagnet (no. 8b), thus generating dynamic, approximately step-shaped axial compressive loads $F_x(t) \neq$ const. at the upper piezo-elastic support, section 6.3.

In both cases, the axial load $F_x(t)$ is measured by a strain gauge-based load cell (no. 9). Furthermore, laser distance sensors (no. 10) measure the position of the

beam-column center in y- and z-direction relative to the stiff frame structure (no. 4). The relative position is used to assure a consistent positioning of the beam-column center each time a new beam-column with piezo-elastic supports is mounted. This way, the experimental results for passive buckling and active buckling control of different beam-column systems are comparable, chapter 6.

Figure 4.2 shows a close-up photo of the beam-column with piezo-elastic supports (no. 1) in figure 4.1. The beam-column with circular solid cross-section (no. 1a) is made from high-strength aluminum to avoid plastic deformation due to beam-column buckling, [89]. It's lower and upper ends are connected to the piezo-elastic supports (no. A) and (no. B), which are fixed to the baseplate (no. 2) and the parallel guidance (no. 3), respectively. Section 4.1.2 gives a detailed description of the piezo-elastic supports.

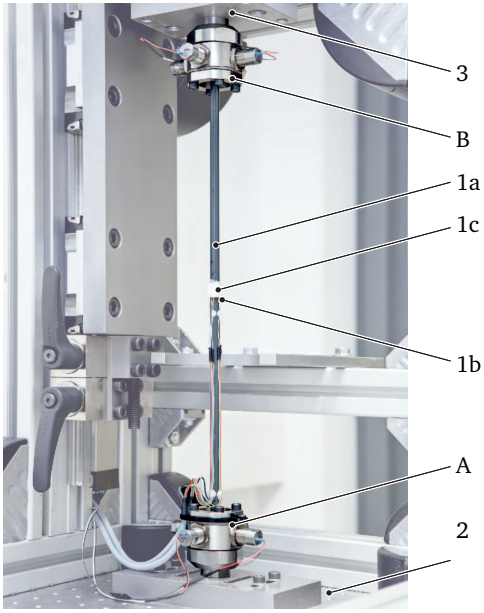

Figure 4.2.: Beam-column with piezo-elastic supports for experiments (laser sensors removed for visibility)

Four strain gauge sensors (no. 1b) at the sensor position x_s, connected as two WHEATSTONE half bridges, [45], measure the surface strains due to bending $y_b(t)$ (3.29) in y- and z-direction. Furthermore, laser reflectors (no. 1c) are attached

to the beam-column center at x_s to provide a plane surface perpendicular to the laser beams of the laser distance sensors, (no. 10) in figure 4.1. Table 4.1 lists the relevant specifications of the test setup components.

Table 4.1.: Mechanical components of the experimental test setup

no.	qty.	description	type / material
1	1	beam-column with piezo-elastic supports	–
1a	1	beam-column	aluminum alloy 7075-T6
1b	4	strain gauge sensors	HBM® – *K-LY4-3-01-120-0*
1c	1	laser reflectors	polymer PA 2200
2	1	baseplate	Thorlabs®– *B90120A*
3	1	parallel guidance	Rexroth® – *KWD-035*
4	1	stiff frame structure	Rexroth® – strut profiles
5	1	shiftable mass	5 kg to 40 kg
6a	1	hinge	Rexroth® – swivel bearing
6b	1	stiff beam	Rexroth® – strut profiles
7a	1	linear axle	igus® – *SAW-1080*
7b	1	stepper motor	igus® – *NEMA23*
8a	1	releaseable mass	0 kg to 40 kg
8b	1	electromagnet	Magna-C® – *80055*
9	1	load cell	HMB® – *C2* (10 kN)
10	2	laser distance sensors	Micro-epsilon® – *ILD 1420-10*
piezo-elastic support			
A	1	lower piezo-elastic support	–
A1	1	connector	steel 1.4305
A2	1	retainer nut	steel 1.4305
A3	1	support housing	steel 1.4305
A4	1	spacer ring	steel 1.4310
A5	1	clamp ring	steel 1.4305
A6	2	membrane spring element	spring steel 1.1248
A7	2	piezoelectric stack actuators	PI Ceramic® – 2x *P-887.31*
A8	1	axial extension	hardened steel 1.2312
A9	2	helical disc springs	Röhrs® – *F-24628* (170 N/mm)
B	1	upper piezo-elastic support	–

4.1.2 Piezo-elastic supports

The piezo-elastic supports are designed to provide the elastic boundary conditions of the beam-column and to include the piezoelectric stack actuators to influence the lateral deflections, as motivated in the concept for the active buckling control in section 3.1. Figure 4.3 shows sectional views of the piezo-elastic support A.

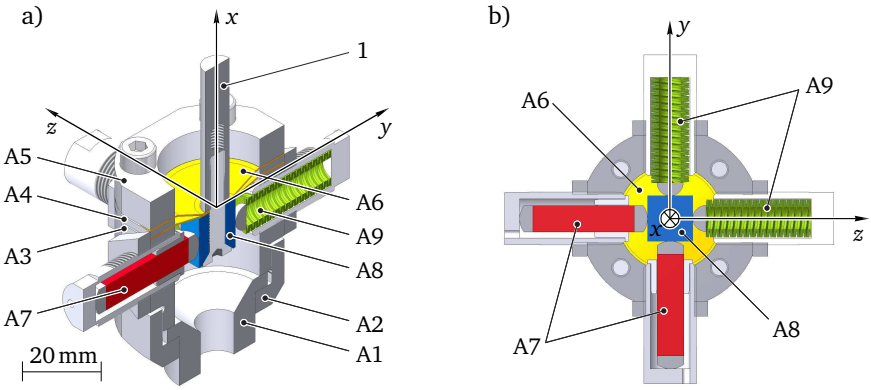

Figure 4.3.: Sectional views of piezo-elastic support A, a) 3D section through x-y-plane, b) 2D section bottom view through actuator-plane

The mechanical components that attach the beam-column with piezo-elastic supports, figure 4.2, to the test setup, figure 4.1, are the connector (no. A1) with retainer nut (no. A2), which fixate the support housing (no. A3). The connector is compatible to the lightweight truss structure in figure 1.1, [60], where the active beam-column system is planned to be integrated. The support housing (no. A3), spacer ring (no. A4) and the clamp ring (no. A5) clamp two differently shaped membrane spring elements (no. A6).

The two piezoelectric stack actuators (no. A7) in figure 4.3 exert lateral forces in y- and z-direction to the beam-column's axial extensions (no. A8) at a distance l_{ext} from the beam-column ends, as shown in figure 3.1. The piezoelectric stack actuators are mechanically prestressed by allocated helical disk springs (no. A9), to allow dynamic operation, [71]. Since only positive voltage may be applied to the piezoelectric stack actuators, they are electrically prestressed by constantly held 60 V to allow a symmetric operation of $-60\,\text{V} \leq V_{\text{pz},y/z}(t) \leq 60\,\text{V}$ of the piezoelectric stack actuators (3.25). Thus, positive and negative control inputs $\boldsymbol{u}(t)$ of the controller are possible while still fulfilling the voltage limitation of 120 V of the piezoelectric stack actuators, [71].

Figure 4.4 shows the photo of a single and the 2D section of the two assembled membrane spring elements (index ms) with sheet thickness h, radius r_{ms} and two different cone angles $\delta_{1/2}$, which are manufactured by a single point incremental forming process, [43]. The concave-shaped membrane spring elements bear the axial and lateral loads and allow rotations in any plane perpendicular to the beam-column's longitudinal x-axis, figure 4.3. Due to the high axial loads that act on the beam-column and, thus, the piezo-elastic supports, two membrane spring elements are used. By using two different cone angles $\delta_{1/2}$, it is possible to obtain relatively low values for the rotational stiffness $k_{\varphi_{y/z}}$ of the piezo-elastic supports, which is favorable for the electro-mechanical coupling of the piezoelectric stack actuators and the elastically supported beam-column, [100].

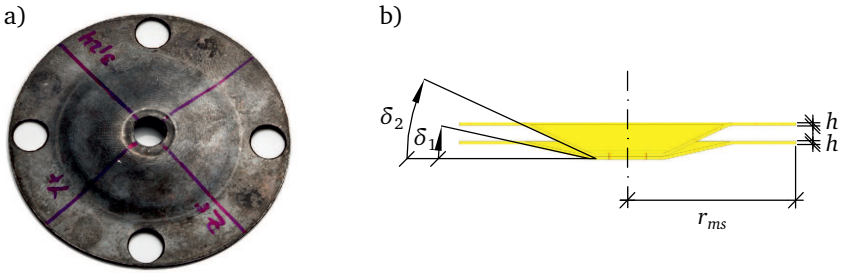

Figure 4.4.: Membrane spring elements in support A, a) real, experimental membrane spring element, b) 2D section of two different membrane spring elements with sheet thickness h, radius r_{ms} and cone angles $\delta_{1/2}$

The geometry of the membrane spring elements, i.e. h, r_{ms} and $\delta_{1/2}$, as well as the distance l_{ext} are the result of a numerical optimization of the combined stiffness of membrane spring elements and piezoelectric stack actuators to be close to fixed-fixed boundary conditions for the beam-column, as motivated in section 2.4, as well as the electro-mechanical coupling of the piezoelectric stack actuators and the elastically supported beam-column, [100].

4.1.3 Component variation for uncertainty quantification

As motivated in section 2.3.3, uncertainty in the form of imperfections in the material, geometry, loading or the support properties has a large effect on the passive buckling behavior of compressively loaded beam-column systems. Few studies have investigated uncertainty in the active buckling control. However,

knowledge of the uncertainty in the characteristic properties, such as maximum bearable axial loads for quasi-static, section 6.2.2, and lateral deflections for dynamic axial loads, section 6.3.2, of active beam-column systems is essential for the practical use of active buckling control in real applications.

The goal of this thesis is to quantify and evaluate uncertainty in passive buckling and active buckling control for the investigated beam-column system in figure 4.2. The approach of this thesis is to introduce variations in the characteristic properties for passive buckling and active buckling control by using different mechanical components in table 4.1, e.g. beam-columns and piezo-elastic supports, to include the effects of uncertainty in manufacturing, assembly and mounting of the beam-column system, as motivated in section 2.3.3.

As an example of uncertainty in manufacturing, the elastic properties of the piezo-elastic supports without piezoelectric stack actuators, which are represented by lateral stiffness $k_{y/z}$ and rotational stiffness $k_{\varphi_{y/z}}$ in figure 3.1, vary due to variations in the production process. A sample of ten nominally identical piezo-elastic supports without piezoelectric stack actuators with different support housings (no. A3), spacer rings (no. A4), clamp rings (no. A5) and membrane spring elements (no. A6) is investigated. Figure 4.5 shows experimental results of the lateral and rotational stiffness in y- and z-direction from static stiffness measurements, as performed in [37].

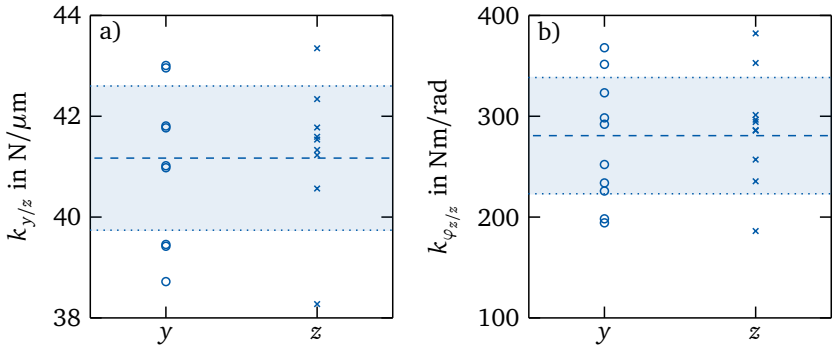

Figure 4.5.: Experimental variation in the measured stiffness parameters in y- and z-direction of ten different piezo-elastic supports without piezoelectric stack actuators with mean value μ_X (– –) and $2\sigma_X$ range ( ), a) lateral stiffness $k_{y/z}$, b) rotational stiffness $k_{\varphi_{y/z}}$

The variability in the sample of ten different piezo-elastic supports without piezoelectric stack actuators is indicated by the $2\sigma_X$ colored area with mean μ_X and standard deviation σ_X according to (2.12) given in table 4.2. The lateral stiffness $k_{y/z}$ is relatively high compared to the beam-column's flexural stiffness, as intended in the design process, so that the lateral displacements of the beam-column ends are very small. The rotational stiffness $k_{\varphi_{y/z}}$ is smaller, so that rotational displacements of the beam-column ends are possible. This is necessary for the piezoelectric stack actuators to influence the lateral dynamic behavior of the beam-column system, section 5.1.

Table 4.2.: Mean μ_X and standard deviation σ_X of the stiffness parameters for the ten different piezo-elastic supports without piezoelectric stack actuators

X	μ_X	σ_X	unit
$k_{y/z}$	41.17	1.43	N/μm
$k_{\varphi_{y/z}}$	280.77	57.64	Nm/rad

Due to the variation in the stiffness parameters, the use of different piezo-elastic supports without piezoelectric stack actuators is expected to yield variations in the lateral dynamic beam-column behavior, section 5.1.2, and the maximum bearable axial loads and lateral deflections due to quasi-static and dynamic axial loads, sections 6.2.2 and 6.3.2. In addition to different piezo-elastic supports without piezoelectric stack actuators, (A3), (A4), (A5) and (A6) in figure 4.3, the use of different beam-columns (no. 1) and piezoelectric stack actuators (no. A7), as given in table 4.3, is investigated.

Table 4.3.: Beam-column system components for exp. uncertainty quantification

no.	beam-columns	piezo-elastic supports	piezoelectric stack actuators
1	b1	AB1	p1
2	b2	AB2	p2
3	b3	AB3	
4	b4		
5	b5		
sum	5	3	2

For the experimental uncertainty quantification in this thesis, five identically instrumented beam-columns b, three combinations of lower and upper piezo-elastic supports without piezoelectric stack actuators AB and two different sets of piezoelectric stack actuators p are used.

Thus, a sample of $n = 5 \cdot 3 \cdot 2 = 30$ nominally identical beam-column systems is used to quantify and evaluate probabilistic uncertainty in passive buckling and active buckling control. The applied component variation combines the effects of uncertainty in manufacturing, assembly and mounting of the beam-column systems. Individual effects of manufacturing, assembly and mounting can not be separated by the approach. However, the combined effects are assumed to provide a realistic representation of the uncertainty in passive buckling and active buckling control of the experimental practical beam-column system.

4.2 Electrical test setup components

In this section, the electrical components of the experimental test setup, which are needed for the practical implementation of the active buckling control, chapter 6, are presented. As shown in figure 3.2, the voltages $V_{\mathrm{pz},y/z}(t)$ (3.25), which are applied to the piezoelectric stack actuators (no. A7) in figure 4.3, are used to control the beam-column's lateral deflections, which are represented by the bending strains $\varepsilon_{\mathrm{s},y/z}(t)$ (3.29) measured by the strain gauge sensors (no. 1b) in figure 4.2. Figure 4.6 shows a detailed depiction of the signal processing in the beam-column system used for active buckling control. The electrical components (EC) are summarized in table 4.4.

Table 4.4.: Electrical components of the experimental test setup

no.	qty.	description	type / material
EC1	1	real-time system	dSPACE® – *DS1103*
EC2	1	reconstruction filter	Eigner Messtechnik® – *AF08*
EC3	2	piezo amplifier	PI Ceramic® – *E-618.10G*
EC4	1	strain gauge amplifier	HBM® – *QuantumX MX410B*

The data acquisition and the controller implementation are performed with the real-time system (no. EC1) with a sampling frequency $f_{\mathrm{rt}} = 10\,\mathrm{kHz}$. The real-time system output voltages, the controller output $\boldsymbol{u}(t)$ (3.46), after DAC is filtered

and smoothed by the reconstruction filters (no. EC2) and amplified by the piezo amplifiers (no. EC3) before being applied to the piezoelectric stack actuators in the piezo-elastic supports A and B.

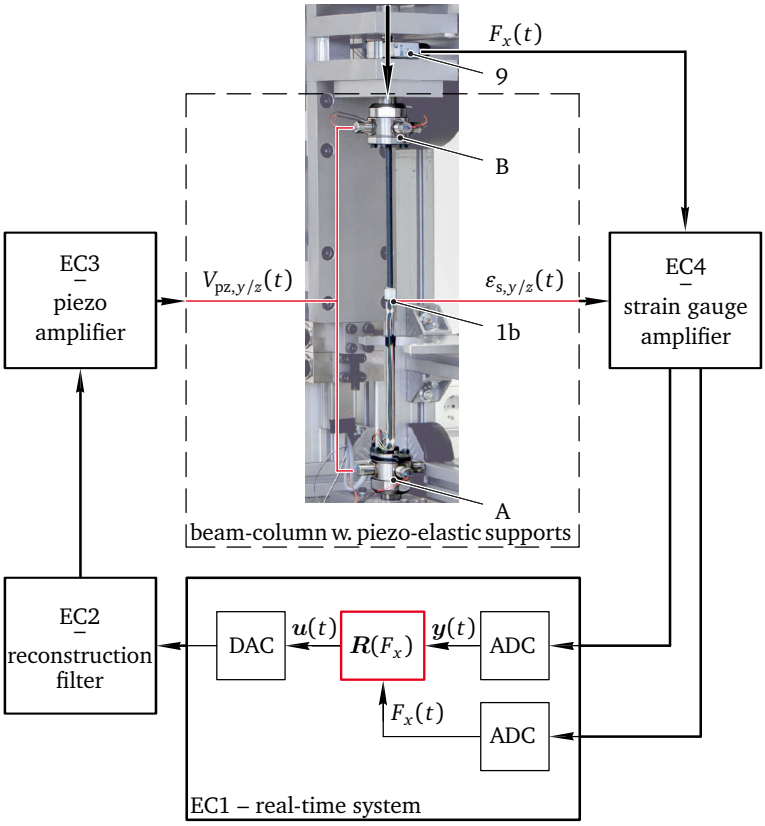

Figure 4.6.: Signal processing in the beam-column system for active buckling control

The sensor signals $\varepsilon_{s,y/z}(t)$ (3.29) from the strain gauge sensors (no. 1b) and $F_x(t)$ from the load cell (no. 9) are amplified and filtered prior to ADC by the strain gauge amplifier (no. EC4). For active buckling control, the dynamic LPV controller $\boldsymbol{R}(F_x)$, as derived in section 3.3 and tuned in section 5.3, is gain-scheduled in real-time by the measured axial load $F_x(t)$ via (3.77).

5 Beam-column dynamic behavior and controller tuning

The experimental test setup introduced in chapter 4 is used to perform experiments on passive buckling and active buckling control of the beam-column system subject to quasi-static and dynamic axial loads, sections 6.2 and 6.3. Knowledge of the axial load-dependent lateral dynamic behavior of the passive beam-column system is essential for the synthesis and tuning of the gain-scheduled $\mathscr{H}_\infty$ controller introduced in section 3.3. As result of the component variations introduced in section 4.1.3, the lateral dynamic behavior of the passive beam-column system is uncertain. The goal of this chapter is to describe the variations in the axial load-dependent lateral dynamic behavior of the passive beam-column system to obtain the parameters for a calibrated mean beam-column plant that represents the mean experimental beam-column system and to tune the gain-scheduled $\mathscr{H}_\infty$ controller for the mean beam-column plant.

This chapter opens with the investigation of the experimental axial load-dependent lateral dynamic behavior of the passive beam-column systems, section 5.1. Then, the experimental results are used to perform a model calibration of the beam-column plant from section 3.2.4 and to derive a mean beam-column plant, section 5.2. Finally, the gain-scheduled $\mathscr{H}_\infty$ controller, as introduced in section 3.3, is synthesized and tuned by adjusting the frequency-dependent in- and output weights for the experimental beam-column system by using the mean beam-column plant, section 5.3.

5.1 Experimental lateral dynamic behavior of the beam-column system

The lateral dynamic behavior of the beam-column system depends on the axial load $F_x(t)$, as shown in section 2.1.2. For the experimental characterization of the axial load-dependent lateral dynamic behavior without active buckling control, the passive beam-column system is loaded by static axial loads $F_x(t) = \text{const.}$ and is additionally excited by broadband white noise via the control inputs $u_{y/z}(t)$ (3.46) in y- and z-direction, which results in measurement outputs $y_{y/z}(t)$ (3.48) according

to figure 4.6. The experimental (index exp) beam-column plant transfer functions in y- and z-direction

$$P_{y,\mathrm{exp}}(F_x,\Omega)=\frac{y_y(F_x,\Omega)}{u_y(\Omega)} \qquad \text{and} \qquad P_{z,\mathrm{exp}}(F_x,\Omega)=\frac{y_z(F_x,\Omega)}{u_z(\Omega)}, \tag{5.1}$$

describe the relation of control inputs $u_{y/z}(\Omega)$ to measurement outputs $y_{y/z}(F_x,\Omega)$ for a harmonic excitation with angular frequency Ω, [30], similar to the transfer function (3.45) of the mathematical model. The experimental beam-column plant transfer functions $P_{y/z,\mathrm{exp}}(F_x,\Omega)$ (5.1) are estimated by the *tfestimate* algorithm in the MATLAB® *System Identification Toolbox*, [56]. The algorithm calculates the transfer functions from the averaged power spectral densities and cross power spectral densities of the excitation and measurement time signals, which are obtained by discrete FOURIER transformations, [16, 35].

In the following, first, the deterministic lateral dynamic behavior of a single beam-column system is presented in order to characterize the general axial load-dependency of the experimental transfer functions. Second, the uncertain lateral dynamic behavior of 30 nominally identical beam-column systems according to table 4.3 is presented in order to describe the uncertainty in the experimental transfer functions due to component variations.

5.1.1 Deterministic lateral dynamic behavior

This section presents the deterministic experimental lateral dynamic behavior of the beam-column system with beam-column (b2), piezo-elastic supports (AB1) and piezoelectric stack actuators (p1) according to table 4.3 subject to static axial loads $F_x(t)=\text{const}$. The particular beam-column system, which is further denoted as [b2-AB1-p1], is used as an arbitrary example to show the axial load-dependent lateral dynamic behavior of the experimental passive beam-column system. Qualitatively, the other investigated beam-column systems according to table 4.3 show the same dynamic behavior. However, they differ quantitatively, which is presented in section 5.1.2.

Figure 5.1 shows the experimental beam-column plant transfer functions $P_{y/z,\mathrm{exp}}(F_x,\Omega)$ (5.1) with amplitude response $|P_{y/z,\mathrm{exp}}(F_x,\Omega)|$ and phase response $\arg P_{y/z,\mathrm{exp}}(F_x,\Omega)$ in the frequency range $0\,\mathrm{Hz}\leq\Omega/2\pi\leq 1200\,\mathrm{Hz}$ and in y- and z-direction for the beam-column loaded with static axial loads $F_x=337\,\mathrm{N}$ and $2500\,\mathrm{N}$. The lower axial load $F_x=F_{x,\mathrm{l}}=337\,\mathrm{N}$ is the dead weight of the parallel

guidance, (no. 3) in figure 4.1, and $F_x = 2500\,\mathrm{N}$ is the maximum axial load to which the transfer function of the passive beam-column system can be measured for all investigated beam-column systems.

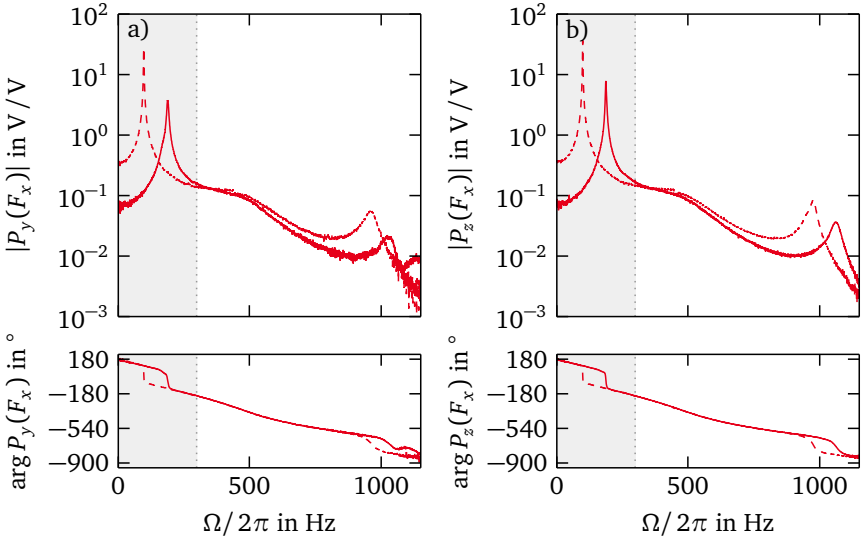

Figure 5.1.: Experimental beam-column plant transfer functions $P_{y/z,\mathrm{exp}}(337\,\mathrm{N}, \Omega)$(——) and $P_{y/z,\mathrm{exp}}(2500\,\mathrm{N}, \Omega)$ (– –) of the beam-column system [b2-AB1-p1] in a) y-direction and b) z-direction

The first and third lowly damped modes of vibration are visible as distinct peaks at the resonance frequencies in both directions and for both axial loads. As expected from figure 2.4b), both first and third resonance frequencies reduce for increasing axial load F_x. The second mode of vibration is not observable with the given sensor position, figure 3.6 and section 3.1.

At $\Omega/2\pi \approx 500\,\mathrm{Hz}$, the amplitude responses $|P_{y/z,\mathrm{exp}}(F_x)|$ bend downwards, which is the result of the low-pass filter in the strain gauge amplifier, section 4.2. Consequently, the amplitudes of the third mode of vibration are more than two orders smaller than of the first mode of vibration. The phase responses decline for increasing frequencies $\Omega/2\pi$, which is the result of the electrical components used for signal processing, sections 4.2 and 5.2.1. The jumps in the phase responses are attributed to the beam-column's first and third resonance frequencies.

In general, the amplitude and phase responses in y- and z-direction are similar, which shows that the experimental beam-column system in the experimental test setup is symmetric. Only the third mode of vibration in y-direction at $F_x = 337\,\mathrm{N}$ is influenced by test setup dynamics, which could not be reduced, seen by the anti-resonance at $\Omega/2\pi \approx 1050\,\mathrm{Hz}$. This influence remains constant and is not observed for higher axial loads $F_x \geq 1000\,\mathrm{N}$.

The chosen sensor position and the low-pass filtering lead to a large separation of the first mode of vibration from higher observable modes, both in frequency and amplitude. This is favorable for active buckling control, since the first mode of vibration is critical to buckling, section 2.1 and (2.2), and therefore can be focused by the controller. The relevant frequency range for the first resonance frequency $0\,\mathrm{Hz} \leq \Omega/2\pi \leq 300\,\mathrm{Hz}$ indicated by the shaded area in figure 5.1 is shown in detail in figure 5.2.

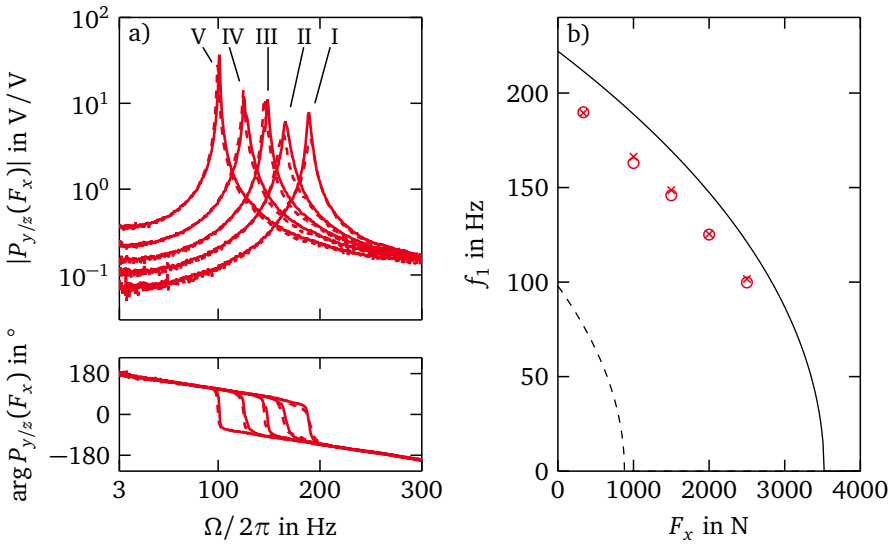

Figure 5.2.: Experimental lateral dynamic behavior of the beam-column system [b2-AB1-p1] for static axial loads $F_x = 337\,\mathrm{N}$ (I), $1000\,\mathrm{N}$ (II), $1500\,\mathrm{N}$ (III), $2000\,\mathrm{N}$ (IV) and $2500\,\mathrm{N}$ (V), a) beam-column plant transfer functions $P_{y/z,\mathrm{exp}}(F_x, \Omega)$ in y-direction (——) and z-direction (– –), b) experimental first resonance frequency $f_{1,y/z,\mathrm{exp}}(F_x)$ in y-direction (o) and z-direction (×), ideal pinned-pinned (– –) and fixed-fixed (——) boundary conditions as reference

Additional to figure 5.1, experimental beam-column plant transfer functions $P_{y/z,\mathrm{exp}}(F_x, \Omega)$ for axial loads $F_x = 1000\,\mathrm{N}$, $1500\,\mathrm{N}$ and $2000\,\mathrm{N}$ that lie between the curves from figure 5.1 are portrayed in figure 5.2a). The experimental first resonance frequencies $f_{1,y/z,\mathrm{exp}}(F_x)$ decrease for increasing static axial load F_x. Furthermore, the experimental static amplitude responses $|P_{y/z,\mathrm{exp}}(F_x, \Omega \to 0)|$ increase for increasing static axial loads F_x, which shows that the static lateral beam-column stiffness is reduced.

Figure 5.2b) also shows the decrease of the experimental first resonance frequencies $f_{1,y/z,\mathrm{exp}}(F_x)$ due to increasing static axial load between $337\,\mathrm{N} \leq F_x \leq 2500\,\mathrm{N}$. The displayed first resonance frequencies correspond to the maxima $\max(|P_{y/z,\mathrm{exp}}(F_x, \Omega)|) = |P_{y/z,\mathrm{exp}}(F_x, \Omega = 2\pi f_{1,y/z,\mathrm{exp}})|$ of the experimental amplitude responses and are similar in y- and z-direction. The dashed and solid black curves correspond to the numerical axial load-dependent first resonance frequencies of EULER cases II and IV with ideal pinned-pinned and fixed-fixed boundary conditions from Figure 2.4b), calculated with the geometric and material properties of the beam-column given in table 5.2. As intended, the boundary conditions of the beam-column system realized by the piezo-elastic supports, figure 4.3, are close to fixed-fixed boundary conditions, section 3.1. These result in the maximum possible critical buckling loads of the passive beam-column system, as shown in figure 2.2.

5.1.2 Uncertainty in the lateral dynamic behavior

This section presents the uncertain experimental lateral dynamic behavior of the 30 nominally identical beam-column systems from the variation of components in table 4.3. The component variations result in variations of the experimental beam-column plant transfer functions $P_{y/z,\mathrm{exp}}(F_x, \Omega)$. These may originate from variations in the component properties from manufacturing, as shown for the piezo-elastic support stiffness in figure 4.5 and table 4.2, but also from assembly and mounting of the beam-column with piezo-elastic supports in the experimental test setup, figure 4.1. However, the source of uncertainty is of minor importance for the uncertainty quantification in this thesis, as only the resulting variations in the lateral dynamic behavior of the beam-column systems is investigated.

Figure 5.3 shows the envelopes of the experimental beam-column plant transfer functions $P_{y/z,\mathrm{exp}}(F_x, \Omega)$, which represent the minimum and maximum amplitude and phase responses in the frequency range $0\,\mathrm{Hz} \leq \Omega/2\pi \leq 1200\,\mathrm{Hz}$ in y- and z-direction.

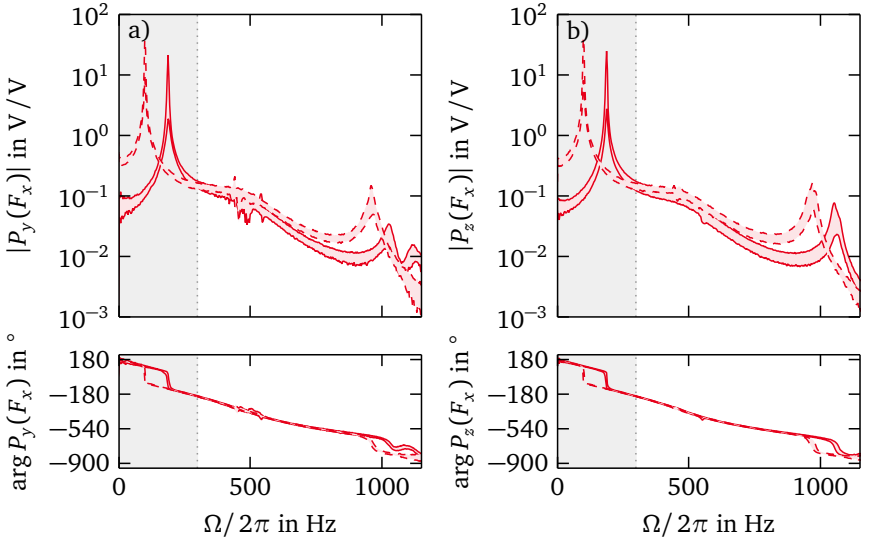

Figure 5.3.: Envelopes of 30 experimental beam-column plant transfer functions $P_{y/z,\mathrm{exp}}(337\,\mathrm{N},\Omega)$ (——) and $P_{y/z,\mathrm{exp}}(2500\,\mathrm{N},\Omega)$ (– –) in a) y-direction and b) z-direction

As in the deterministic case in figure 5.1, amplitude and phase responses in y- and z-direction are similar. In the frequency range $450\,\mathrm{Hz} \leq \Omega/2\pi \leq 550\,\mathrm{Hz}$, some small peaks in the amplitude responses are visible, which are attributed to the second mode of vibration being excited and measured due to imperfect actuator inputs or sensor positioning in single beam-column systems. The influence of the test setup dynamics at $\Omega/2\pi \approx 1050\,\mathrm{Hz}$ for $F_x = 337\,\mathrm{N}$ in y-direction is seen in all experimental beam-column plant transfer functions.

Figure 5.4 shows the envelopes of the experimental beam-column plant transfer functions $P_{y/z,\mathrm{exp}}(F_x,\Omega)$ and the experimental first resonance frequencies $f_{1,y/z,\mathrm{exp}}(F_x)$ in the frequency range $0\,\mathrm{Hz} \leq \Omega/2\pi \leq 300\,\mathrm{Hz}$ for axial loads $337\,\mathrm{N} \leq F_x \leq 2500\,\mathrm{N}$. Both, figures 5.4a) and b) show the variations of the lateral beam-column dynamics for the 30 investigated beam-column systems in y- and z-direction combined. The decrease of the experimental first resonance frequency $f_{1,y/z,\mathrm{exp}}(F_x)$ due to increasing static axial loads F_x is reproducible for all beam-column systems. Furthermore, the increase in the static amplitude responses $|P_{y/z,\mathrm{exp}}(F_x,\Omega \to 0)|$ for increasing static axial loads F_x, as seen in 5.2a) is also reproducible.

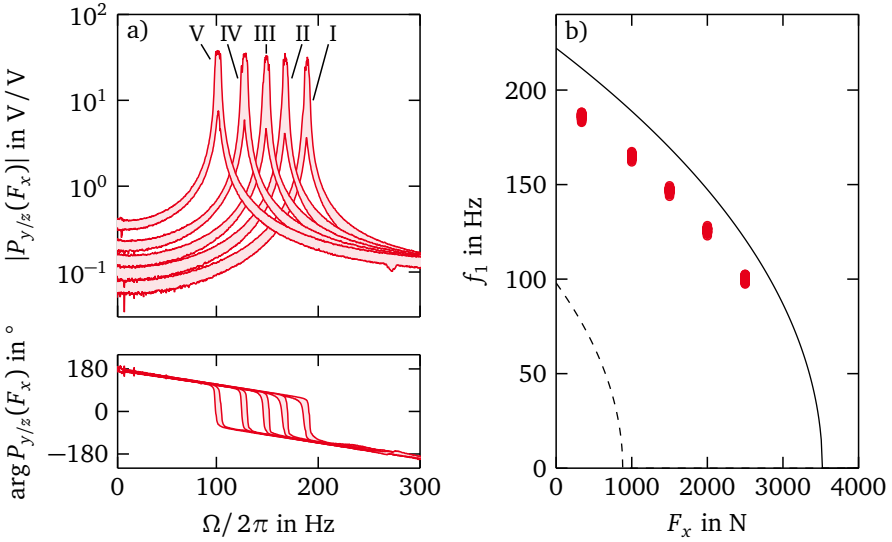

Figure 5.4.: Experimental lateral dynamic behavior of 30 beam-column systems for static axial loads $F_x = 337\,\mathrm{N}$ (I), $1000\,\mathrm{N}$ (II), $1500\,\mathrm{N}$ (III), $2000\,\mathrm{N}$ (IV) and $2500\,\mathrm{N}$ (V), a) envelopes of beam-column plant transfer functions $P_{y/z,\mathrm{exp}}(F_x, \Omega)$ in y and z-direction (——), b) experimental first resonance frequency $f_{1,y/z,\mathrm{exp}}(F_x)$ in y- and z-direction (o), ideal pinned-pinned (− −) and fixed-fixed (——) boundary conditions as reference

Table 5.1 shows the mean μ_X and standard deviation σ_X according to (2.12) of the experimental first resonance frequency $f_{1,y/z,\mathrm{exp}}(F_x)$ for different static axial loads F_x. The probability plots in figure A.1 in the appendix show that the assumption of normal distributions for the axial load-dependent experimental first resonance frequencies is justified.

Table 5.1.: Normal distribution fits of the experimental first resonance frequencies $f_{1,y/z,\mathrm{exp}}(F_x)$ of the 30 investigated beam-column systems

F_x/N	337	1000	1500	2000	2500
$\mu_{f_{1,y/z,\mathrm{exp}}}$/Hz	186.08	165.13	146.98	125.85	100.21
$\sigma_{f_{1,y/z,\mathrm{exp}}}$/Hz	1.17	1.11	1.09	1.07	1.23

As can be seen, the component variations according to table 4.3 result in variations of the experimental first resonance frequency, which is critical to buckling, section 2.1. The standard deviations are comparable for all investigated axial loads. Thus, the variations are assumed to result from the different beam-column systems and the axial load-dependency is assumed to be constant.

5.2 Calibration of the beam-column plant

This section presents the calibration of the mathematical beam-column plant with the experimental beam-column plant transfer functions from section 5.1. First, the model calibration procedure as well as the model parameters that are assumed to be fixed and that are calibrated are given in section 5.2.1. Then, the model calibration is performed for the deterministic beam-column system [b2-AB1-p1] in section 5.2.2 to show how the beam-column plant may be fitted to a single experimental beam-column system. Finally, the model calibration is performed for all 30 nominally identical experimental beam-column systems according to table 4.3 and the mean beam-column plant used for controller synthesis and tuning in section 5.3 is derived in section 5.2.3.

5.2.1 Model calibration procedure

For the model-based controller synthesis, it is important to appropriately describe the axial load-dependency of the experimental beam-column systems by the mathematical LPV beam-column plant $\boldsymbol{P}(F_x, s)$ (3.45). Therefore, the parameters of the beam-column plant are calibrated by comparison of the experimental lateral dynamic behavior according to (5.1) with the numerical (index num) beam-column plant transfer functions

$$P_{y,\mathrm{num}}(F_x, \Omega) = \frac{y_y(\Omega)}{u_y(\Omega)} \qquad \text{and} \qquad P_{z,\mathrm{num}}(F_x, \Omega) = \frac{y_z(\Omega)}{u_z(\Omega)}, \tag{5.2}$$

which are obtained from (3.45) for zero initial conditions and the conversion $s = j\,\Omega$, [30]. Most parameters of the beam-column plant (3.45), which were introduced in section 3.2, are assumed to be fixed for all investigated beam-column systems and are given in table 5.2. The properties of the beam-column material aluminum 7075-T6 are taken from [21].

Table 5.2.: Fixed parameters of the beam-column plant

property	symbol	value	unit
beam-column			
beam-column length	l_b	$400{\cdot}10^{-3}$	m
beam-column radius	r_b	$4{\cdot}10^{-3}$	m
beam-column density	ϱ_b	2850	$\mathrm{kg/m^3}$
beam-column Young's modulus	E_b	$71{\cdot}10^{9}$	$\mathrm{N/m^2}$
beam-column yield strength	$S_\mathrm{y,b}$	$505{\cdot}10^{6}$	$\mathrm{N/m^2}$
sensor position	x_s	$200{\cdot}10^{-3}$	m
modal damping ratio mode 3	ζ_3	$16{\cdot}10^{-3}$	–
piezo-elastic support			
axial extension width	d_ext	$12{\cdot}10^{-3}$	m
axial extension density	ϱ_ext	7810	$\mathrm{kg/m^3}$
axial extension Young's modulus	E_ext	$210{\cdot}10^{9}$	$\mathrm{N/m^2}$
electrical components			
real-time system sampling rate	f_rt	$10{\cdot}10^{3}$	Hz
real-time system time delay	T_rt	$4{\cdot}10^{-4}$	s
reconstruction filter cutoff frequency	f_rf	$4{\cdot}10^{3}$	Hz
piezo amplifier constant	c_pa	10	–
strain gauge amplifier cutoff frequency	f_sg	500	Hz
strain gauge amplifier constant	c_sg	$20{\cdot}10^{3}$	–

A reduced set of parameters that were shown to have a strong influence on the beam-column lateral dynamic behavior, [54], are calibrated to fit the numerical beam-column plant transfer functions (5.2) with the experimental beam-column plant transfer functions (5.1) presented in section 5.1. The set of calibrated parameters is

$$\boldsymbol{p}_{y/z} = \left[l_{\mathrm{ext},y/z},\, \zeta_{1,y/z},\, k_{y/z,\mathrm{e}},\, k_{y/z,\mathrm{g}},\, k_{\varphi_{y/z},\mathrm{e}},\, k_{\varphi_{y/z},\mathrm{g}},\, k_{\mathrm{pz},y/z},\, \theta_{y/z},\, k_{\mathrm{s},y/z},\, m_{\mathrm{s},y/z} \right]. \quad (5.3)$$

The parameters in $\boldsymbol{p}_{y/z}$ are the axial extension length $l_{\mathrm{ext},y/z}$, the modal damping ratio of the first mode of vibration $\zeta_{1,y/z}$, the elastic and geometric lateral support stiffness $k_{y/z,\mathrm{e/g}}$, the elastic and geometric rotational support stiffness $k_{\varphi_{y/z},\mathrm{e/g}}$, the piezoelectric stack actuator stiffness $k_{\mathrm{pz},y/z}$, the piezoelectric force constant $\theta_{y/z}$, and the sensor stiffness and mass $k_{\mathrm{s},y/z}$ and $m_{\mathrm{s},y/z}$. The stiffness of the elastic supports and the piezoelectric stack actuators are assumed to be identical in piezo-elastic supports A and B.

The parameters in (5.3) are independent in y- and z-direction and are varied to solve the least squares curve fitting problem

$$\min_{\boldsymbol{p}_{y/z}} \left(\sum_{i=1}^{5} \left|\left| P_{y/z,\mathrm{exp}}(F_{x,i},\Omega) - P_{y/z,\mathrm{num}}(F_{x,i},\Omega,\boldsymbol{p}_{y/z}) \right|\right|_2^2 \right) \tag{5.4}$$

with the experimental and numerical beam-column plant transfer functions $P_{y/z,\mathrm{exp}}(F_x,\Omega)$ (5.1) and $P_{y/z,\mathrm{num}}(F_x,\Omega)$ (5.2) for the five measured axial loads $F_x = 337\,\mathrm{N}$, $1000\,\mathrm{N}$, $1500\,\mathrm{N}$, $2000\,\mathrm{N}$ and $2500\,\mathrm{N}$. The model calibration is performed for all five measured axial loads F_x at once according to (5.4), so that the axial load-dependency is well captured by the model. The least squares curve fitting problem in (5.4) is solved by the *lsqnonlin* algorithm in the MATLAB® *Optimization Toolbox*, [62].

The goodness of fit between the experimental beam-column plant transfer function $P_{y/z,\mathrm{exp}}(F_x,\Omega)$ (5.1) and the numerical beam-column plant transfer function $P_{y/z,\mathrm{num}}(F_x,\Omega)$ (5.2) in y- and z-direction is quantified by the normalized root mean square error (NRMSE) for a given axial load F_x

$$\Delta_{y/z}(F_x) = 1 - \frac{\left|\left| P_{y/z,\mathrm{exp}}(F_x,\Omega) - P_{y/z,\mathrm{num}}(F_x,\Omega) \right|\right|}{\left|\left| P_{y/z,\mathrm{exp}}(F_x,\Omega) - \mathrm{mean}\left(P_{y/z,\mathrm{exp}}(F_x,\Omega)\right) \right|\right|}, \tag{5.5}$$

[56]. For $\Delta_{y/z}(F_x) = 1$, model and experiment fit exactly for the axial load F_x.

5.2.2 Deterministic model calibration

The model calibration according to (5.4) is performed for the beam-column system [b2-AB1-p1], which was discussed in section 5.1.1 and the numerical and experimental beam-column plant transfer functions are compared in the following. Figure 5.5 shows the experimental beam-column plant transfer functions $P_{y/z,\mathrm{exp}}(F_x,\Omega)$ (5.1) from figure 5.1 with the corresponding calibrated numerical beam-column plant transfer functions $P_{y/z,\mathrm{num}}(F_x,\Omega)$ (5.2). The y- and z-direction are calibrated separately and the model and the experiment show good agreement in the frequency range $0\,\mathrm{Hz} \leq \Omega/2\pi \leq 1200\,\mathrm{Hz}$. The influence of the test setup dynamics, as discussed in section 5.1.1, is not considered in the beam-column plant (3.45), which leads to the discrepancies of model and experiment for the third mode of vibration at $F_x = 337\,\mathrm{N}$ in y-direction. For higher axial loads, the test setup influence is no longer observed.

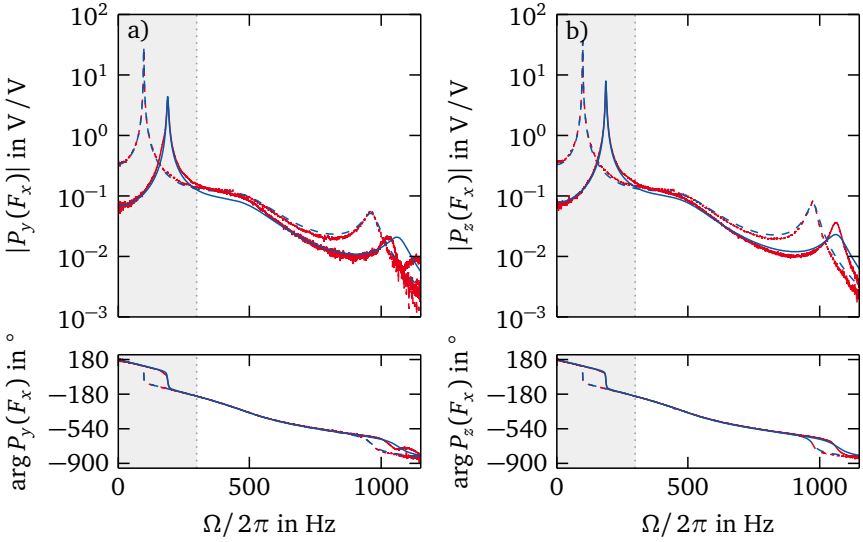

Figure 5.5.: Experimental and numerical beam-column plant transfer functions $P_{y/z,\mathrm{exp}}(337\,\mathrm{N},\Omega)$ (——), $P_{y/z,\mathrm{exp}}(2500\,\mathrm{N},\Omega)$ (– –), $P_{y/z,\mathrm{num}}(337\,\mathrm{N},\Omega)$ (——) and $P_{y/z,\mathrm{num}}(2500\,\mathrm{N},\Omega)$ (– –) in a) y-direction and b) z-direction

The calibrated parameter values of $\boldsymbol{p}_{y/z}$ (5.3) are given in table 5.3.

Table 5.3.: Calibrated parameter values of $\boldsymbol{p}_{y/z}$ for the beam-column system [b2-AB1-p1] in y- and z-direction

parameter	y	z	unit
$l_{\mathrm{ext},y/z}$	$7.77{\cdot}10^{-3}$	$7.75{\cdot}10^{-3}$	m
$\zeta_{1,y/z}$	$2.71{\cdot}10^{-3}$	$2.85{\cdot}10^{-3}$	–
$k_{y/z,\mathrm{e}}$	$21.70{\cdot}10^{6}$	$29.73{\cdot}10^{6}$	N/m
$k_{y/z,\mathrm{g}}$	$43.26{\cdot}10^{3}$	$58.48{\cdot}10^{3}$	1/m
$k_{\varphi_{y/z},\mathrm{e}}$	203.67	214.66	Nm/rad
$k_{\varphi_{y/z},\mathrm{g}}$	$104.75{\cdot}10^{-3}$	$99.93{\cdot}10^{-3}$	m/rad
$k_{\mathrm{pz},y/z}$	$20.12{\cdot}10^{6}$	$20.85{\cdot}10^{6}$	N/m
$\theta_{y/z}$	$187.87{\cdot}10^{-9}$	$180.53{\cdot}10^{-9}$	m/V
$k_{\mathrm{s},y/z}$	$1.85{\cdot}10^{3}$	$1.78{\cdot}10^{3}$	N/m
$m_{\mathrm{s},y/z}$	$3.55{\cdot}10^{-3}$	$3.54{\cdot}10^{-3}$	kg

The calibrated parameters are similar in y- and z-direction, which indicates that the experimental beam-column system is symmetric in the lateral directions. In order to also obtain a symmetric beam-column plant that can be used for controller synthesis, both lateral directions of the deterministic beam-column plant are assumed to be identical. For that, the mean of the calibrated parameter sets $\boldsymbol{p}_y$ and $\boldsymbol{p}_z$ from (5.3) is used to calculate the numerical beam-column plant transfer functions $P_{y/z,\mathrm{num}}(F_x, \Omega)$ (5.2) for both y- and z-direction. Figure 5.6 shows the resulting numerical beam-column plant transfer function $P_{\mathrm{num}}(F_x, \Omega)$ and the numerical first resonance frequency $f_{1,\mathrm{num}}(F_x)$ with the experimental results from figure 5.2 in the frequency range $0\,\mathrm{Hz} \leq \Omega/2\pi \leq 300\,\mathrm{Hz}$ for axial loads $337\,\mathrm{N} \leq F_x \leq 2500\,\mathrm{N}$.

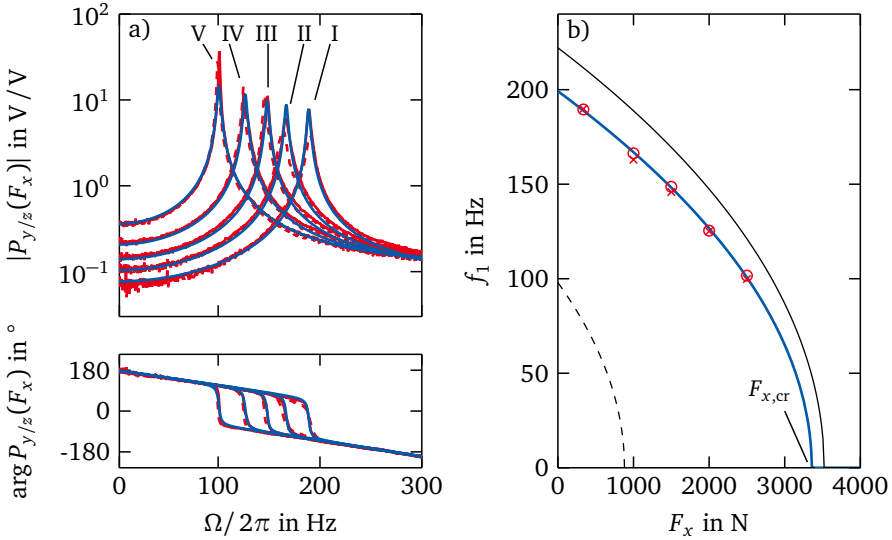

Figure 5.6.: Experimental and numerical beam-column dynamic behavior, a) beam-column plant transfer functions $P_{y,\mathrm{exp}}(F_x, \Omega)$ (——), $P_{z,\mathrm{exp}}(F_x, \Omega)$ (– –) and $P_{\mathrm{num}}(F_x, \Omega)$ (——) for $F_x = 337\,\mathrm{N}$ (I), $1000\,\mathrm{N}$ (II), $1500\,\mathrm{N}$ (III), $2000\,\mathrm{N}$ (IV) and $2500\,\mathrm{N}$ (V), b) experimental first resonance frequency $f_{1,y/z,\mathrm{exp}}(F_x)$ in y-direction (o) and z-direction (×) for $337\,\mathrm{N} \leq F_x \leq 2500\,\mathrm{N}$, numerical first resonance frequency $f_{1,\mathrm{num}}(F_x)$ for $0\,\mathrm{N} \leq F_x \leq 4000\,\mathrm{N}$ (——); ideal pinned-pinned (– –) and fixed-fixed (——) boundary conditions as reference

Amplitude and phase responses from model and experiment coincide well for the considered frequency range. Thus, the model adequately represents the axial load-dependency of the experimental beam-column system. The decrease of the experimental first resonance frequencies $f_{1,y/z,\mathrm{exp}}(F_x)$ due to increasing static axial loads F_x is well captured by the beam-column plant. The same is valid for the increase in the static amplitude responses $|P_{y/z}(F_x, \Omega \to 0)|$ for increasing static axial loads F_x.

The goodness of fit between model and experiment in figure 5.6 in the frequency range $0\,\mathrm{Hz} \leq \Omega/2\pi \leq 300\,\mathrm{Hz}$ is quantified by the NRMSE $\Delta_{y/z}(F_x)$ (5.5) given in table 5.4. The values of the NRMSE lie in the range of $0.50 \leq \Delta_{y/z}(F_x) \leq 0.78$ for all investigated axial loads. The deviations from the perfect fit $\Delta_{y/z}(F_x) = 1$ are explained by the fact that the calibration is simultaneously performed for all axial loads and that the numerical model is identical in y- and z-direction.

Table 5.4.: NRMSE values $\Delta_{y/z}(F_x)$ of experimental and numerical transfer functions after calibration for beam-column system [b2-AB1-p1]

F_x/N	337	1000	1500	2000	2500
Δ_y	0.53	0.78	0.58	0.72	0.59
Δ_z	0.50	0.75	0.53	0.63	0.63

The numerical first resonance frequency $f_{1,\mathrm{num}}(F_x)$ is shown in figure 5.6b) for axial loads $0\,\mathrm{N} \leq F_x \leq 4000\,\mathrm{N}$. It is calculated by solution of the eigenvalue problem for lateral beam-column vibrations in (3.22). The numerical first resonance frequency reaches zero for the critical buckling load $F_{x,\mathrm{cr}}$ obtained by solution of (3.21). For the beam-column system [b2-AB1-p1], the critical buckling load is $F_{x,\mathrm{cr}} = 3393.58\,\mathrm{N} = 0.96 \cdot F_{x,\text{E-IV}}$, which is close to the EULER case IV buckling load $F_{x,\text{E-IV}} = 3522.31\,\mathrm{N}$ obtained from (2.5) with the fixed geometric and material properties given in table 5.2.

The slenderness ratio λ (2.3) of the experimental beam-column system [b2-AB1-p1] can be calculated from the estimated critical buckling load to $\lambda = 102$, which is closer to the transition slenderness ratio $\lambda_{\mathrm{tr}} = 37$ according to (2.4). Thus, the beam-column system still exhibits elastic buckling, but can be considered as practical beam-column system, as motivated in section 2.4.

5.2.3 Model calibration considering uncertainty

This section presents the model calibration considering uncertainty in the experimental lateral dynamic behavior of the beam-column systems, which was discussed in section 5.1.2. The goal of this section is to obtain the parameters for a calibrated mean beam-column plant that gives the best representation of the axial load-dependent lateral dynamic behavior of all passive experimental beam-column systems. The derived mean beam-column plant is then used for the synthesis and tuning of the gain-scheduled $\mathscr{H}_\infty$ controller in section 5.3.

The deterministic model calibration according to (5.4) presented in section 5.2.2 is performed individually for the 30 nominally identical beam-column systems according to table 4.3. The resulting 30 parameter sets $\boldsymbol{p}_y$ and $\boldsymbol{p}_z$ (5.3), which are calibrated separately for y- and z-direction, are combined in one sample of 60 calibrated parameter sets. Figure 5.7 shows the normalized histograms of the 10 calibrated parameters X with fitted normal probability density functions (pdf) $p_\mathrm{N}(X)$ (2.11). The probability plots in figure A.2 in the appendix show that the assumption of normal distributions for the calibrated parameters is justified. The corresponding means μ_X and standard deviations σ_X (2.12) are summarized in table 5.5.

Table 5.5.: Normal distribution fits for the $2 \cdot 30$ calibrated parameter sets $\boldsymbol{p}_y$ and $\boldsymbol{p}_z$

parameter	μ_X	σ_X	unit
$l_{\mathrm{ext},y/z}$	$8.12{\cdot}10^{-3}$	$0.37{\cdot}10^{-3}$	m
$\zeta_{1,y/z}$	$3.98{\cdot}10^{-3}$	$1.36{\cdot}10^{-3}$	–
$k_{y/z,\mathrm{e}}$	$44.97{\cdot}10^{6}$	$15.34{\cdot}10^{6}$	N/m
$k_{y/z,\mathrm{g}}$	$69.76{\cdot}10^{3}$	$24.08{\cdot}10^{3}$	1/m
$k_{\varphi_{y/z},\mathrm{e}}$	224.61	42.41	Nm/rad
$k_{\varphi_{y/z},\mathrm{g}}$	$78.60{\cdot}10^{-3}$	$35.75{\cdot}10^{-3}$	m/rad
$k_{\mathrm{pz},y/z}$	$19.16{\cdot}10^{6}$	$1.24{\cdot}10^{6}$	N/m
$\theta_{y/z}$	$177.96{\cdot}10^{-9}$	$8.28{\cdot}10^{-9}$	m/V
$k_{\mathrm{s},y/z}$	$1.70{\cdot}10^{3}$	$0.27{\cdot}10^{3}$	N/m
$m_{\mathrm{s},y/z}$	$3.62{\cdot}10^{-3}$	$0.39{\cdot}10^{-3}$	kg

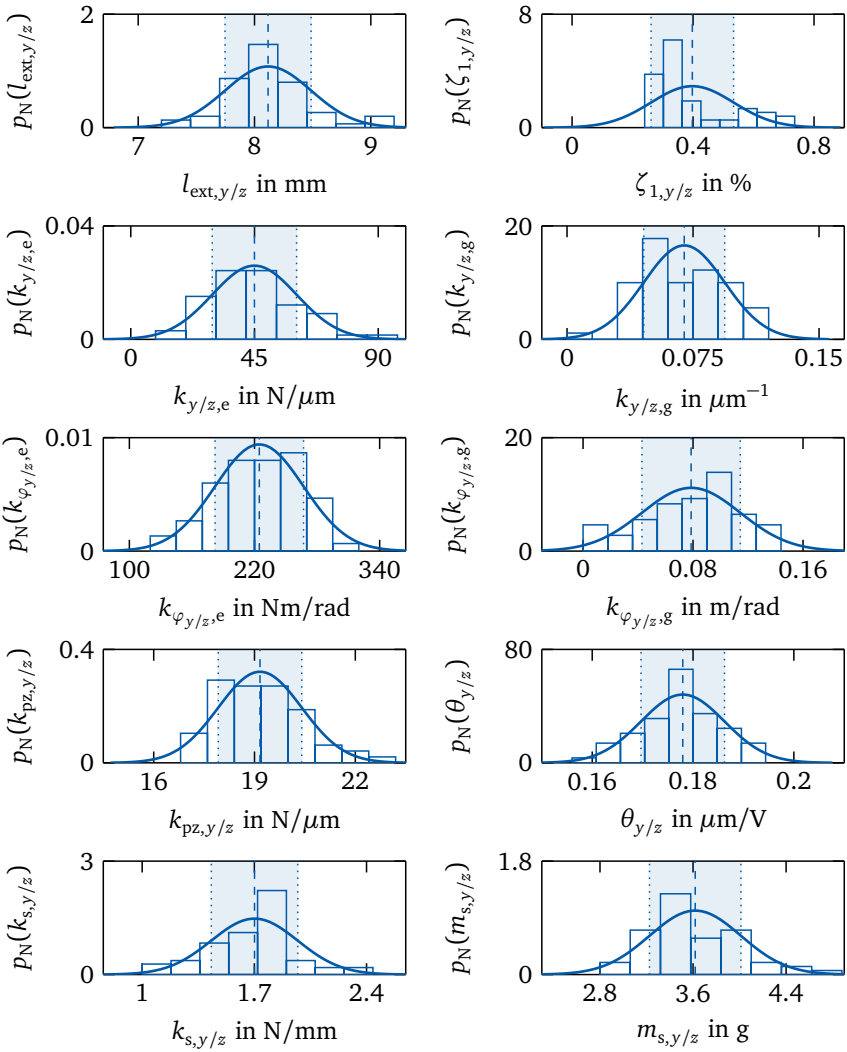

Figure 5.7.: Normalized histograms of the $2 \cdot 30$ calibrated parameter sets $\boldsymbol{p}_y$ and $\boldsymbol{p}_z$ and normal distribution fits $p_N(X)$ with mean μ_X (– –) and $2\sigma_X$ range ( )

The numerical beam-column plant transfer functions (5.2) with the means of the calibrated parameters in table 5.5 are denoted as the mean beam-column

plant transfer function $\overline{P}_{\mathrm{num}}(F_x, \Omega)$, which represent both y- and z-direction. Figure 5.8 shows the envelopes of the experimental beam-column plant transfer functions $P_{y/z,\mathrm{exp}}(F_x, \Omega)$ from figure 5.3 and the mean beam-column plant transfer function $\overline{P}_{\mathrm{num}}(F_x, \Omega)$, which lies within the experimental envelopes except for the discrepancies of the third mode of vibration at $F_x = 337\,\mathrm{N}$ in y-direction, as discussed previously. This shows that the mean beam-column model describes the lateral dynamic behavior of the experimental passive beam-column systems reasonably well for the first and third modes of vibration in the frequency range $0\,\mathrm{Hz} \leq \Omega/2\pi \leq 1200\,\mathrm{Hz}$.

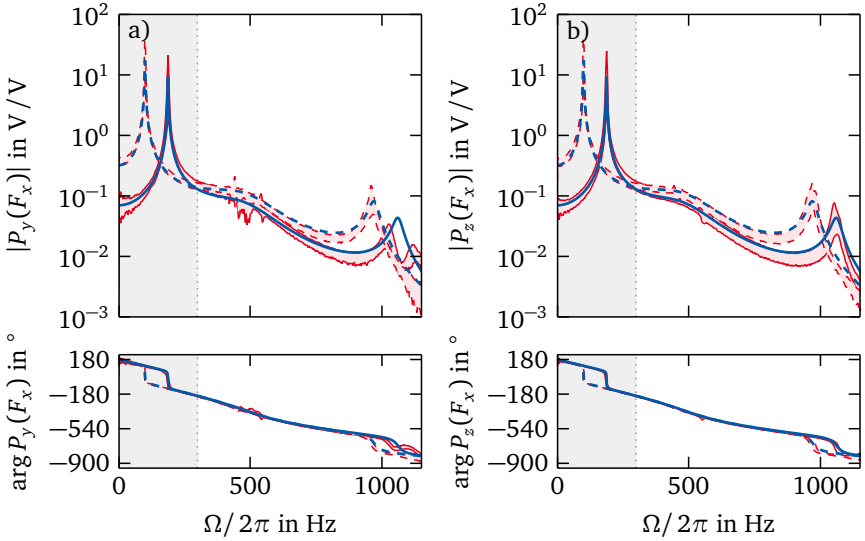

Figure 5.8.: Envelopes of 30 experimental beam-column plant transfer functions $P_{y/z,\mathrm{exp}}(337\,\mathrm{N}, \Omega)$ (——) and $P_{y/z,\mathrm{exp}}(2500\,\mathrm{N}, \Omega)$ (– –), mean beam-column plant $\overline{P}_{\mathrm{num}}(337\,\mathrm{N}, \Omega)$ (——) and $\overline{P}_{\mathrm{num}}(2500\,\mathrm{N}, \Omega)$ (– –) in a) y-direction and b) z-direction

Figure 5.9 shows the envelopes of the experimental beam-column plant transfer functions $P_{y/z,\mathrm{exp}}(F_x, \Omega)$ in the frequency range $0\,\mathrm{Hz} \leq \Omega/2\pi \leq 300\,\mathrm{Hz}$ and the experimental first resonance frequencies $f_{1,y/z,\mathrm{exp}}(F_x)$ from figure 5.4 together with the mean beam-column plant transfer function $\overline{P}_{\mathrm{num}}(F_x, \Omega)$ and the mean first resonance frequency $\overline{f}_{1,\mathrm{num}}(F_x)$.

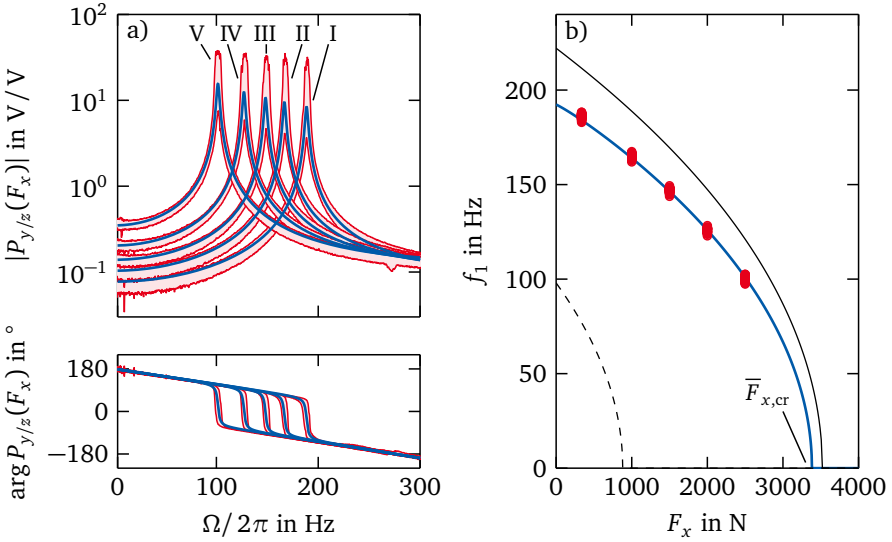

Figure 5.9.: Experimental lateral dynamic behavior of 30 beam-column systems for static axial loads $F_x = 337\,\mathrm{N}$ (I), $1000\,\mathrm{N}$ (II), $1500\,\mathrm{N}$ (III), $2000\,\mathrm{N}$ (IV) and $2500\,\mathrm{N}$ (V) and mean beam-column plant, a) envelopes of beam-column plant transfer functions $P_{y/z,\mathrm{exp}}(F_x,\Omega)$ in y and z-direction (——) and mean beam-column plant $\overline{P}_{\mathrm{num}}(F_x,\Omega)$ (——), b) first resonance frequency $f_1(F_x)$ in y- and z-direction (o), mean beam-column plant (——); ideal pinned-pinned (– –) and fixed-fixed (——) boundary conditions

For the investigated axial loads F_x, the axial load-dependent mean first resonance frequency $\overline{f}_{1,\mathrm{num}}(F_x)$ and the static amplitude response of the mean beam-column plant transfer function $\overline{P}_{\mathrm{num}}(F_x,\Omega=0)$ lie within the experimental envelopes of the uncertain experimental beam-column plant transfer functions, figure 5.4. Because of the good agreement, the mean beam-column plant is expected to adequately represent the mean axial load-dependent lateral dynamic behavior of the 30 nominally identical experimental beam-column systems. Thus, it is used for the controller synthesis described in section 3.3.4. The mean critical buckling load of the mean beam-column plant according to (3.21) is $\overline{F}_{x,\mathrm{cr}} = 3381.01\,\mathrm{N} = 0.96 \cdot F_{x,\mathrm{E\text{-}IV}}$. The mean slenderness ratio (2.3) of all experimental beam-column systems is calculated from the mean critical buckling load to $\overline{\lambda} = 102$ and, thus, does not change compared to the deterministic beam-column system in section 5.2.2.

5.3 Controller tuning

The mean beam-column transfer function $\overline{P}_{\text{num}}(F_x, \Omega)$ derived in the previous section characterizes the mean beam-column lateral dynamic behavior of the 30 investigated beam-column systems in y- and z-direction, section 4.1.3. Thus, it is used for synthesis, section 3.3, and tuning of the gain-scheduled $\mathscr{H}_\infty$ control described in this section. First, the parameters of the frequency-dependent controller weights introduced in section 3.3.3 are presented in section 5.3.1. Second, the controller performance is numerically verified by analyzing the lateral dynamic behavior of the closed-loop beam-column plant in section 5.3.2.

5.3.1 Controller weight selection

As presented in section 3.3.3, the frequency-dependent input and output weights (3.72) to (3.75) in figure 3.10 are used to shape the transfer behavior of the closed-loop plant $\boldsymbol{P}_{\text{cl}}(F_x, s)$ (3.58). The parameters of the frequency-dependent weights are tuned to achieve satisfactory closed-loop control performance. This is done iteratively by manually choosing different parameter values, synthesizing the controller and analyzing the resulting closed-loop plant, [58, 97]. The parameter values of the input and output weights (3.72) to (3.75) are summarized in table 5.6 and the corresponding transfer functions are displayed in figure A.5 in the appendix.

Table 5.6.: Parameters of frequency-dependent input and output weights

weight	parameters	order
$W_{\boldsymbol{d}}$	$a_{\boldsymbol{d}} = 1{\cdot}10^{-4}\,\text{rad/s}$, $b_{\boldsymbol{d}} = 2.2{\cdot}10^{-4}\,\text{Nm rad/s}$	1
$W_{\boldsymbol{n}}$	$c_{\boldsymbol{n}} = 1{\cdot}10^{-3}\,\text{V}$	0
$W_{\boldsymbol{y}}$	$c_{\boldsymbol{y}} = 0.2\,/\text{V}$, $\zeta_{\boldsymbol{y}} = 0.1$, $\omega_{\boldsymbol{y}} = 479 \cdot 2\pi\,\text{rad/s}$	2
$W_{\boldsymbol{u}}$	$a_{\boldsymbol{u}} = 20$, $b_{\boldsymbol{u}} = 1{\cdot}10^{-2}$, $c_{\boldsymbol{u}} = 1\,\text{V}$, $\omega_{\boldsymbol{u}} = 5000 \cdot 2\pi\,\text{rad/s}$	4

For each transfer path $\boldsymbol{w} \rightarrow \boldsymbol{z}$ from the exogenous inputs $\boldsymbol{w}(s)$ (3.60) to the performance outputs $\boldsymbol{z}(s)$ (3.64) in figure 3.10, the input and output weights define upper bounds $\Gamma_{\boldsymbol{w}\rightarrow\boldsymbol{z}}(s)$, which limit and shape the amplitude responses of the closed-loop plant $\boldsymbol{P}_{\text{cl}}(F_x, s)$ (3.58). For the transfer paths from disturbance end

moments $\boldsymbol{d}(s)$ and measurement noise $\boldsymbol{n}(s)$ to the performance outputs $\boldsymbol{y}_\mathrm{t}(s)$ and $\boldsymbol{u}_\mathrm{t}(s)$, the upper bounds are

$$\begin{aligned} \Gamma_{\boldsymbol{d}\to\boldsymbol{y}_\mathrm{t}}(s) &= \frac{1}{|W_{\boldsymbol{d}}(s)\,W_{\boldsymbol{y}}(s)|}, & \Gamma_{\boldsymbol{n}\to\boldsymbol{y}_\mathrm{t}}(s) &= \frac{1}{|W_{\boldsymbol{n}}(s)\,W_{\boldsymbol{y}}(s)|}, \\ \Gamma_{\boldsymbol{d}\to\boldsymbol{u}_\mathrm{t}}(s) &= \frac{1}{|W_{\boldsymbol{d}}(s)\,W_{\boldsymbol{u}}(s)|} \quad \text{and} & \Gamma_{\boldsymbol{n}\to\boldsymbol{u}_\mathrm{t}}(s) &= \frac{1}{|W_{\boldsymbol{n}}(s)\,W_{\boldsymbol{u}}(s)|}. \end{aligned} \tag{5.6}$$

5.3.2 Numerical verification of the controller performance

The performance of the gain-scheduled $\mathscr{H}_\infty$ buckling control is verified numerically prior to the implementation in the experimental test setup in chapter 6 by comparing the passive open-loop and active closed-loop beam-column plant dynamic behavior, [8, 85, 97].

The gain-scheduled $\mathscr{H}_\infty$ controller is synthesized for the weighted closed-loop plant $\boldsymbol{P}_{\mathrm{cl,w}}(F_x,s)$ (3.70) with the fixed and calibrated model parameters in tables 5.2 and 5.5 of the mean beam-column plant as well as the weight parameters in table 5.6. For that, the BRL (3.80) is solved for the vertices of the weighted closed-loop plant $\boldsymbol{P}_{\mathrm{cl,w}}(F_{x,\mathrm{l}})$ and $\boldsymbol{P}_{\mathrm{cl,w}}(F_{x,\mathrm{u}})$ for the subcritical lower axial load $F_{x,\mathrm{l}} = 337\,\mathrm{N}$ and supercritical upper axial load $F_{x,\mathrm{u}} = 3600\,\mathrm{N}$, which exceeds the mean critical buckling load $\overline{F}_{x,\mathrm{cr}} = 3381.01\,\mathrm{N}$ of the mean beam-column plant, section 5.2.3.

Figure 5.10 shows amplitude responses of the open-loop plant $\boldsymbol{P}_{\mathrm{ol}}(F_x,s)$ (3.66), the closed-loop plant $\boldsymbol{P}_{\mathrm{cl}}(F_x,s)$ (3.58) and the upper bounds $\Gamma_{\boldsymbol{w}\to\boldsymbol{z}}(s)$ (5.6) for zero initial conditions and the conversion $s = j\,\Omega$ and axial loads $337\,\mathrm{N} \le F_x \le 3600\,\mathrm{N}$.

The open-loop amplitude responses $|\boldsymbol{P}_{\mathrm{ol}}(F_x,\Omega)|$ only exist for transfer path $\boldsymbol{d} \to \boldsymbol{y}_\mathrm{t}$ from the disturbance end moments to the performance measurement output, figure 5.10a). As seen in section 5.2, the resonance frequencies of the open-loop amplitude responses $\boldsymbol{P}_{\mathrm{ol}}(F_x,\Omega)$ decrease for increasing axial load F_x and the static responses $|\boldsymbol{P}_{d\to y_\mathrm{t},\mathrm{ol}}(F_x,\Omega)|$. For the mean critical buckling load $F_x = \overline{F}_{x,\mathrm{cr}} = 3381.01\,\mathrm{N}$, the resonance frequency reduces to zero and the static amplitude response $|\boldsymbol{P}_{d\to y_\mathrm{t},\mathrm{ol}}(\overline{F}_{x,\mathrm{cr}},\Omega\to 0)| \to \infty$ grows infinitely, figure 5.10a). For supercritical axial loads $F_x \ge \overline{F}_{x,\mathrm{cr}}$, the open-loop plant $\boldsymbol{P}_{\mathrm{ol}}(F_x,s)$ (3.66) becomes instable and, therefore, is not displayed.

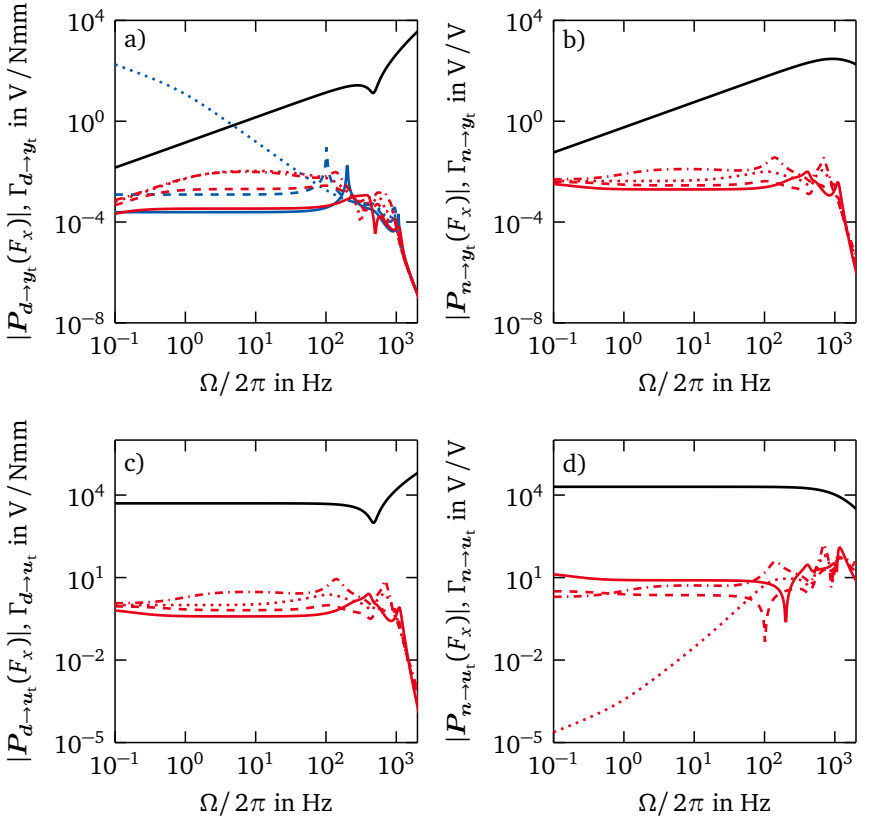

Figure 5.10.: Amplitude responses of open- (——) and closed-loop plant (——) $|\boldsymbol{P}_{w\to z}(F_x,\Omega)|$ and upper bounds $\Gamma_{w\to z}(\Omega)$ (——) for axial loads $F_x = 337\,\mathrm{N}$ (——), $F_x = 2500\,\mathrm{N}$ (– –), $F_x = F_{x,\mathrm{cr}}$ (·---·) and $F_x = 3600\,\mathrm{N}$ (–·– only closed-loop), transfer paths: a) $\boldsymbol{d}\to\boldsymbol{y}_\mathrm{t}$, b) $\boldsymbol{n}\to\boldsymbol{y}_\mathrm{t}$, c) $\boldsymbol{d}\to\boldsymbol{u}_\mathrm{t}$, d) $\boldsymbol{n}\to\boldsymbol{u}_\mathrm{t}$

The closed-loop plant $\boldsymbol{P}_\mathrm{cl}(F_x,s)$ (3.58) is quadratically stable for the entire operation range $F_{x,\mathrm{l}} \le F_x \le F_{x,\mathrm{u}}$ by solution of the bounded real lemma (3.80) and the induced $\mathscr{L}_2$-norm of the weighted closed-loop plant in (3.79) is smaller than $\gamma = 0.51$. Thus, none of the closed-loop amplitude responses in figure 5.10a)–d) violates the upper bounds $\Gamma_{\boldsymbol{w}\to\boldsymbol{z}}(s)$.

As intended by the weights on the performance measurement output $W_{\boldsymbol{y}}(s)$ (3.74), there are no large closed-loop amplitudes in the frequency range $450\,\text{Hz} \leq \Omega/2\pi \leq 550\,\text{Hz}$ so that the controller does not excite the second mode of vibration, figure 5.3. Furthermore, the resonance amplitudes for the shown axial loads F_x are reduced resulting in a reduction of lateral vibrations in the first lateral mode of vibration. For low frequencies $\Omega/2\pi \leq 1\,\text{Hz}$, the closed-loop amplitude responses in figure 5.10a) decrease as a result of the integral action in (3.72). The closed-loop static amplitude responses $|\boldsymbol{P}_{d\to y_\text{t},\text{cl}}(F_x, \Omega \to 0)|$ are reduced significantly compared to the static open-loop responses $|\boldsymbol{P}_{d\to y_\text{t},\text{ol}}(F_x, \Omega = 0)|$, figure 5.11.

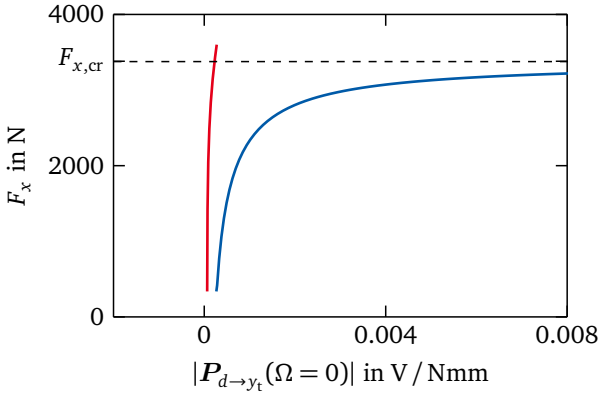

Figure 5.11.: Static amplitude response $|\boldsymbol{P}_{d\to y_\text{t}}(\Omega = 0)|$ versus axial load F_x for open-loop plant (——) and closed-loop plant (——)

For the critical buckling load $F_x = \overline{F}_{x,\text{cr}} = 3381.01\,\text{N}$, the closed-loop system is stable and the static response $|\boldsymbol{P}_{d\to y_\text{t},\text{ol}}(\overline{F}_{x,\text{cr}}, \Omega \to 0)|$ is finite. For axial loads exceeding $\overline{F}_{x,\text{cr}} \leq F_x \leq F_{x,\text{u}}$, the closed-loop plant remains stable. Furthermore, the static amplitude response slightly increases due to the approximated integrator in (3.72), which does not achieve exact zero lateral deflections.

Based on the numerical verification of controller performance of the axial load-dependent closed-loop beam-column plant, the gain-scheduled $\mathscr{H}_\infty$ controller tuned according to table 5.6 may stabilize the active beam-column system up to supercritical axial loads of up to $F_{x,\text{u}} = 3600\,\text{N}$. The experimental results for the active buckling control with the presented controller are presented in chapter 6.

6 Experimental results of passive buckling and active buckling control

This chapter presents the experimental results of passive buckling and active buckling control for the experimental beam-column systems introduced in section 4.1. First, the experimental procedure, the investigated load cases with quasi-static and dynamic axial loads and the characteristic quantities to describe passive buckling and active buckling control are introduced in section 6.1. Then, the experimental results for the beam-column systems subject to quasi-static axial loads, section 6.2, and dynamic axial loads, section 6.3, are examined and compared for the passive and active beam-column systems. Finally, the results of the experimental quantification and evaluation of uncertainty in the maximum bearable axial loads and lateral deflections are summarized and discussed in section 6.4.

6.1 Experimental procedure

The experiments for passive buckling and active buckling control are conducted on the experimental test setup shown in figure 4.1 with the 30 nominally identical beam-column systems according to table 4.3. The component variations introduced in section 4.1.3 are used to obtain a realistic representation of the uncertainty in passive buckling and active buckling control of the experimental practical beam-column systems. Passive buckling is investigated on the beam-column systems without the gain-scheduled $\mathscr{H}_\infty$ controller from section 3.3, which are denoted as passive beam-column systems. Active buckling control is investigated on the beam-column systems with the gain-scheduled $\mathscr{H}_\infty$ controller from sections 3.3 and 5.3, which are denoted as active beam-column systems.

The experimental beam-column systems exhibit real buckling behavior with increasing lateral deflections for increasing axial loads, which is shown for the beam-column center deflection in figure 2.3. The lateral beam-column center deflection in the experiment is approximated by the modal displacements $q_{1,y/z}(t)$ (3.32) of the first mode of vibration in y- and z-direction calculated by

$$\begin{bmatrix} q_{1,y}(t) \\ q_{1,z}(t) \end{bmatrix} \approx \frac{1}{c_{\mathrm{sg}}} \left(\boldsymbol{C}_{\boldsymbol{y},0} \begin{bmatrix} \widehat{\boldsymbol{r}}_{1,y}(F_{x,\mathrm{cr}}) \\ \widehat{\boldsymbol{r}}_{1,z}(F_{x,\mathrm{cr}}) \end{bmatrix}^{T} \right)^{-1} \begin{bmatrix} y_y(t) \\ y_z(t) \end{bmatrix}. \tag{6.1}$$

In (6.1), $y_{y/z}(t)$ are the measurement outputs from (3.48) and c_{sg} is the strain gauge amplifier constant from (3.52). The inverted $[2 \times 2]$ matrix in (6.1) is the modified modal output matrix with only the first eigenvectors $\boldsymbol{r}_{1,y/z}$ in y- and z-direction in (3.39). The absolute modal displacement is given by

$$q_1(t) = \sqrt{q_{1,y}^2(t) + q_{1,z}^2(t)}. \tag{6.2}$$

The passive and active beam-column systems are loaded by slowly increasing quasi-static axial loads $F_x(t) \approx$ const. and step-shaped dynamic axial loads $F_x(t) \neq$ const., which are measured in real-time by the load cell (no. 9) in figure 4.1. Both load cases are introduced in the following.

Quasi-static axial load

As introduced in section 4.1.1, the slowly increasing quasi-static axial loads $F_x(t) \approx$ const. are generated with the experimental test setup by shifting the mass (no. 5) in figure 4.1 via a linear axle (no. 7a) operated by a stepper motor (no. 7b). Thus, quasi-static axial loads between $337\,\mathrm{N} \leq F_x(t) \leq 5000\,\mathrm{N}$ are realizable. Figure 6.1 shows the quasi-static axial load $F_x(t)$ plotted versus time t used in the experiments of passive buckling and active buckling control for a single experiment, figure 6.1a), and for the $2 \cdot 30 = 60$ passive and active beam-column systems according to table 4.3, figure 6.1b).

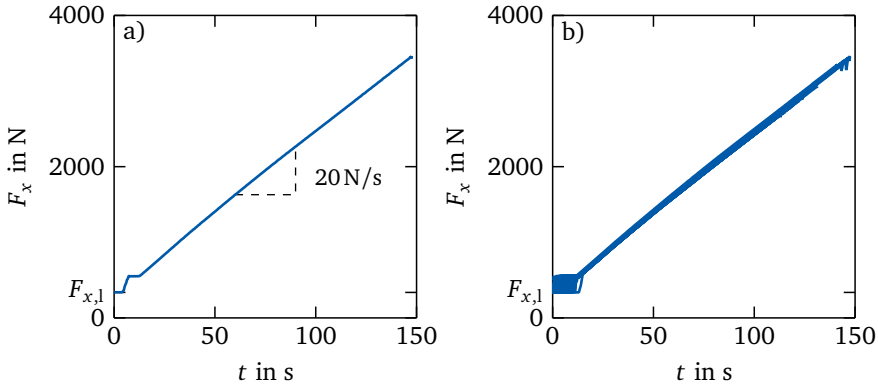

Figure 6.1.: Experimental quasi-static axial load F_x versus time t with slope $20\,\mathrm{N/s}$, a) single experiment, b) 60 experiments

The initial axial load $F_{x,\mathrm{l}} = 337\,\mathrm{N}$ is the dead weight of the parallel guidance (no. 3) in figure 4.1. In the axial load range $337\,\mathrm{N} \leq F_x(t) \leq 550\,\mathrm{N}$, the hinged beam (no. 6a) is manually lowered until the beam-column system fully supports the weight. Then, the axial load $F_x(t)$ increases by operation of the stepper motor (no. 7b) with a slope of approximately $20\,\mathrm{N/s}$. The 30 different beam-column systems are loaded up to the passive and active maximum bearable axial loads

$$F_{x,\mathrm{max,p/a}} = F_x(q_{1,\mathrm{max}}), \tag{6.3}$$

which are the characteristic properties to describe the quasi-static buckling behavior of the passive and active beam-column systems, as shown in figure 2.3. At $F_{x,\mathrm{max,p/a}}$, the maximum admissible modal displacement $q_{1,\mathrm{max}} = 0.5\,\mathrm{mm}$ according to (6.2) is reached, which is chosen to avoid plastic deformation of the beam-column.

Buckling due to the slowly increasing quasi-static axial loads $F_x(t)$ can be well controlled, since the axial load increase is stopped as soon as the maximum absolute modal deflection $q_{1,\mathrm{max}}$ is reached. This way, the beam-columns do not deform plastically, so that all passive and active beam-column systems according to the component variation, table 4.3, can be loaded until they buckle within the elastic realm. The described course of the quasi-static axial load generated by the experimental test setup, figure 4.1, is reproducible for all experiments, as shown in figure 6.1b), so that the results are comparable.

Dynamic axial load

The step-shaped dynamic axial loads $F_x(t) \neq$ const. are generated with the experimental test setup by releasing the mass (no. 8a) in figure 4.1 by the electromagnet (no. 8b). By that, step-shaped dynamic axial loads up to $F_{x,\text{step}} \approx 2000\,\text{N}$ are realizable. Figure 6.2 shows the dynamic axial load $F_x(t)$ plotted versus time t that is used in the experiments of passive buckling and active buckling control for a single experiment, figure 6.2a), and for the $2 \cdot 30 = 60$ passive and active beam-column systems according to table 4.3, figure 6.2b).

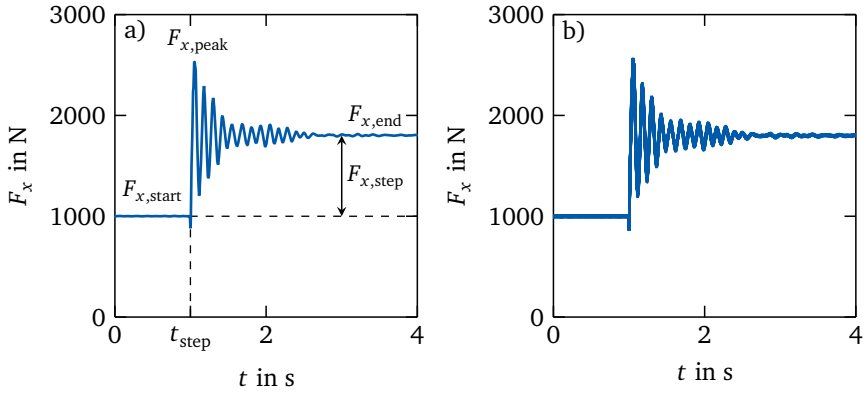

Figure 6.2.: Experimental step-shaped axial load F_x versus time t with axial step load $F_{x,\text{step}}$, a) single experiment, b) 60 experiments

The initial axial load in the conducted experiments is deliberately chosen as $F_{x,\text{start}} = 1000\,\text{N}$. Due to the dynamics of the experimental test setup, the axial load $F_x(t)$ is not an ideal step, but is influenced by the inertia of the hinged beam (no. 6a) with mass (no. 5) in figure 4.1. Thus, the axial load overshoots and has a peak value of $F_{x,\text{peak}}$. When the dynamic effects of the test setup have decayed, the beam-column system is loaded by the constant axial load $F_{x,\text{end}}$. The axial step load $F_{x,\text{step}} = F_{x,\text{end}} - F_{x,\text{start}}$, in this thesis, is defined as the difference of the axial load before and after application of the dynamic axial load.

The described course of the step-shaped dynamic axial load generated by the experimental test setup, figure 4.1, is reproducible for all experiments, as shown in figure 6.2b), so that the results are comparable. However, the experiments with the step-shaped dynamic axial loads cannot be performed as controlled as in the quasi-static load case since the peak axial loads may lead to plastic deformation by large

lateral deflections of the beam-columns. In order to prevent plastic deformation, a relatively small axial step load of $F_{x,\text{step}} \approx 800\,\text{N}$ is chosen for the experiments. This axial step load does not lead to dynamic buckling, as described in section 2.1.2, and no maximum bearable step load can be defined as characteristic property. Instead, the passive and active absolute modal displacements (6.2) of the passive and active beam-column systems at the start, peak and end of the axial step load $q_{1,\text{start,p/a}}$, $q_{1,\text{peak,p/a}}$ and $q_{1,\text{end,p/a}}$ according to figure 6.2 are chosen as characteristic properties to describe the step responses.

All experiments are conducted for the passive and active beam-column systems. In the following, first, the experimental results for slowly increasing quasi-static axial loads $F_x(t) \approx \text{const.}$ are presented in section 6.2. Then, the experimental results for step-shaped dynamic axial loads $F_x(t) \neq \text{const.}$ are discussed in section 6.3. Table 6.1 summarizes the investigated experimental cases regarding the type of axial load, deterministic or uncertain analysis and the associated sections.

Table 6.1.: Experimental cases for passive buckling and active buckling control

axial load	$F_x(t) \mid F_{x,\text{step}}$	determ. | uncert.	section
quasi-static	$337\,\text{N} \leq F_x(t) \leq F_{x,\text{max,p/a}}$	deterministic uncertain	6.2.1 6.2.2
dynamic	$F_{x,\text{step}} \approx 800\,\text{N}$	deterministic uncertain	6.3.1 6.3.2

6.2 Experimental results for quasi-static axial loads

This section presents the experimental results of the passive and active beam-column systems subject to the slowly increasing quasi-static axial loads $F_x(t)$ shown in figure 6.1. In the following, first, the deterministic experimental results of the passive and active beam-column system [b2-AB1-p1], table 4.3, are presented in section 6.2.1 to generally describe the quasi-static buckling behavior. Then, the uncertain experimental results of all 30 passive and active beam-column systems are presented in section 6.2.2 to quantify and evaluate uncertainty in the passive and active maximum bearable axial loads and compare them with each other.

6.2.1 Deterministic passive buckling and active buckling control

The experimental procedure for the generation and measurement of the axial load and the modal displacements $q_{1,y/z}(t)$ (6.1) is explained in section 6.1. Figure 6.3 shows the modal displacements $q_{1,y/z}(t)$ and the control inputs $u_{y/z}(t)$ (3.46) in y- and z-direction plotted versus time t for the passive and active beam-column system [b2-AB1-p1] loaded by the quasi-static axial load $F_x(t)$ in figure 6.1a). The control inputs $u_{y/z}(t)$ of the gain-scheduled $\mathscr{H}_\infty$ controller are calculated from the experimental measurement outputs $y_{y/z}(t)$ (3.48) and the dynamic LPV controller $\boldsymbol{R}(F_x, s)$ (3.77) according to the control law (3.57).

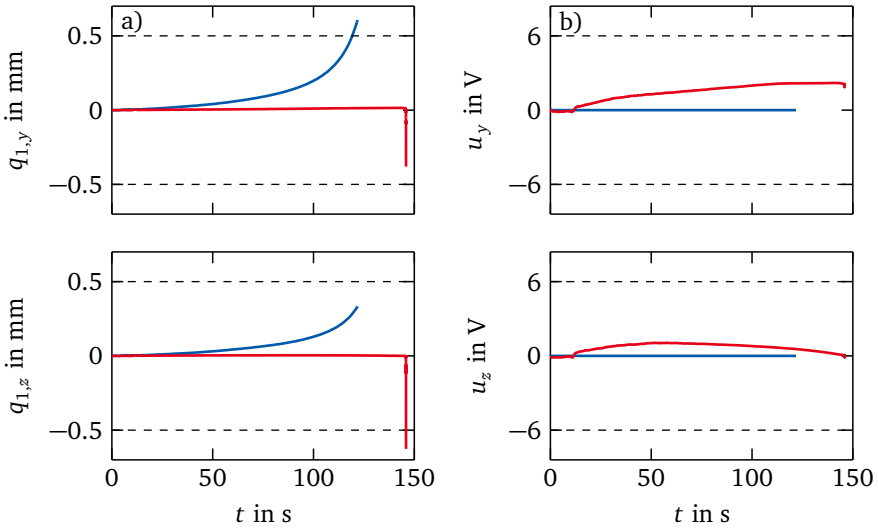

Figure 6.3.: Passive (——) and active (——) beam-column system [b2-AB1-p1] with quasi-static axial load F_x, a) modal displacements $q_{1,y}$ and $q_{1,z}$ versus time t, b) control inputs u_y and u_z versus time t

For the passive beam-column system, the modal displacements $q_{1,y/z}(t)$ in figure 6.3a) increase continuously with increasing axial load $F_x(t)$. The beam-column deflects in positive y- and z-direction and the modal displacement in y-direction reaches the maximum admissible displacement at $q_{1,y}(t \approx 120\,\mathrm{s}) = q_{1,\max}$. The control inputs $u_{y/z}(t)$ are zero for the passive beam-column system.

For the active beam-column system, the modal displacements $q_{1,y/z}(t)$ remain zero for the slowly increasing quasi-static axial load $F_x(t)$, contrary to the passive beam-column system. At $t \approx 145\,\mathrm{s}$, the beam-column suddenly deflects in negative y- and z-direction and reaches the maximum admissible displacement in z-direction. Figure 6.3b) shows the control inputs $u_{y/z}(t)$ of the gain-scheduled $\mathscr{H}_\infty$ controller. The control input $u_y(t)$ shows a continuous increase with a maximum value of 2.2 V and $u_z(t)$ first increases and then decreases with a maximum value of 1 V. Both control inputs are not close to the voltage limits $\max|u_{y/z}(t)| = 6\,\mathrm{V}$ that are necessary to not damage the piezoelectric stack actuators, section 4.1.2, after the control inputs are amplified by a factor of 10 by the piezo amplifiers, section 4.2.

To better interpret the quasi-static buckling behavior of the passive and active beam-column systems, the axial load $F_x(t)$ from figure 6.1 and the modal displacements $q_{1,y/z}(t)$ from figure 6.3a) are combined in figure 6.4. Thus, figure 6.4a) shows the load-displacement curve of the absolute modal displacement q_1 (6.2) from figure 6.3a) plotted versus the axial load F_x from figure 6.1.

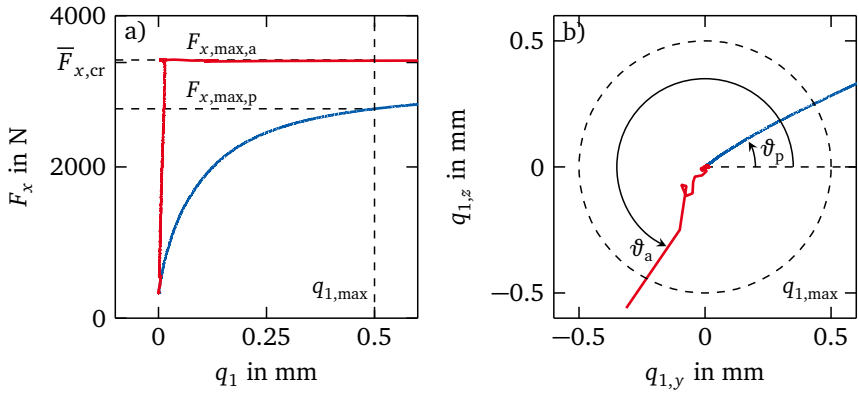

Figure 6.4.: Passive (——) and active (——) beam-column system [b2-AB1-p1] with quasi-static axial load F_x, a) absolute modal displacement q_1 versus axial load F_x, b) modal displacements $q_{1,y}$ versus $q_{1,z}$

The passive beam-column system shows the typical continuous increase in the modal displacement q_1 with increasing axial load F_x. Sudden buckling does not occur, as expected from section 2.1.1. The passive maximum bearable axial load $F_{x,\max,p} = 2768.8\,\mathrm{N} = 0.82\,\overline{F}_{x,cr}$ is considerably smaller than the mean critical buckling load $\overline{F}_{x,cr} = 3381.01\,\mathrm{N}$ estimated from the mean beam-column plant, section 5.2.3.

Figure 6.4b) shows the modal displacements $q_{1,y}$ and $q_{1,y}$ in y- and z-direction from figure 6.3 plotted versus each other. It can be interpreted as the beam-column center displacement in the y-z-plane and shows the passive and active direction of buckling $\vartheta_{\mathrm{p/a}}$ measured from the positive y-direction. In theory, the ideal beam-column with circular cross-section has infinite directions of buckling. In reality, however, the direction of buckling is the result of many influences, like the beam-column component properties, assembly and mounting variations as well as a possible preferred direction of the experimental test setup. These effects cannot be quantified separately. The particular experimental passive beam-column system [b2-AB1-p1] deflects continuously at an angle of $\vartheta_{\mathrm{p}} = 30°$.

For the active beam-column system, the gain-scheduled $\mathscr{H}_\infty$ controller keeps the absolute modal displacement q_1 close to zero for increasing quasi-static axial load F_x, contrary to the passive beam-column system, figure 6.4a). The gain-scheduled $\mathscr{H}_\infty$ controller is designed for axial loads up to $F_{x,\mathrm{u}} = 3600\,\mathrm{N}$, section 5.3.2. However, the absolute modal displacement only remains zero up to an axial load of $F_{x,\mathrm{max,a}} = 3414.5\,\mathrm{N} = 1.01\,\overline{F}_{x,\mathrm{cr}}$, which is an increase of 23% or 645.6 N compared to the passive beam-column system.

At $F_{x,\mathrm{max,a}}$, the beam-column starts to oscillate and finally buckles at an angle of $\vartheta_{\mathrm{a}} = 244°$ in approximately the opposite direction as the passive beam-column system, figure 6.4b). The oscillations originate from the influence of test setup dynamics, presumably the resonance frequency of the hinged beam in figure 4.1, which coincides with the decreasing first resonance frequency of the experimental beam-column systems in y- and z-direction in figure 5.9 and, thus, leads to flutter [93].

6.2.2 Uncertainty in passive buckling and active buckling control

This section presents the experimental results of all 30 passive and active beam-column systems according to table 4.3 with quasi-static axial loads. They are used to quantify and evaluate probabilistic uncertainty according to section 2.3.1 in the passive and active maximum bearable axial loads $F_{x,\mathrm{max,p}}$ and $F_{x,\mathrm{max,a}}$ by three-parameter WEIBULL distributions, section 2.3.2. Figure 6.5 shows the absolute modal displacement q_1 versus axial load F_x and the modal displacements $q_{1,y}$ versus $q_{1,z}$ in the y-z-plane, as given in figure 6.4 for the deterministic beam-column system [b2-AB1-p1].

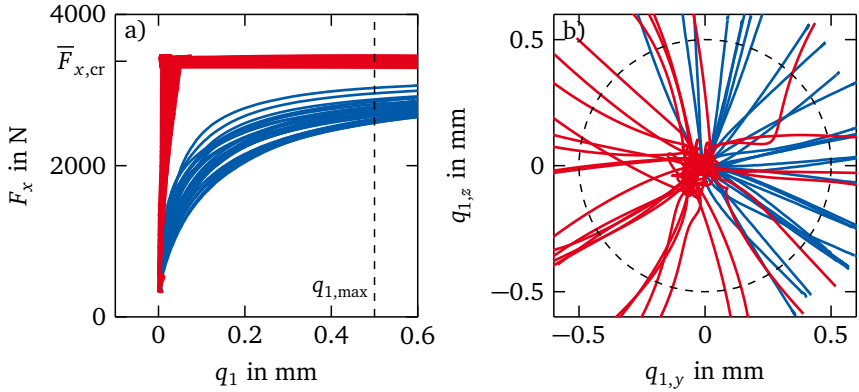

Figure 6.5.: All 30 passive (——) and active (——) beam-column systems with quasi-static axial load $F_x(t)$, a) absolute modal displacement q_1 versus axial load F_x, b) modal displacements $q_{1,y}$ versus $q_{1,z}$

In figure 6.5a), the passive beam-column systems all exhibit continuously increasing absolute modal displacements q_1 for increasing axial loads F_x with slightly different courses of the load-displacement curves. The resulting passive maximum bearable axial loads lie in the range of $2567.1\,\mathrm{N} \leq F_{x,\mathrm{max,p}} \leq 3029.4\,\mathrm{N}$. The absolute modal displacements of the active beam-column systems again remain close to zero for increasing axial loads up to the mean critical buckling load $\overline{F}_{x,\mathrm{cr}}$. Some active beam-column systems already show a slight increase in the absolute modal displacements prior to buckling due to the approximated integral action of the controller, as shown in figure 5.11. The active beam-column systems exhibit the same quasi-static buckling behavior as described for the deterministic beam-column system [b2-AB1-p1] in section 6.2.1. The observed active maximum bearable axial loads lie in the range of $3300.5\,\mathrm{N} \leq F_{x,\mathrm{max,a}} \leq 3451.6\,\mathrm{N}$.

In figure 6.5b), the directions of buckling $\vartheta_{\mathrm{p/a}}$ of the passive and active beam-column systems show large variations, which are attributed to the combined effects of the component variations according to table 4.3, which include the effects of manufacturing, assembly and mounting of the beam-column systems. The passive beam-column systems almost all buckle in the positive half-plane, whereas the active beam-column systems predominantly buckle in the negative half-plane. This indicates a possible systematic influence of the experimental test setup, which could not be eliminated despite thorough alignment of the test setup, section 4.1.1. The similar buckling behavior of the active beam-column systems despite of the different directions of buckling shows that the novel piezo-elastic supports, section 4.1.2, with active buckling control, section 3.1, are able to stabilize the active beam-column

systems in arbitrary lateral y- and z-direction. Since the passive and active maximum bearable axial loads $F_{x,\max,\mathrm{p}}$ and $F_{x,\max,\mathrm{a}}$ are more important for the practical use the beam-column systems than the direction of buckling, the latter is not considered for the further uncertainty quantification, which is presented in the following.

Uncertainty quantification and evaluation

The experimental results of the passive and active maximum bearable axial loads of all investigated beam-column systems are shown in the scatter plot in figure 6.6a) and the normalized histograms and empirical cdf in figure 6.6b).

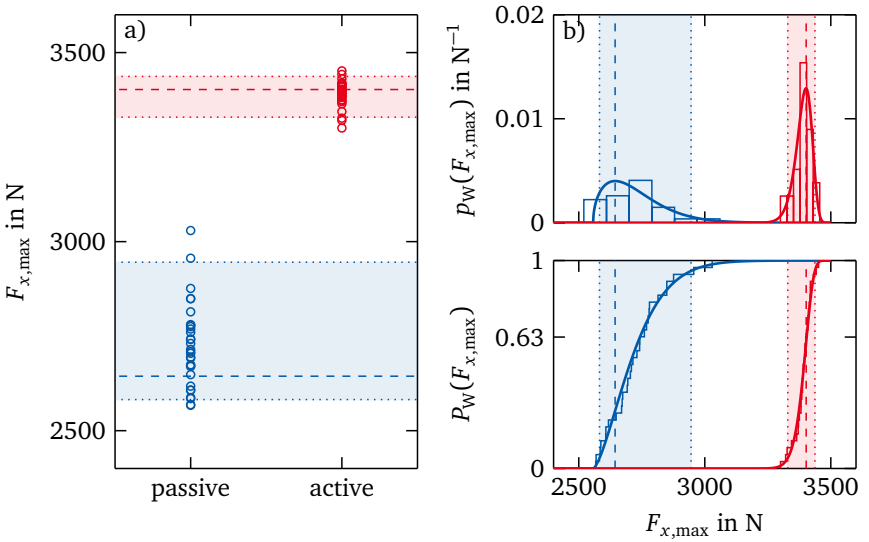

Figure 6.6.: **Passive** and **active** maximum bearable axial loads $F_{x,\max}$ with most likely value $\Sigma_{F_{x,\max}}$ (– –) and interpercentile range $R_{F_{x,\max}}$ ( ) for three-parameter WEIBULL distribution fits, a) scatter plot (○), b) normalized histograms and fitted pdf $p_{\mathrm{W}}(F_{x,\max})$ (top) and empirical and fitted cdf $P_{\mathrm{W}}(F_{x,\max})$ (bottom) (——)

The scatter plots, histograms and empirical cdf are unsymmetric with non-zero offset for both passive and active beam-column systems. As shown in section 2.3.2, variations of this form may be approximated by three-parameter WEIBULL distributions. The shape parameter β_X, scale parameter η_X and location parameter X_0 of the three-parameter WEIBULL distributions according to (2.13) for the maximum

bearable axial load $X = F_{x,\max}$ are fitted by the maximum likelihood estimator *mle* algorithm in the MATLAB® *Statistics and Machine Learning Toolbox*, [63], and are given in table 6.2.

Table 6.2.: Parameters of three-parameter WEIBULL distribution fits for maximum bearable axial loads $X = F_{x,\max,\mathrm{p/a}}$

case	β_X	η_X/N	X_0/N	Σ_X/N	R_X/N
passive	1.48	185.4	2557.2	2643.8	363.2
active	11.71	334.7	3069.4	3402.3	107.7
act./pass.	7.89	1.81	1.20	1.29	0.30

The fitted pdf $p_{\mathrm{W}}(F_{x,\max})$ (2.13) and cdf $P_{\mathrm{W}}(F_{x,\max})$ (2.10) show good agreement with the normalized histograms and empirical cdf in figure 6.6, which is also seen in the probability plots in figure A.3 in the appendix. Thus, the assumption of three-parameter WEIBULL distributions is admissible. The shape parameter $\beta_X = 1.48 < 3.5$ for the passive maximum bearable axial loads $X = F_{x,\max,\mathrm{p}}$ indicates that the pdf is positively skewed, therefore, most values of $F_{x,\max,\mathrm{p}}$ are on the left part of $p_{\mathrm{W}}(F_{x,\max,\mathrm{p}})$, section 2.3.2. The shape parameter $\beta_X = 11.71 > 3.5$ for the active maximum bearable axial loads $X = F_{x,\max,\mathrm{a}}$ indicates that the pdf is negatively skewed, so that most values of $F_{x,\max,\mathrm{a}}$ are on the right part of $p_{\mathrm{W}}(F_{x,\max,\mathrm{a}})$. This results from the consistent buckling failure of the active beam-column systems at axial loads close to the mean critical buckling load. The location parameter X_0 indicates the lowest value of $X = F_{x,\max,\mathrm{p/a}}$ for the passive or active beam-column systems, which is 20% higher for the active beam-column systems.

The location and variablity of the three-parameter WEIBULL distributions are characterized by the most likely values Σ_X (2.14) and the interpercentile ranges R_X (2.15), section 2.3.2, which are also given in table 6.2. They are used to compare the passive and active beam-column systems with respect to their maximum bearable axial loads $F_{x,\max,\mathrm{p}}$ and $F_{x,\max,\mathrm{a}}$. The most likely value $\Sigma_{F_{x,\max,\mathrm{a}}}$ of the active beam-column systems is increased by 29% or 758.2 N compared to the passive beam-column system. At the same time, the interpercentile range $R_{F_{x,\max,\mathrm{a}}}$, which contains 90% of all assumed maximum bearable axial loads and is indicated by the blue and red shaded areas in figure 6.6, of the active beam-column systems is reduced by 70% or 255.5 N compared to the passive beam-column system. Thus, the gain-scheduled $\mathscr{H}_\infty$ active buckling control considerably increases the maximum bearable axial load and exhibits a smaller variability. This is beneficial for the practical use of the active beam-column system, as the failure by buckling is less sensitive to the uncertainty introduced by component variations, assembly and mounting.

6.3 Experimental results for dynamic axial loads

This section presents the experimental results of the passive and active beam-column systems subject to the step-shaped dynamic axial loads $F_x(t)$ from figure 6.2. In the following, first, the experimental results of the passive and active beam-column system [b2-AB1-p1] are presented in section 6.3.1 to generally describe the dynamic step responses. Then, the experimental results of all 30 passive and active beam-column systems are presented in section 6.3.2 to quantify and evaluate uncertainty in the passive and active absolute modal displacements and compare them with each other.

6.3.1 Deterministic passive and active step response

Analog to figure 6.3 for the quasi-static axial load, figure 6.7 shows the modal displacements $q_{1,y/z}(t)$ (6.1) and the control inputs $u_{y/z}(t)$ (3.46) in y- and z-direction plotted versus time t for the passive and active beam-column system [b2-AB1-p1] loaded by the dynamic axial load $F_x(t)$ in figure 6.2a).

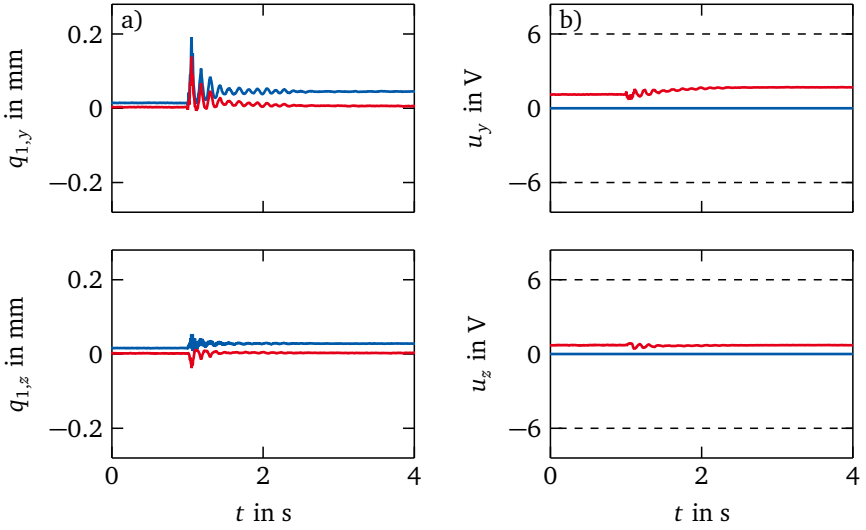

Figure 6.7.: Passive (——) and active (——) beam-column system [b2-AB1-p1] with dynamic axial load F_x, a) modal displacements $q_{1,y}$ and $q_{1,z}$ versus time t, b) control inputs u_y and u_z versus time t

For the passive beam-column system, the initial axial load $F_{x,\text{start}} = 1000\,\text{N}$ leads to non-zero initial modal displacements $q_{1,y/z,\text{start}}$ in figure 6.7a). The step-shaped axial load at $t_{\text{step}} \approx 1\,\text{s}$ amplifies the initial modal displacements and results in high peak modal displacements $q_{1,y/z,\text{peak}}$ in positive y- and z-direction. After application of the step-shaped axial load for $F_{x,\text{end}} \approx 1800\,\text{N}$, the final modal displacements $q_{1,y/z,\text{end}}$ have increased. The control inputs $u_{y/z}(t)$ in figure 6.2b) are zero for the passive beam-column system.

For the active beam-column system, the initial modal displacements $q_{1,y/z,\text{start}}$ are zero, as for the active beam-column system with quasi-static axial load, section 6.2.1. The peak modal displacement $q_{1,y,\text{peak}}$ in y-direction is smaller than in the passive beam-column system, but $q_{1,z,\text{peak}}$ deflects in negative z-direction and is slightly larger than in the passive beam-column system. The final modal displacements $q_{1,y/z,\text{end}}$ in the active beam-column system are again close to zero. The corresponding control inputs $u_{y/z}(t)$ are shown in figure 6.7b). Before and after application of the dynamic axial load $F_x(t)$, the control inputs $u_{y/z}(t)$ are constant with a maximum value of 1.7 V, which is again not close to the voltage limits $\max|u_{y/z}(t)| = 6\,\text{V}$.

To better interpret the experimental step response of the passive and active beam-column system, the modal displacements $q_{1,y/z}$ from figure 6.7a) are combined in figure 6.8. Figure 6.8a) shows the absolute modal displacement $q_1(t)$ versus time t in response to the step-shaped axial load from figure 6.2 for the passive and active beam-column system.

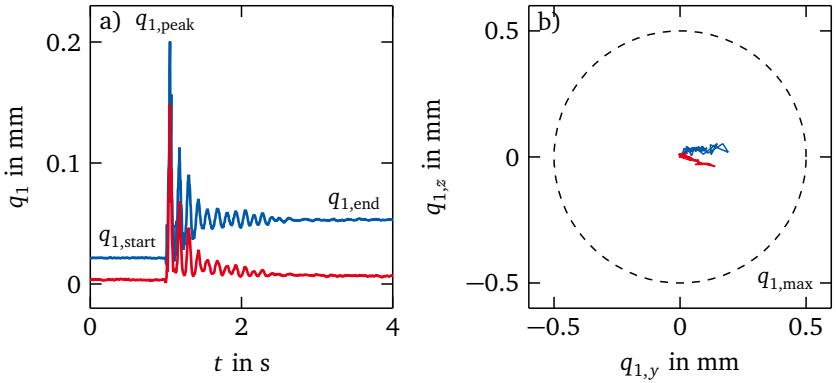

Figure 6.8.: Passive (——) and active (——) beam-column system [b2-AB1-p1] with dynamic axial load F_x, a) absolute modal displacement q_1 versus time t, b) modal displacements $q_{1,y}$ versus $q_{1,z}$

Table 6.3 shows the values of the absolute modal displacements before application of the step load $q_{1,\text{start}}$, for the peak displacements $q_{1,\text{peak}}$, and after application of the step load $q_{1,\text{end}}$. The absolute modal displacements $q_{1,\text{start}}$ and $q_{1,\text{end}}$ are significantly reduced by 84% and 87%, respectively, whereas the peak displacement $q_{1,\text{peak}}$ is reduced by 26%. This shows that the scheduling of the gain-scheduled $\mathscr{H}_\infty$ controller matrices (3.77) with the fast changing measured dynamic axial load $F_x(t) \neq \text{const.}$ works properly without the controller becoming instable.

Table 6.3.: Beam-column absolute modal displacements $q_{1,\text{start}}$, $q_{1,\text{peak}}$ and $q_{1,\text{end}}$ for dynamic axial load $F_x(t)$

case	$q_{1,\square}$ /mm		
	start	peak	end
passive	0.0215	0.2004	0.0527
active	0.0035	0.1483	0.0066
act./pass.	0.16	0.74	0.13

Figure 6.8b) shows the modal displacements $q_{1,y}(t)$ and $q_{1,z}(t)$ in y- and z-direction from figure 6.7 plotted versus each other. The passive beam-column system almost solely deflects in positive y-direction with angle $\vartheta_\text{p} = 10°$. The active beam-column system deflects in similar direction with angle $\vartheta_\text{a} = 344°$.

The peak and final absolute modal displacements $q_{1,\text{peak}}$ and $q_{1,\text{end}}$ of the passive and active beam-column systems are not close to the maximum admissible modal displacement $q_{1,\max} = 0.5\,\text{mm}$ according to (6.3) for quasi-static loads $F_x(t) \approx \text{const.}$ However, other beam-column systems exhibit considerably larger absolute modal displacements, as shown in figure 6.9. To avoid plastic deformation of the five investigated beam-columns (b1–b5) in table 4.3, the passive and active beam-column systems for the uncertainty quantification in section 6.3.2 are all loaded by the same step load $F_{x,\text{step}} \approx 800\,\text{N}$ as shown in figure 6.2b) and table 6.1.

6.3.2 Uncertainty in passive and active step response

This section presents the experimental results of all 30 passive and active beam-column systems according to table 4.3 with step-shaped dynamic axial loads. They are used to quantify and evaluate probabilistic uncertainty according to section 2.3.1 in the passive and active absolute modal displacements $q_{1,\text{p}}$ and $q_{1,\text{a}}$ (6.2) for start,

peak and end of the axial step load according to figure 6.2 by three-parameter WEIBULL distributions, section 2.3.2. Figure 6.9 shows the absolute modal displacement q_1 versus time t and the modal displacements $q_{1,y}$ versus $q_{1,z}$ in the y-z-plane.

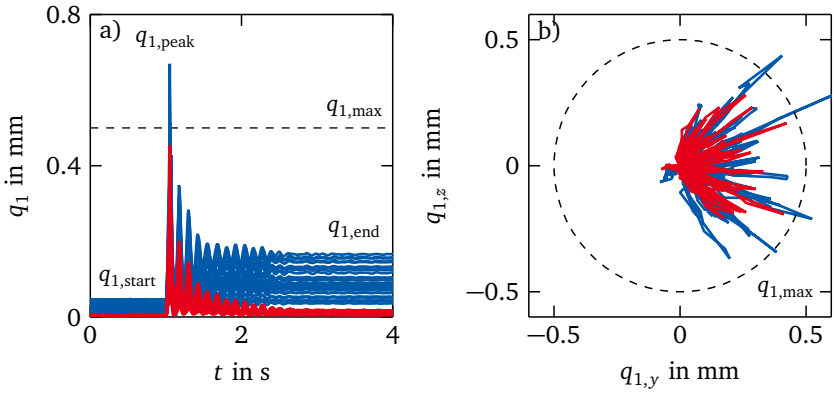

Figure 6.9.: All 30 passive (——) and active (——) beam-column systems with dynamic axial load $F_x(t)$, a) absolute modal displacement q_1 versus time t, b) modal displacements $q_{1,y}$ versus $q_{1,z}$

The step responses of the passive and active beam-column systems in figure 6.9a) are similar to the determinstic beam-column system [b2-AB1-p1] from figure 6.8. The passive beam-column systems exhibit non-zero initial absolute modal displacements $q_{1,\text{start}}$ that are amplified by the step-shaped axial load to result in high peak absolute modal displacements $q_{1,\text{peak}}$ and final absolute modal displacements $q_{1,\text{end}}$. In contrast to the deterministic case in figure 6.8, some peak absolute modal displacements exceed the maximum admissible modal displacement $q_{1,\text{max}} = 0.5\,\text{mm}$ according to (6.3). However, the peak lateral deflections only occur for a very limited time span, so that the passive beam-column system is not considered as buckled, section 2.1.2.

The initial and final absolute modal displacements $q_{1,\text{start}}$ and $q_{1,\text{end}}$ of the active beam-column system are close to zero. The peak absolute modal displacements $q_{1,\text{peak}}$ are smaller and decay faster than in the passive beam-column systems. Furthermore, the peak displacements do not exceed the maximum admissible modal displacement $q_{1,\text{max}}$.

The passive and active beam-column systems deflect in similar directions with angles $\vartheta_{p/a}$, figure 6.9b). The variations in $\vartheta_{p/a}$ are smaller than in the case of the quasi-static axial loads from 6.5b), which again indicates a possible systematic influence of the experimental test setup that is more pronounced for the generation of the step-shaped dynamic axial loads, section 4.1.1. As in the quasi-static load case, section 6.2.2, the direction of deflection is not considered for the further uncertainty quantification, which is presented in the following.

Uncertainty quantification and evaluation

The experimental results of the absolute modal displacements $q_{1,\mathrm{start}}$, $q_{1,\mathrm{peak}}$ and $q_{1,\mathrm{end}}$ for the step-shaped axial loads of all investigated passive and active beam-column systems from figure 6.9 are shown in the scatter plot in figure 6.10. The corresponding normalized histograms and empirical cdf are shown in figure 6.11. Again, the most likely values Σ_{q_1} (2.14) and the interpercentile ranges R_{q_1} (2.15) for the three-parameter WEIBULL distribution fits from table 6.4 are indicated.

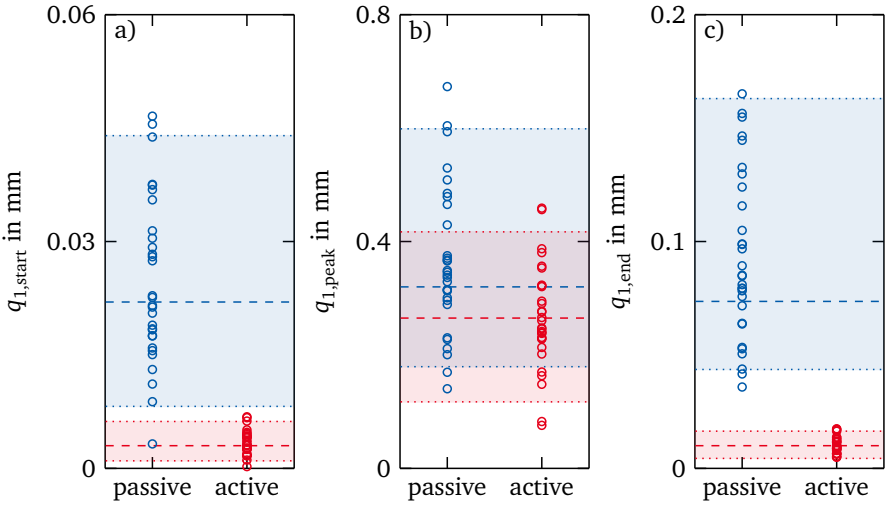

Figure 6.10.: **Passive** and **active** absolute modal displacements q_1: scatter plot (○) with most likely value Σ_{q_1} (– –) and interpercentile range R_{q_1} ( ) for three-parameter WEIBULL distribution fits, a) $q_{1,\mathrm{start}}$, b) $q_{1,\mathrm{peak}}$, c) $q_{1,\mathrm{end}}$

As in the uncertainty quantification for the beam-column systems subject to quasi-static axial loads in section 6.2.2, the variations in the absolute modal displacements are approximated by three-parameter WEIBULL distributions (2.13). The

fitted pdf $p_W(X)$ (2.13) and cdf $P_W(X)$ (2.10) for the absolute modal displacements $X = q_{1,start}$, $q_{1,peak}$ and $q_{1,end}$ show a good agreement with the normalized histograms and empirical cdf in figure 6.11, which is also seen in the probability plots in figure A.4 in the appendix. Therefore, the assumption of three-parameter WEIBULL distributions is admissible.

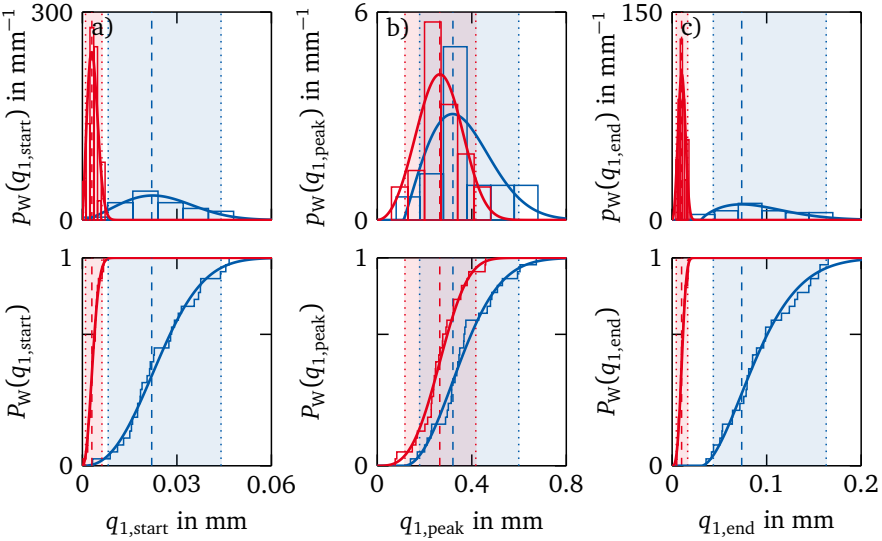

Figure 6.11.: **Passive** and **active** absolute modal displacements q_1: normalized histograms and fitted pdf $p_W(q_1)$ (top) and empirical and fitted cdf $P_W(q_1)$ (bottom) (——) with most likely value Σ_{q_1} (– –) and interpercentile range R_{q_1} ( ) for three-parameter WEIBULL distribution fits, a) $q_{1,start}$, b) $q_{1,peak}$, c) $q_{1,end}$

The shape parameters β_X, scale parameters η_X and location parameters X_0 of the three-parameter WEIBULL distributions for the absolute modal displacements are given in table 6.4. The initial absolute modal displacements of the passive and all absolute modal deflections of the active beam-column systems are best fitted by two-parameter WEIBULL distributions, indicated by the location parameter $X_0 = 0$, section 2.3.2. This is reasonable, as the goal of the gain-scheduled $\mathcal{H}_\infty$ controller is to minimize the lateral beam-column deflections so that they are close to zero. All shape parameters are $\beta_X < 3.5$ so that the fitted pdf $p_W(X)$ (2.13) and cdf $P_W(X)$ (2.10) for the absolute modal displacements $X = q_{1,start}$, $q_{1,peak}$ and $q_{1,end}$ are positively skewed.

Table 6.4.: Parameters of the three-parameter WEIBULL distribution fits for the absolute modal displacements $X = q_{1,\text{start}}$, $q_{1,\text{peak}}$ and $q_{1,\text{end}}$

$X = q_{1,\square}$	case	β_X	η_X/mm	X_0/mm	Σ_X/mm	R_X/mm
start	passive	2.42	0.028	0	0.022	0.036
	active	2.25	0.004	0	0.003	0.005
	act./pass.	0.93	0.14	–	0.13	0.15
peak	passive	2.06	0.286	0.111	0.320	0.419
	active	3.21	0.296	0	0.265	0.300
	act./pass.	1.56	1.04	–	0.83	0.71
end	passive	1.73	0.070	0.031	0.074	0.119
	active	3.11	0.012	0	0.010	0.012
	act./pass.	1.80	0.17	–	0.14	0.10

The most likely values Σ_X (2.14) of the absolute modal displacements $X = q_{1,\text{start}}$ and $X = q_{1,\text{end}}$ in the active beam-column systems are significantly reduced by 87% and 86%, respectively, compared to the passive beam-column system. The interpercentile range R_X (2.15), which is indicated by the blue and red shaded areas in figures 6.10 and 6.11, of the active beam-column systems is likewise reduced by 85% and 90%, respectively. The most likely value of the absolute peak displacement $X = q_{1,\text{peak}}$ is reduced by 17% and the corresponding interpercentile range is reduced by 29%. Due to the reduced absolute modal displacements, the active beam-column systems are expected to sustain higher step-shaped axial loads.

6.4 Discussion of results

This section discusses the experimental results obtained for the 30 nominally identical passive and active beam-column systems, section 4.1.3, subject to slowly increasing quasi-static axial loads $F_x(t) \approx$ const., section 6.2, and step-shaped dynamic axial loads $F_x(t) \neq$ const., section 6.3.

The passive beam-column systems exhibit real buckling behavior for slowly increasing quasi-static axial loads and fail according to (6.3) at the passive maximum bearable axial loads $F_{x,\text{max,p}}$. The active beam-column systems are stabilized in arbitrary lateral directions up to the active maximum bearable axial loads $F_{x,\text{max,a}}$, which are at least 9% or 271.1 N higher than the highest passive maximum bearable

axial load $F_{x,\mathrm{max,p}}$. The active beam-column systems exhibit an increase in the most likely values Σ_X by 29% and a reduction in the interpercentile range R_X by 70% compared to the passive beam-column systems.

For quasi-static axial loads, the relative increase in the maximum bearable axial loads is comparable to earlier experimental investigations on active buckling control introduced in section 2.2. However, the absolute values of the maximum bearable axial loads of the practical beam-column system investigated in this thesis, represented by the most likely values of the passive and active beam-column systems $\Sigma_{F_{x,\mathrm{max,p}}} = 2643.8\,\mathrm{N}$ and $\Sigma_{F_{x,\mathrm{max,a}}} = 3402.3\,\mathrm{N}$ from table 6.2, significantly exceed those found in earlier experimental studies with $F_{x,\mathrm{max,p}} \leq 74\,\mathrm{N}$ and $F_{x,\mathrm{max,a}} \leq 151\,\mathrm{N}$, table 2.2. Furthermore, the quantification and evaluation of uncertainty due to component variations that combine the effects of manufacturing, assembly and mounting broadens the current state of research and shows the feasibility of the active buckling control for the practical beam-column system.

The active buckling control for step-shaped dynamic axial loads is generally novel and is evaluated with regard to the measured absolute modal displacements $q_{1,\mathrm{start}}$, $q_{1,\mathrm{peak}}$ and $q_{1,\mathrm{end}}$ at different moments of the passive and active step responses. The probabilistic uncertainty in the absolute modal displacements, is assumed to be a measure for the uncertainty in the maximum step loads of the passive and active beam-column systems. The active beam-column systems exhibit a reduction in the most likely values of the absolute modal displacements Σ_X of up to 87% with no lasting deformation after the step load and a reduction in the interpercentile ranges R_X by up to 90% compared to the passive beam-column systems. Furthermore, the scheduling with the measured dynamic axial load $F_x(t) \neq \text{const.}$ of the gain-scheduled $\mathscr{H}_\infty$ controller from section 3.3 does not become instable for fast changes of the axial load $F_x(t)$. The active buckling control for dynamic axial loads that are common in practical beam-column systems has so far not been investigated elsewhere and is new in this thesis.

In summary, the active buckling control by the novel piezo-elastic supports and the gain-scheduled $\mathscr{H}_\infty$ controller is successfully implemented for the practical beam-column system.

7 Conclusions and outlook

In this thesis, uncertainty in a novel active buckling control approach for a beam-column with circular cross-section subject to quasi-static and dynamic axial loads has been quantified and evaluated. The active buckling control was successfully applied to a practical beam-column system with relatively low slenderness ratio and relatively high critical buckling load. In particular, the objectives were to stabilize a practical beam-column system in arbitrary lateral direction by using innovative piezo-elastic supports with gain-scheduled $\mathscr{H}_\infty$ control and to experimentally quantify and evaluate probabilistic uncertainty in the maximum bearable axial loads and lateral deflections of the passive and active beam-column systems. By that, the applicability of the approach for active buckling control in practical truss structures can be assessed.

A comprehensive review on the background in static and dynamic passive buckling and the research on active buckling control of axially loaded beam-columns classified the different types of buckling failure and showed previous active approaches to increase the maximum bearable axial loads of passive beam-column systems. In general, passive beam-column systems subject to compressive axial loads are sensitive to failure by buckling. Uncertainty due to imperfections in real beam-column systems leads to increased lateral deflections, so that the maximum bearable axial loads are reduced considerably compared to the critical buckling load of ideal beam-column systems. Active buckling control has been shown to increase the maximum bearable axial load of academic beam-column systems with rectangular cross-sections, relatively high slenderness ratios and relatively low critical buckling loads subject to (quasi-)static axial loads. Uncertainty in the material, geometry, loading or support properties may significantly reduce the maximum bearable load and, therefore, needs to be quantified. However, uncertainty in the active buckling control, expressed e.g. by probabilistic uncertainty in the maximum bearable axial loads, has not been considered in most previous studies.

In contrast to the current state of research, this study examined the active buckling control of a practical beam-column system with circular cross-section, relatively low slenderness ratio and relatively high critical buckling load subject to quasi-static and dynamic axial loads. Furthermore, uncertainty in the maximum

bearable axial loads and lateral deflections due to component variations in the passive and active beam-column systems is quantified and evaluated.

In the concept of the novel active buckling control approach, the beam-column with circular cross-section is supported by innovative piezo-elastic supports with integrated piezoelectric stack actuators. They stabilize the beam-column in arbitrary lateral direction by active bending moments at each end of the beam-column. An LPV controller, in particular a gain-scheduled $\mathscr{H}_\infty$ controller, was used for active buckling control. The gain-scheduled $\mathscr{H}_\infty$ controller guarantees stability and performance for arbitrary trajectories of the dynamic axial load within the operation range of the axial load that includes supercritical axial loads exceeding the critical buckling load of the passive beam-column system. In the active beam-column systems, the dynamic LPV controller is scheduled in real-time with the measured axial load. For controller design, the beam-column including the piezo-elastic supports is modeled by an axial load-dependent FE model, which is reduced by modal truncation and augmented by the dynamic transfer behavior of the electrical components. The resulting beam-column plant is a polytopic LPV system with a defined operation range of the axial load, which was used for controller synthesis. By analyzing the lateral dynamic behavior of the closed-loop beam-column plant, the controller performance was numerically verified.

An experimental test setup was designed to load the experimental beam-column system with slowly increasing quasi-static and step-shaped dynamic axial loads. Variations in the lateral axial load-dependent dynamic behavior of the passive beam-column system were determined from experiments with a representative sample of 30 nominally identical beam-column systems by combining five different beam-columns, three different sets of piezo-elastic supports and two sets of piezoelectric stack actuators. The model parameters of the beam-column plant were calibrated individually for all investigated beam-column systems. Probabilistic uncertainty in the calibrated parameters was assumed by normal distributions, which determine a mean beam-column plant for controller synthesis. Based on the mean beam-column plant, the gain-scheduled $\mathscr{H}_\infty$ controller was tuned by frequency-dependent input and output weights and the performance of the closed-loop plant was verified numerically. The controller was designed to include integral action to reduce the static lateral beam-column deflections and, thus, increase the maximum bearable axial loads of the active beam-column systems.

Passive buckling and active buckling control of the beam-column systems was investigated in the experimental test setup for slowly increasing quasi-static and step-shaped dynamic axial loads. The variations in the characteristic properties, maximum bearable axial loads and lateral deflections, of the 30 nominally identical

passive and active beam-column systems are fitted by three-parameter WEIBULL distributions. Thus, probabilistic uncertainty in the characteristic values due to component variations, which combine the effects of manufacturing, assembly and mounting of the beam-column systems, is quantified and evaluated. The fitted WEIBULL distributions are compared with respect to their most likely values and variability. For quasi-static axial loads, the active beam-column systems exhibit an increase in the most likely values of the maximum bearable axial loads by 29% and a reduction in the variability by 70% compared to the passive beam-column systems. For step-shaped dynamic axial loads, the active beam-column systems exhibit a reduction in the most likely values of the absolute modal displacements of up to 87% and a reduction in the variability by up to 90% compared to the passive beam-column systems.

In summary, the experimental investigations show the successful application of active buckling control by novel piezo-elastic supports and gain-scheduled $\mathscr{H}_\infty$ control to a practical beam-column system with circular cross-section, relatively low slenderness ratio and relatively high critical buckling load for both quasi-static and dynamic axial loads. Furthermore, the quantification and evaluation of probabilistic uncertainty in the maximum bearable axial loads and lateral deflections shows that the active beam-column systems exhibit smaller variability than the passive beam-column systems, which is beneficial for the usage in real applications.

Based on the findings of this thesis, further investigations on the limitations of the proposed active buckling control for step-shaped dynamic axial loads may be performed. Uncertainty in the maximum step loads of the passive and active beam-column systems may be quantified. The experimental results for passive buckling and active buckling control presented in this thesis are limited to the single beam-column system. Therefore, the main future objective will be the implementation of the active beam-column system into an experimental lightweight truss structure to study the influence of the active buckling control on the performance and stability of the truss structure.

A Appendix

A.1 Probability plots

Probability plots are used to graphically assess the quality of a fitted probability distribution for a given data set. Normal distributions are assumed for the experimental axial load-dependent first resonance frequencies $f_{1,y/z,\mathrm{exp}}(F_x)$ in figure A.1 and the calibrated parameter sets $\boldsymbol{p}_y$ and $\boldsymbol{p}_z$ for the uncertain lateral dynamic behavior of the beam-column plant in figure A.2.

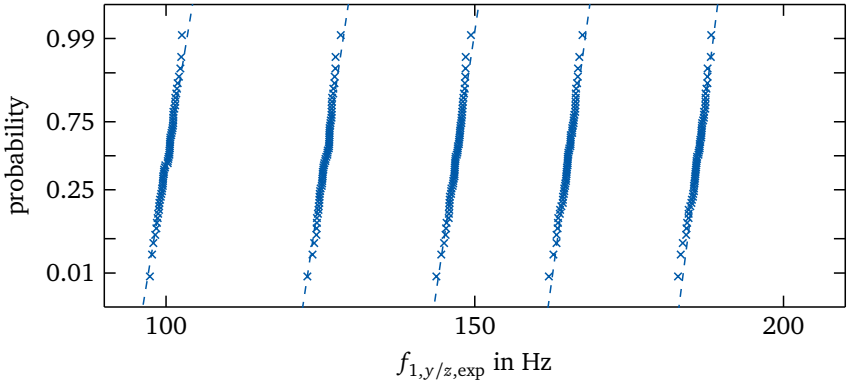

Figure A.1.: Probability plots for assumed normal distributions (– –) of the experimental first resonance frequencies $f_{1,y/z,\mathrm{exp}}(F_x)$ (×)

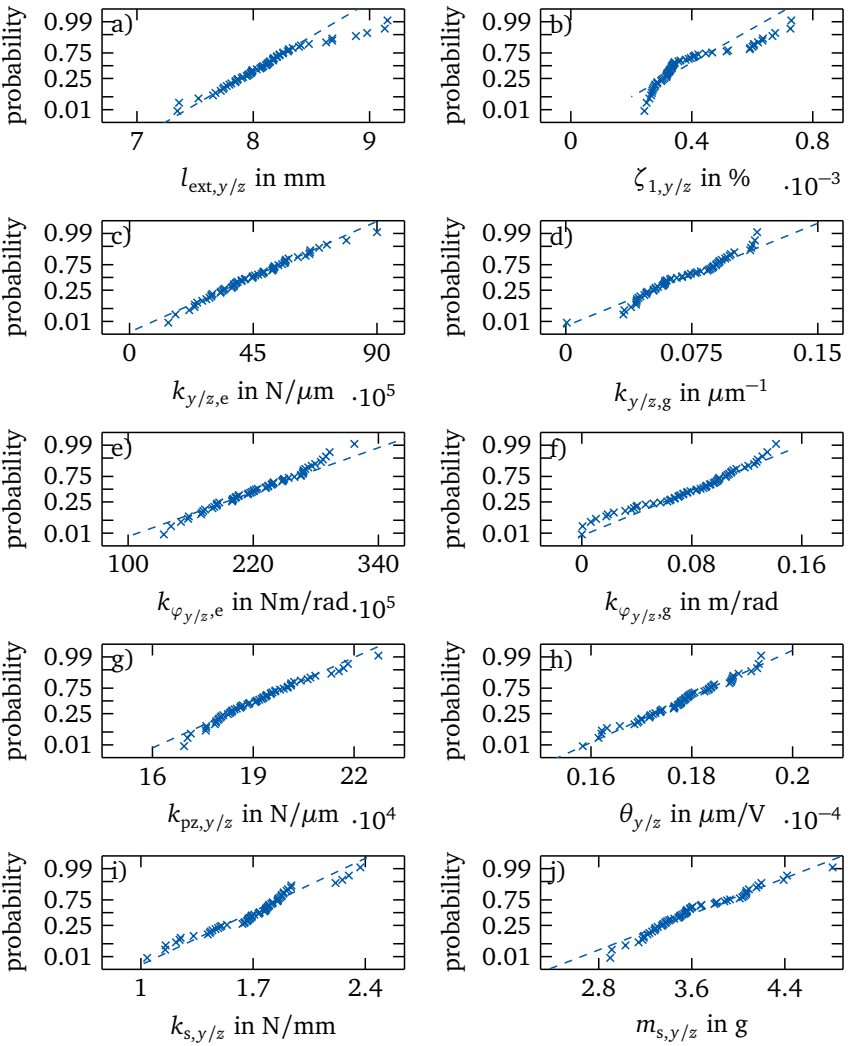

Figure A.2.: Probability plots for assumed normal distributions (– –) of the $2 \cdot 30$ calibrated parameter sets $\boldsymbol{p}_y$ and $\boldsymbol{p}_z$ (×)

Three-parameter WEIBULL distributions are assumed for the experimental passive and active maximum bearable axial loads $F_{x,\mathrm{max,p/a}}$ in figure A.3 and the experimental passive and active absolute modal displacements $q_{1,\mathrm{start,p/a}}$, $q_{1,\mathrm{peak,p/a}}$ and $q_{1,\mathrm{end,p/a}}$ in figure A.4. The probability plots are shifted by the location parameters X_0 from tables 6.2 and 6.4.

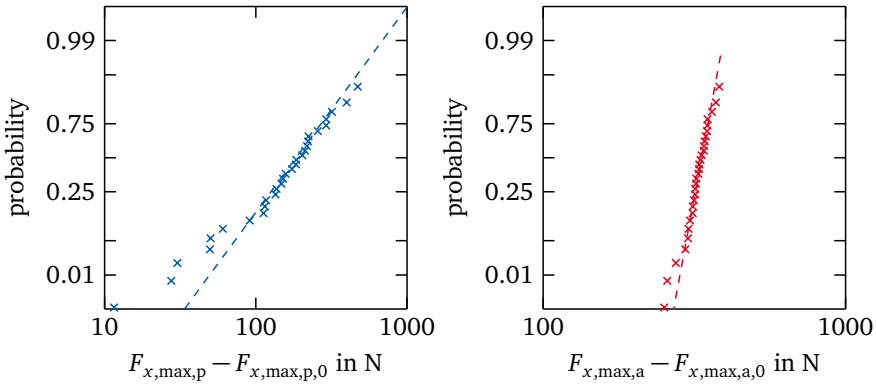

Figure A.3.: Probability plots for assumed three-parameter WEIBULL distributions shifted by the location parameters X_0 from table 6.2 (– –) of the experimental **passive** and **active** maximum bearable axial loads $F_{x,\mathrm{max,p/a}}$ (×)

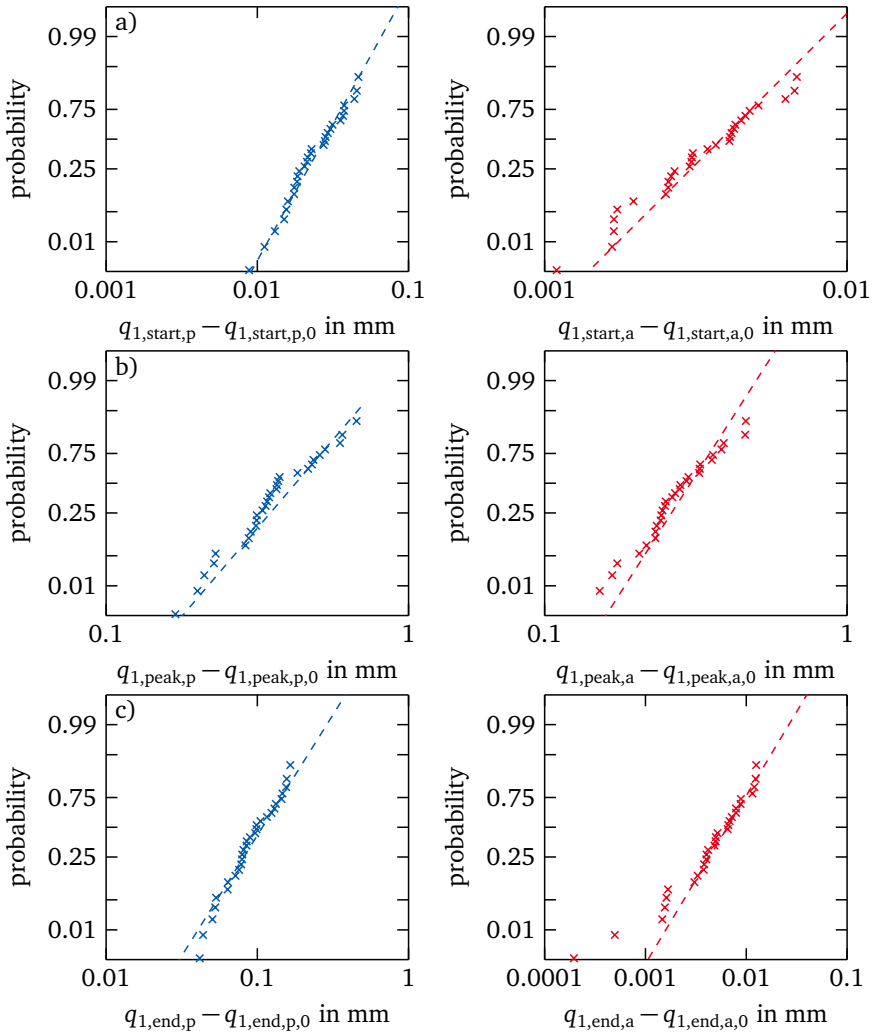

Figure A.4.: Probability plots for assumed three-parameter WEIBULL distributions shifted by the location parameters X_0 from table 6.4 (– –) of the experimental **passive** and **active** absolute modal displacements q_1 (×), a) $q_{1,\mathrm{start}}$, b) $q_{1,\mathrm{peak}}$, c) $q_{1,\mathrm{end}}$

A.2 Controller weights

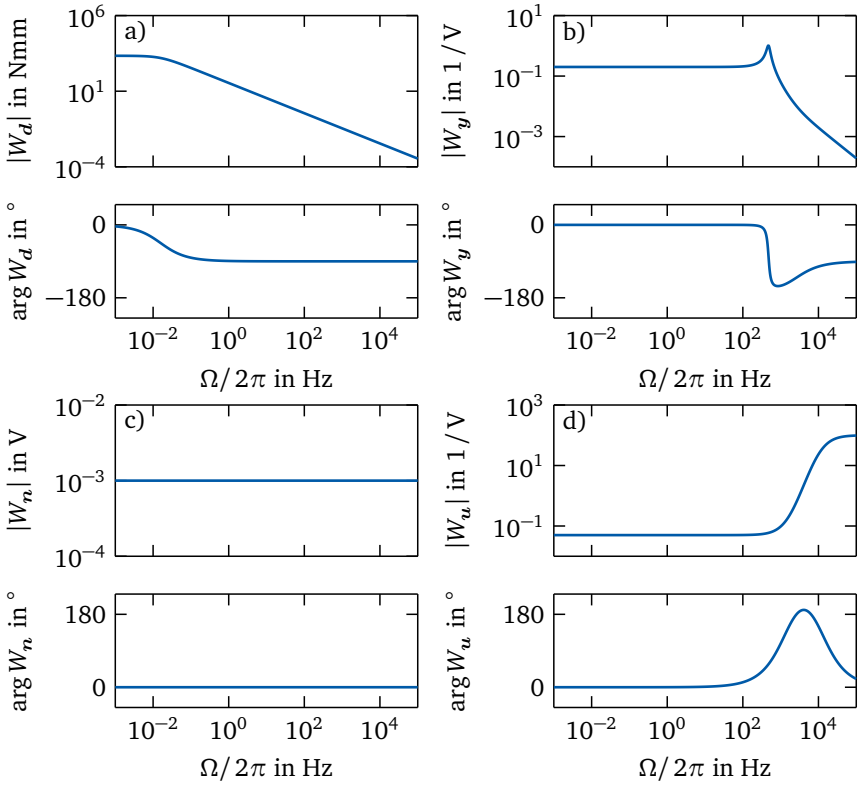

Figure A.5.: Amplitude and phase responses of the input and output weight transfer functions plotted versus excitation frequency $\Omega/2\pi$, a) disturbance end moments $W_d(\Omega)$, b) measurement output without measurement noise $W_y(\Omega)$, c) measurement noise $W_n(\Omega)$, d) and the control input $W_u(\Omega)$

References

[1] Amarante dos Santos, F. *Buckling Control Using Shape-Memory Alloy Cables*. In: *Journal of Engineering Mechanics* 142.6 (2016), p. 04016029.

[2] Angermann, A. *MATLAB – Simulink – Stateflow. Grundlagen, Toolboxen, Beispiele*. München: Oldenbourg, 2011.

[3] Apkarian, P., Biannic, J.-M., and Gahinet, P. *Self-scheduled $\mathscr{H}_\infty$ control of missile via linear matrix inequalities*. In: *Journal of Guidance, Control, and Dynamics* 18.3 (1995), pp. 532–538.

[4] Apkarian, P., Gahinet, P., and Becker, G. *Self-scheduled $\mathscr{H}_\infty$ control of linear parameter-varying systems. A design example*. In: *Automatica* 31.9 (1995), pp. 1251–1261.

[5] Aristizábal-Ochoa, J. D. *Stability and Second-Order Analyses of Frames with Semigrid Connection under Distributed Axial Loads*. In: *Journal of Structural Engineering* 127 (2001), pp. 1306–1315.

[6] Balas, G. et al. *Robust Control Toolbox. User's Guide*. Natick, MA: MathWorks, 2018.

[7] Balas, M. J. *Active control of flexible systems*. In: *Journal of Optimization Theory and Applications* 25.3 (1978), pp. 415–436.

[8] Becker, F. B. *Aktive Wälzlagerung zur Reduktion von Rotorschwingungen*. Dissertation. Darmstadt: Technische Universität Darmstadt, 2017.

[9] Becker, G. and Packard, A. *Robust performance of linear parametrically varying systems using parametrically-dependent linear feedback*. In: *Systems & Control Letters* 23.3 (1994), pp. 205–215.

[10] Berlin, A. A. *Towards Intelligent Structures: Active Control of Buckling*. Dissertation. Cambridge: Massachusetts Institute of Technology, 1994.

[11] Berlin, A. A. et al. *MEMS-Based Control of Structural Dynamic Instability*. In: *Journal of Intelligent Material Systems and Structures* 9.7 (1998), pp. 574–586.

[12] Bertsche, B. et al. *Zuverlässigkeit mechatronischer Systeme*. Berlin: Springer, 2009.

[13] Bokaian, A. *Natural Frequencies of Beams under Compressive Axial Loads*. In: *Journal of Sound and Vibration* 126.1 (1988), pp. 49–65.

[14] Bolotin, V. V. *The Dynamic Stability of Elastic Systems*. San Francisco: Holden-Day, 1964.

[15] Boyd, S. P. *Linear matrix inequalities in system and control theory*. Vol. 15. SIAM studies in applied mathematics. Philadelphia, Pa: Society for Industrial and Applied Mathematics, 1994.

[16] Brandt, A. *Noise and vibration analysis. Signal analysis and experimental procedures*. Hoboken, NJ: Wiley, 2011.

[17] Chase, J. G. and Yim, M. H. *Optimal Stabilization of Column Buckling*. In: *Journal of Engineering Mechanics* 125.9 (1999), pp. 987–993.

[18] Choi, S.-K., Grandhi, R. V., and Canfield, R. A. *Reliability-based Structural Design*. London: Springer, 2007.

[19] Choi, S. et al. *The active buckling control of laminated composite beams with embedded shape memory alloy wires*. In: *Composite Structures* 47 (1999), pp. 679–686.

[20] Chopra, A. K. *Dynamics of structures. Theory and applications to earthquake engineering*. Englewood Cliffs, NJ: Prentice-Hall, 1995.

[21] Davis, J. R. *Properties and selection. Nonferrous alloys and special-purpose materials*. Vol. 2. ASM handbook. Materials Park, Ohio: ASM International, 2000.

[22] Doyle, J. *Analysis of feedback systems with structured uncertainties*. In: *IEE Proceedings D Control Theory and Applications* 129.6 (1982), p. 242.

[23] Eifler, T. et al. *Approach for a Consistent Description of Uncertainty in Process Chains of Load Carrying Mechanical Systems*. In: *Applied Mechanics and Materials* 104 (2011), pp. 133–144.

[24] Elishakoff, I. *Uncertain buckling: its past, present and future*. In: *International Journal of Solids and Structures* 37 (2000), pp. 6869–6889.

[25] Engelhardt, R. A. *Uncertainty mode and effects analysis – heuristische Methodik zur Analyse und Beurteilung von Unsicherheiten in technischen Systemen des Maschinenbaus*. Dissertation. Darmstadt: Technische Universität Darmstadt, 2013.

[26] Enss, G. C. *Beherrschung von Unsicherheit am Beispiel eines aktiv gegen Knicken stabilisierten Systems*. Dissertation. Darmstadt: Technische Universität Darmstadt, 2016.

[27] Enss, G. C. and Platz, R. *Evaluation of uncertainty in experimental active buckling control of a slender beam-column with disturbance forces using Weibull analysis*. In: *Mechanical Systems and Signal Processing* 79 (2016), pp. 123–131.

[28] Enss, G. C. et al. *Device for bearing design elements in lightweight structures (Festkörperlager)*. DE 10 2015 101 084 A1. 2016.

[29] Euler, L. *Methodus inveniendi lineas curvas maximi minimive proprietate gaudentes, sive Solutio problematis isoperimetrici latissimo sensu accepti*. 1744.

[30] Fuller, C. R., Elliott, S. J., and Nelson, P. A. *Active Control of Vibration*. London: Academic Press, Inc, 1997.

[31] Galambos, T. V., ed. *Guide to stability design criteria for metal structures*. New York, NY: John Wiley, 1998.

[32] Galambos, T. V. and Surovek, A. E. *Structural Stability of Steel. Concepts and Applications for Structural Engineers*. Hoboken, NJ: John Wiley, 2008.

[33] Gawronski, W. *Balanced Control of Flexible Structures*. Vol. 211. Lecture Notes in Control and Information Sciences. London: Springer, 1996.

[34] Gawronski, W. *Advanced structural dynamics and active control of structures*. Mechanical Engineering Series. New York, NY: Springer-Verlag, 2004.

[35] Götz, B. *Evaluation of uncertainty in the vibration attenuation with shunted piezoelectric transducers integrated in a beam-column support*. Dissertation. Darmstadt: Technische Universität Darmstadt, 2019.

[36] Götz, B., Platz, R., and Melz, T. *Effect of static axial loads on the lateral vibration attenuation of a beam with piezo-elastic supports*. In: *Smart Materials and Structures* 27.3 (2018), p. 035011.

[37] Götz, B. et al. *Model verification and validation of a piezo-elastic support for passive and active structural control of beams with circular cross-section*. In: *Applied Mechanics and Materials, Trans Tech Publications* 807 (2015), pp. 67–77.

[38] Gross, D. et al. *Technische Mechanik 2. Elastostatik*. Berlin: Springer, 2007.

[39] Gu, D.-W., Petkov, P. H., and Konstantinov, M. M. *Robust control design with MATLAB*. Advanced Textbooks in Control and Signal Processing. London: Springer, 2013.

[40] Han, H. P. et al. *Buckling enhancement of epoxy columns using embedded shape memory alloy spring actuators*. In: *Composite Structures* 72.2 (2006), pp. 200–211.

[41] Hanselka, H. and Platz, R. *Ansätze und Massnahmen zur Beherrschung von Unsicherheit in lasttragenden Systemen des Maschinenbaus*. In: *VDI-Zeitschrift Konstruktion* 11/12-2010 (2010), pp. 55–62.

[42] Hedrich, P. et al. *Comparison of a New Passive and Active Technology for Vibration Reduction of a Vehicle under Uncertain Load*. In: *Applied Mechanics and Materials* 807 (2015), pp. 57–66.

[43] Hesse, D., Hoppe, F., and Groche, P. *Controlling Product Stiffness by an Incremental Sheet Metal Forming Process*. In: *Procedia Manufacturing* 10 (2017), pp. 276–285.

[44] Hoffmann, C. *Linear parameter-varying control of systems of high complexity*. Dissertation. Hamburg: Technische Universität Hamburg-Harburg, 2016.

[45] Hoffmann, K. *An Introduction to Stress Analysis using Strain Gauges*. Hottinger-Baldwin-Messtechnik-GmbH, 1987.

[46] Janocha, H., ed. *Adaptronics and Smart Structures. Basics, Materials, Design, and Applications*. Berlin Heidelberg: Springer-Verlag, 2007.

[47] Klein, B. *FEM. Grundlagen und Anwendungen der Finite-Element-Methode im Maschinen- und Fahrzeugbau*. Wiesbaden: Vieweg+Teubner, 2012.

[48] Koiter, W. T. *A Translation of: The Stability of elastic Equilibrium*. 1945.

[49] Koning, C. and Taub, J. *Impact Buckling of thin Bars in the elastic Range, Hinged at both Ends*. NACA, 1934.

[50] Kounadis, A. N. *Dynamic buckling of limit-point systems under step loading*. In: *Dynamics and Stability of Systems* 3.3-4 (1988), pp. 219–234.

[51] Krolo, A. *Planung von Zuverlässigkeitstests mit weitreichender Berücksichtigung von Vorkenntnissen*. Dissertation. Stuttgart: Universität Stuttgart, 2004.

[52] Lagoudas, D. C. *Shape memory alloys. Modeling and engineering applications*. Boston, MA: Springer, 2008.

[53] Leckie, F. A. and Dal Bello, D. J. *Strength and stiffness of engineering systems*. Mechanical Engineering Series. New York, NY: Springer, 2009.

[54] Li, S. et al. *Approach to prove the efficiency of the monte carlo method combined with the elementary effect method to quantify uncertainty of a beam structure with piezo-elastic supports*. In: *Proceedings of UNCECOMP 2017*. Rhodes Island, Greece, 2017, pp. 441–455.

[55] Lindberg, H. E. and Florence, A. L. *Dynamic Pulse Buckling. Theory and Experiment*. Vol. 12. Mechanics of Elastic Stability. Dordrecht: Springer, 1987.

[56] Ljung, L. *System Identification Toolbox. User's Guide*. Natick, MA: MathWorks, 2017.

[57] Lubkin, S. and Stoker, J. J. *Stability of columns and strings under periodically varying forces*. In: *Quarterly of Applied Mathematics* 1.3 (1943), pp. 215–236.

[58] Lundström, P., Skogestad, S., and Wang, Z.-Q. *Performance weight selection for $\mathcal{H}_\infty$ and μ-control methods*. In: *Transactions of the Institute of Measurement and Control* 13.5 (2016), pp. 241–252.

[59] Lunze, J. *Regelungstechnik 1. Systemtheoretische Grundlagen, Analyse und Entwurf einschleifiger Regelungen*. Berlin: Springer, 2008.

[60] Mallapur, S. and Platz, R. *Uncertainty quantification in the mathematical modelling of a suspension strut using Bayesian inference*. In: *Mechanical Systems and Signal Processing* 118 (2019), pp. 158–170.

[61] Markert, R. *Strukturdynamik*. Mechanik. Aachen: Shaker, 2013.

[62] Mathworks Inc., ed. *Optimization Toolbox. User's Guide*. Natick, MA: MathWorks, 2018.

[63] Mathworks Inc., ed. *Statistics and Machine Learning Toolbox. User's Guide*. Natick, MA: MathWorks, 2018.

[64] Meressi, T. and Paden, B. *Buckling Control of a Flexible Beam Using Piezoelectric Actuators*. In: *Journal of Guidance, Control, and Dynamics* 16.5 (1993), pp. 977–980.

[65] Meyer, M. *Signalverarbeitung. Analoge und digitale Signale, Systeme und Filter*. Wiesbaden: Vieweg, 2006.

[66] Moheimani, S. O. R. and Fleming, A. J. *Piezoelectric Transducers for Vibration Control and Damping*. Advances in Industrial Control. London: Springer, 2006.

[67] Mukherjee, A. and Chaudhuri, A. S. *Active control of dynamic instability of piezolaminated imperfect columns*. In: *Smart Materials and Structures* 11.6 (2002), pp. 874–879.

[68] Mukherjee, A. and Chaudhuri, A. S. *Active control of piezolaminated columnsexact solutions and experimental validation*. In: *Smart Materials and Structures* 14.4 (2005), pp. 475–482.

[69] Ondoua, S. *Unsicherheit in der Bewertung von Struktur- Eigenschaftsbeziehungen zwischen aktiven und passiven Systemelementen in aktiven lasttragenden Systemen*. Dissertation. Darmstadt: Technische Universität Darmstadt, 2016.

[70] Packard, A. *Gain scheduling via linear fractional transformations*. In: *Systems & Control Letters* 22.2 (1994), pp. 79–92.

[71] PI Ceramic GmbH. *Piezoelectric Actuators. Components , Technologies , Operation*. Ed. by PI Ceramic GmbH. Lederhose, 2016.

[72] Preumont, A. *Vibration control of active structures. An introduction*. Berlin: Springer, 2011.

[73] Przemieniecki, J. S. *Theory of Matrix Structural Analysis*. New York, NY: McGraw-Hill, 1968.

[74] Schaeffner, M., Enss, G. C., and Platz, R. *Influence of uncertain support boundary conditions on the buckling load of an axially loaded beam-column*. In: *Proceedings of ISMA2014 including USD2014*. Leuven, Belgium, 2014, pp. 4675–4686.

[75] Schaeffner, M., Enss, G. C., and Platz, R. *Mathematical modeling and numerical simulation of an actively stabilized beam-column with circular cross-section*. In: *Proceedings of SPIE Vol. 9057 Active and Passive Smart Structures and Integrated Systems*. San Diego, CA, 2014, 90572H.

[76] Schaeffner, M., Götz, B., and Platz, R. *Active buckling control of a beam-column with circular cross-section using piezo-elastic supports and integral LQR control*. In: *Smart Materials and Structures* 25.6 (2016), pp. 1–10.

[77] Schaeffner, M. and Platz, R. *Active buckling control of an imperfect beam-column with circular cross-section using piezo-elastic supports and integral LQR control*. In: *Journal of Physics: Conference Series* 744.1 (2016), pp. 1–12.

[78] Schaeffner, M. and Platz, R. *Linear Parameter-Varying (LPV) Buckling Control of an Imperfect Beam-Column Subject to Time-Varying Axial Loads*. In: *Proceedings of the 35th IMAC*. Conference proceedings of the Society for Experimental Mechanics. Los Angeles, Anaheim: Springer, 2017, pp. 103–112.

[79] Schaeffner, M. and Platz, R. *Gain-scheduled $\mathscr{H}_\infty$ buckling control of a circular beam-column subject to time-varying axial loads*. In: *Smart Materials and Structures* 27.6 (2018), p. 065009.

[80] Schaeffner, M., Platz, R., and Melz, T. *Active buckling control of an axially loaded beam-column with circular cross-section by active supports with integrated piezoelectric actuators*. In: *Proceedings of SMART2015*. Ponta Delgada, Azores, 2015.

[81] Sehr, M. A. *Synthesis of Robust Control for Mixed Uncertainties via μ-K Iteration*. Master Thesis. Darmstadt: Technische Universität Darmstadt, 2012.

[82] Sehr, M. A. et al. *A catalog of LMI conditions for gain-scheduled output-feedback $\mathscr{H}_\infty$-control*. In: *Proceedings of CACSD 2016*. Buenos Aires, Argentina: IEEE, 2016, pp. 1060–1065.

[83] Shamma, J. S. and Athans, M. *Gain Scheduling: Potential Hazards and Possible Remedies*. In: *Proceedings of American Control Conference, 1991*. Boston, MA: IEEE, 1991, pp. 516–521.

[84] Simitses, G. J. *Dynamic Stability of Suddenly Loaded Structures*. New York, NY: Springer, 1990.

[85] Skogestad, S. and Postlethwaite, I. *Multivariable feedback control*. Chichester: John Wiley & Sons, 2001.

[86] Stephenson, A. *On a new type of dynamic stability*. In: *Memories and Proceeding of the Manchester Literary and Philosophical Society* 52 (1908), pp. 1–10.

[87] Sweet, A. L., Genin, J., and Mlakar, P. F. *Determination of Column-buckling Criteria Using Vibratory Data*. In: *Experimental Mechanics* (1977).

[88] Thompson, S. P. and Loughlan, J. *The active buckling control of some composite column strips using piezoceramic actuators*. In: *Composite Structures* 32 (1995), pp. 59–67.

[89] Timoshenko, S. P. and Gere, J. M. *Theory of elastic stability*. New York: McGraw-Hill, 1961.

[90] VDI Verein Deutscher Ingenieure, ed. *Aktive Schwingungsisolierung*. VDI. Berlin: Beuth Verlag, 2010.

[91] Virgin, L. N. *Vibration of axially loaded structures*. New York: Cambridge University Press, 2007.

[92] Wang, Q. S. *Active buckling control of beams using piezoelectric actuators and strain gauge sensors*. In: *Smart Materials and Structures* 19.6 (2010), pp. 1–8.

[93] Waszczyszyn, Z., Cicho, C., and Radwaska, M. *Stability of structures by finite element methods*. Vol. 40. Studies in applied mechanics. Amsterdam and New York: Elsevier, 1994.

[94] Weibull, W. *A Statistical Distribution Function of Wide Applicability*. In: *Journal of Applied Mechanics* 18 (1951), pp. 293–297.

[95] Wiedemann, J. *Leichtbau. Elemente und Konstruktion*. Berlin: Springer, 2007.

[96] Zenz, G. and Humer, A. *Stability enhancement of beam-type structures by piezoelectric transducers. Theoretical, numerical and experimental investigations*. In: *Acta Mechanica* 226.12 (2015), pp. 3961–3976.

[97] Zhou, K. and Doyle, J. C. *Essentials of robust control*. Upper Saddle River, NJ: Prentice Hall, 1998.

[98] Zhou, K., Glover, K., and Doyle, J. C. *Robust and optimal control*. Upper Saddle River, NJ: Prentice Hall, 1995.

[99] Zienkiewicz, O. C. and Taylor, R. L. *The Finite Element Method. Volume 2: Solid mechanics*. Oxford: Butterworth-Heinemann, 2000.

[100] Zimmermann, B. *Bewertung und Anpassung eines piezo-elastischen Balkenlagers zur Strukturkontrolle von Balken mit Kreisquerschnitt*. Master Thesis. Darmstadt: Technische Universität Darmstadt, 2016.

List of Figures

1.1 Practical beam-column for active buckling control and modular active spring-damper system . . . 3

2.1 Beam-column subject to axial load $F_x(t)$ with rotational support stiffness k_φ for buckling analysis . . . 7
2.2 Normalized critical buckling load $F_{x,\mathrm{cr}}/F_{x,\mathrm{E\text{-}II}}$ versus normalized rotational support stiffness $k_\varphi/(EI/l)$ . . . 10
2.3 Beam-column center deflection v_{cn} versus axial load F_x for ideal and real beam-columns with increasing disturbance M_{d} . . . 12
2.4 Normalized first resonance frequency $f_1/f_{1,\mathrm{E\text{-}II}}$ versus normalized rotational support stiffness $k_\varphi/(EI/l)$ and normalized axial load $F_x/F_{x,\mathrm{E\text{-}II}}$ . . . 13
2.5 Probability distributions of random variable X for normal and WEIBULL distribution . . . 21

3.1 Schematic sketch of the axially loaded beam-column with elastic supports, piezoelectric stack actuators and strain gauge sensors . . . 28
3.2 Concept of the beam-column system for active buckling control . . . 30
3.3 Sketch of the FE beam-column . . . 32
3.4 n-th finite beam-column element of length l_{el} . . . 34
3.5 Assembly scheme for the $[4N \times 4N]$ FE mass and stiffness matrices . 40
3.6 First three normalized eigenvectors $\widehat{\boldsymbol{r}}_{1/2/3}(F_x)$ . . . 42
3.7 Block diagram of the beam-column plant $\boldsymbol{P}(F_x)$ . . . 49
3.8 Block diagram for controller synthesis . . . 54
3.9 Block diagram of the open-loop plant $\boldsymbol{P}_{\mathrm{ol}}(F_x, s)$ . . . 56
3.10 Block diagram of augmented open- and closed-loop plants . . . 57
3.11 Amplitude and phase responses of the input and output weight transfer functions plotted versus excitation frequency $\Omega/2\pi$ . . . 59

4.1 Experimental test setup and beam-column with piezo-elastic supports for active buckling control . . . 64
4.2 Beam-column with piezo-elastic supports for experiments . . . 65
4.3 Sectional views of piezo-elastic support A . . . 67

4.4 Membrane spring elements in support A 68
4.5 Experimental variation in the measured stiffness parameters in y- and z-direction of ten membrane spring elements 69
4.6 Signal processing in the beam-column system for active buckling control 72

5.1 Experimental beam-column plant transfer functions of the beam-column system [b2-AB1-p1] for different static axial loads F_x 75
5.2 Experimental lateral dynamic behavior of the beam-column system [b2-AB1-p1] for different static axial loads F_x 76
5.3 Envelopes of 30 experimental beam-column plant transfer functions for different static axial loads F_x 78
5.4 Experimental lateral dynamic behavior of 30 beam-column systems for different static axial loads F_x 79
5.5 Experimental and numerical beam-column plant transfer functions of the beam-column system [b2-AB1-p1] for different axial loads F_x . . 83
5.6 Experimental and numerical beam-column dynamic behavior of the beam-column system [b2-AB1-p1] for different static axial loads F_x . 84
5.7 Normalized histograms of the $2 \cdot 30$ calibrated parameter sets and normal distribution fits $p_{\mathrm{N}}(X)$ 87
5.8 Envelopes of 30 experimental beam-column plant transfer functions and numerical mean beam-column plant 88
5.9 Experimental lateral dynamic behavior of 30 beam-column systems for different static axial loads F_x and mean beam-column plant 89
5.10 Amplitude responses of open- and closed-loop plant $|\boldsymbol{P}_{\boldsymbol{w}\rightarrow\boldsymbol{z}}(F_x, \Omega)|$ and upper bounds $\Gamma_{\boldsymbol{w}\rightarrow\boldsymbol{z}}(\Omega)$ for different axial loads F_x 92
5.11 Static amplitude response $|\boldsymbol{P}_{d\rightarrow y_{\mathrm{t}}}(\Omega = 0)|$ versus axial load F_x for open- and closed-loop plant 93

6.1 Experimental quasi-static axial load F_x versus time t 97
6.2 Experimental step-shaped axial load F_x versus time t 98
6.3 Passive and active beam-column system [b2-AB1-p1] with quasi-static axial load F_x: modal displacements and control inputs 100
6.4 Passive and active beam-column system [b2-AB1-p1] with quasi-static axial load F_x: absolute modal displacement 101
6.5 All 30 passive and active beam-column systems with quasi-static axial load $F_x(t)$ 103
6.6 Passive and active maximum bearable axial loads $F_{x,\max}$ with most likely value $\Sigma_{F_{x,\max}}$ and interpercentile range $R_{F_{x,\max}}$ 104

6.7 Passive and active beam-column system [b2-AB1-p1] with dynamic axial load $F_x(t)$: modal displacements and control inputs 106
6.8 Passive and active beam-column system [b2-AB1-p1] with dynamic axial load $F_x(t)$: absolute modal displacements 107
6.9 All 30 passive and active beam-column systems with dynamic axial load $F_x(t)$ 109
6.10 Scatter plot of passive and active absolute modal displacements q_1 . . 110
6.11 Normalized histograms, fitted pdf $p_W(q_1)$, empirical and fitted cdf $P_W(q_1)$ of passive and active absolute modal displacements q_1 111

A.1 Probability plots for assumed normal distributions of the experimental first resonance frequencies $f_{1,y/z,\mathrm{exp}}(F_x)$ 119
A.2 Probability plots for assumed normal distributions of the $2 \cdot 30$ calibrated parameter sets $\boldsymbol{p}_y$ and $\boldsymbol{p}_z$ 120
A.3 Probability plots for assumed three-parameter WEIBULL distributions of the experimental maximum bearable axial loads $F_{x,\mathrm{max,p/a}}$ 121
A.4 Probability plots for assumed normal distributions of the experimental first resonance frequencies $f_{1,y/z,\mathrm{exp}}(F_x)$ 122
A.5 Amplitude and phase responses of the input and output weight transfer functions plotted versus excitation frequency $\Omega/2\pi$ 123

List of Tables

2.1 Numerical studies on active buckling control 16
2.2 Experimental studies on active buckling control 18

4.1 Mechanical components of the experimental test setup 66
4.2 Mean μ_X and standard deviation σ_X of the stiffness parameters for the ten different piezo-elastic supports 70
4.3 Beam-column system components for exp. uncertainty quantification 70
4.4 Electrical components of the experimental test setup 71

5.1 Normal distribution fits of the experimental first resonance frequencies $f_{1,y/z,\mathrm{exp}}(F_x)$ of the 30 investigated beam-column systems 79
5.2 Fixed parameters of the beam-column plant 81
5.3 Calibrated parameter values of $\boldsymbol{p}_{y/z}$ for the beam-column system [b2-AB1-p1] in y- and z-direction 83
5.4 NRMSE values $\Delta_{y/z}(F_x)$ of experimental and numerical transfer functions after calibration for beam-column system [b2-AB1-p1] 85
5.5 Normal distribution fits for the $2 \cdot 30$ calibrated parameter sets $\boldsymbol{p}_y$ and $\boldsymbol{p}_z$ 86
5.6 Parameters of frequency-dependent input and output weights 90

6.1 Experimental cases for passive buckling and active buckling control . 99
6.2 Parameters of three-parameter WEIBULL distribution fits for maximum bearable axial loads $X = F_{x,\mathrm{max,p/a}}$ 105
6.3 Beam-column absolute modal displacements $q_{1,\mathrm{start}}$, $q_{1,\mathrm{peak}}$ and $q_{1,\mathrm{end}}$ for dynamic axial load $F_x(t)$ 108
6.4 Parameters of the three-parameter WEIBULL distribution fits for the absolute modal displacements $X = q_{1,\mathrm{start}}$, $q_{1,\mathrm{peak}}$ and $q_{1,\mathrm{end}}$ 112